NTNU
Norwegian University of
Science and Technology

Modelling, Simulation, and On-line Detection of Rotor Eccentricity in Hydropower Generators

Andreas Blix Møller

Master of Energy and Environmental Engineering
Submission date: June 2018
Supervisor: Arne Nysveen, IEL
Co-supervisor: Mostafa Valavi, IEL

Norwegian University of Science and Technology
Department of Electric Power Engineering

NORGES TEKNISK-NATURVITENSKAPELIGE UNIVERSITET

NTNU

M A S T E R O P P G A V E

Kandidatens navn	:	Andreas Blix Møller
Fag	:	**ELKRAFTTEKNIKK**
Oppgavens tittel (norsk)	:	Modellering, simulering og on-line deteksjon av rotor eksentrisitet i vannkraft generatorer
Oppgavens tittel (engelsk)	:	Modelling, simulation and on-line detection of rotor eccentricity in hydro generators

Oppgavens tekst:

The synchronous generator is a critical component in the hydropower plants and condition monitoring to detect faults (such as short circuit between turns in rotor or stator windings, eccentricity) and avoid failures are valuable. Based on earlier research on rotor inter-turn fault detection, the objective in this work is to investigate the suitability of the method for detecting eccentricity. The method is based on a frequency analysis of the terminal voltages and currents.

The project study includes:

- Familiarize with fault induced harmonics in stator terminal voltage and current .
- Model selected machines in suitable FEM-software for analysing the harmonic spectrum due to eccentric faults in selected generators.
- Study the methods capability to detect eccentricity faults.
- Investigate the possibility to discriminate between different eccentricity faults and also between eccentricity faults and rotor inter-turn faults.

Further details to be clarified with the supervisors.

Oppgaven gitt : 15. januar 2018

Oppgaven revidert:	: 5. juni 2018
Besvarelsen leveres innen	: 11. juni 2018
Besvarelsen levert	:
Utført ved (institusjon, bedrift)	: Institutt for elkraftteknikk/NTNU
Kandidatens veileder	: Mostafa Valavi/NTNU
Faglærer	: Professor Arne Nysveen

Trondheim, 5. juni 2018

Arne Nysveen

faglærer

Abstract

The generator is a critical component in the hydropower power plant, and detection of its fault conditions is important for safe and cost-effective operation. A new proposed method for detection of rotor interturn short circuits (ITSC), based on detecting harmonic sidebands produced around the main harmonic (the 50[Hz]) and its third harmonic (the 150[Hz]) when there is a fault on the generator, might be used for detection of eccentricity fault conditions on hydro generators [29].

This master thesis investigated the ability of the rotor interturn short circuit detection method to detect eccentricity and differentiate between eccentricity and rotor interturn short circuit faults. The thesis also investigated the method's capability to detect rotor ITSC with static eccentricity. The method was investigated through simulations using the finite element simulation software Ansys Maxwell. The simulations has been made on a model based on technical drawings of a real generator, and three models with slight modifications in generator topology. The results of the simulation showed that the method is highly dependent on generator topology, and is unsuited for some generator topologies. For the cases it is suitable it can detect rotor ITSC with static eccentricity even at low levels of fault severity. Dynamic eccentricity can be detected as it entered critical levels. Mixed eccentricity can be detected, but some critical levels of the fault can go unnoticed by the method. The method is unsuited for detection of static eccentricity. There has also been found a way to differentiate between eccentricity and rotor interturn faults based on the amplitude of two of the harmonic sidebands.

Sammendrag

Generatoren er en kritisk komponent i et vannkraftverk, og oppdagelse av dens feiltilstander er viktig for sikker og kosteffektiv drift av vannkraftverket. En ny metode for deteksjon av kortslutning på isolasjonen mellom viklingene på rotor, basert på gjenkjenning av harmoniske sidebånd produsert av feilen, kan også muligens bli brukt til å oppdage feil relatert til eksentrisitet på vannkraftgeneratorer [29].

Denne masteroppgaven undersøker metoden for deteksjon av kortslutning på isolasjon mellom viklingene på rotor sin evne til å detektere eksentrisitetfeil, samt skille mellom eksentrisitetfeil og kortslutningsfeil. Masteroppgaven undersøker også metodens evne til å oppdage rotor kortslutningsfeilen når generatoren også er utsatt for statisk eksentrisitet. Metoden ble undersøkt gjennom endelig element metode simuleringer. Simuleringene ble gjort med simuleringsprogrammet Ansys Maxwell. Simuleringene ble gjort på en modell basert på tekniske tegninger av en ekte vannkraftgenerator, og tre modeller med noen små endringer i generator topologien. Resultatet viste at metoden er sterkt avhengig av generatorens topologi, og er i noen tilfeller uegnet som deteksjonsmetode. Når den er egnet kan den oppdage rotorkortslutningfeil med statisk eksentrisitet selv for lave feil-nivåer. Dynamisk eksentrisitet kan bli oppdaget når graden av dynamisk eksentrisitet blir kritisk. Blandet eksentrisitet kan også bli oppdaget, men noen kritiske grader av blandet eksentrisitet kan gå uoppdaget av metoden. Metoden er uegnet for deteksjon av statisk eksentrisitet. En metode ble foreslått, basert på amplituden til to av de harmoniske sidebåndene, for å skille dynamisk og blandet eksentrisitet fra feil med rotor kortslutning.

Pre-face and Acknowledgements

This master thesis is conducted as part of the 5-year Master of Science (MSc) study program: “Energi og miljø”, at the Norwegian University of Science and Technology (NTNU). The thesis was written during the spring semester of 2018, at the Department of Electrical Power engineering and has a weighting of 30 credits.

The thesis investigates the electrical frequency response of a hydro generator operating with rotor eccentricity. The investigation was done through finite element modelling simulations of healthy and faulty generators. The thesis assumes the reader has a basic understanding of power engineering, generator design and finite element modelling.

I would like to thank Erik Albjerk Kaggestad and Geir Aalvik, from Statkraft Energi AS, for their contributions to the thesis through their sharing of experience and their practical knowledge of hydro generators. I would also like to thank my supervisor Professor Arne Nysvenn and my co-supervisor Mostafa Valavi for their help and guidance throughout the thesis.

Trondheim, June 2018

Andreas Blix Møller

Table of Content

List of Figures

List of Tables

Abbreviations

NTNU	Norwegian University of Science and technology
ITSC	Interturn short circuit
FEM	Finite element model
TSFE	Time-stepping finite element
TSFEM	Time-stepping finite element model
UMP	Unbalanced magnetic pull
MMF	Magnetomotive force
PMSM	Permanent magnet synchronous motor
UDP	User defined primitives
FFT	Fast Fourier transformation
PSD	Power spectra density

Symbols

O_s	Centre of stator
O_R	Centre of rotor
O_ω	Centre of rotation
N_s	Number of slots [#]
N_P	Number of poles [#]
P	Number pole pair [#]
e	Induced voltage [V]
ϕ	Magnetic flux [Wb]
MMF	Magnetomotive force [At]
Λ	Impedance [Ω]
R_s	Inner radius of the stator [mm]
R_R	Outer radius of the rotor [mm]
g_0	Nominal air-gap [mm]
δ_s	Degree of static eccentricity
δ_d	Degree of dynamic eccentricity
θ_s	Stator reference angle [Degree]
ω_R	Mechanical rotational speed [$\frac{rad}{s}$]
ω_S	Electrical rotational speed [$\frac{rad}{s}$]
μ_0	Permittivity of free space [$\frac{F}{m}$]
f_s	Synchronous frequency [Hz]
θ_P	Pole span [Degree]
q	Number of slots per pole per phase
n_S	Mechanical rotational speed [rpm]
B_s	Magnetic flux density in the air-gap [T]
j_S	Current density in the inner surface of the stator [A]

1 Introduction

Hydro generators contribute to 95.8% of the Norwegian power production in 2017 [2], and are an important component in the Norwegian power system. The hydroelectric generator is a large and expensive piece of machinery and its failures can have a high associated cost, both in terms of actual repair cost and in terms of outage cost. Therefore, hydroelectric generators are subjected to preventive maintenance, to ensure safe and cost-effective operation. Preventive maintenance strategies seek to avoid failure by utilizing monitoring and inspections, and pre-emptive repair and replacement of degraded components [3,4]. For these strategies to be cost-effective and reliable there is a requirement for reliable and cost-effective monitoring and inspection methods. The advancement of technology, giving more cost-effective equipment capable of doing more calculation than before, gives the opportunity of improving the maintenance by utilizing more continuous on-line monitoring methods [5].

In this paper a non-invasive, on-line method for monitoring of the eccentricity conditions in hydropower generators was investigated. The method has previously been shown to be able to monitor rotor ITSC faults [1]. There was therefore an interest to see if the method could differentiate between a generator experiencing eccentricity and a generator with a rotor ITSC. The method monitors the stator phase voltage and the stator phase current for fault signatures. The fault signatures presents themselves as harmonic sideband in the terminal output signals. The faults were investigated through simulations using the Ansys Maxwell, a software capable of doing electromagnetic time-stepping finite element (TSFE)-

simulations. The simulations were done on a finite element model based (FEM) of a real hydro generator, and on a few models based on the same generator with some modifications.

1.1 Background

Norwegian University of Science and Technology (NTNU) and Statkraft Energi AS are both interested in studying the possibility of developing new and improved condition monitoring technics for hydro power generators. Hench, they cooperatively entered a joint project to look into condition monitoring of hydro generators. In the summer of 2017, Statkraft reviewed the fault statistics of their generators. The review showed that one of the more problematic components were the generator- and turbine-bearings. There is a known connection between bearing wear and eccentricity [6]. A method found in an earlier master thesis [1], that was found to be suitable for monitor of rotor ITSC faults, were also theorised to be able to detect eccentricity faults too. It was therefore decided to investigate the method presented in [1] ability to detect eccentricity and differentiate between eccentricity and rotor ITSC faults. The Department of Electrical Power Engineering at NTNU were going to do the main research, while Statkraft contributed with technical experience.

1.2 Objective

The objective of this thesis was to investigate if the non-invasive, on-line detection method proposed in [1] for condition monitoring of rotor interturn short circuits is suitable for condition monitoring of eccentricity fault conditions. The method's ability to both detect, monitor severity and differentiate between fault conditions were under investigation. The aim was to get an improved understanding of the method's capabilities.

1.3 Scope of Work

The work included the following parts:

- A short review of eccentricity faults and the rotor interturn short circuit fault.
- A presentation of the proposed method and theoretical analysis of the fault signatures which that the proposed method should be able to detect.
- Time-stepping finite element (TSFE) -modelling and -simulations of a hydro generator operating under healthy, static eccentricity, dynamic eccentricity and mixed eccentricity conditions, and under rotor interturn short circuit fault with and without static eccentricity.
- Evaluation of the simulation results with focus on the proposed method's ability to detect eccentricity fault conditions and its ability to differentiate between the mentioned fault cases.

1.4 Thesis Limitations and Simulations Tool

The lack of available experimental setup limits the thesis to investigating the fault signatures through simulations. The simulation was performed with Maxwell Ansys v.2017.2.0. which is capable of preforming electromagnetic TSFE-simulations.

The simulations were limited by the thesis's time constraint. Because of the time constraint, a 2D model was used instead of a 3D model, limiting the thesis to assuming the faults have a symmetrical effect in the axial direction, which is not necessarily the case in dynamic and mixed eccentricity which are introduced in chapter 2.1. To reduce the computation time further, the core losses and eddy current losses for all parts, except the damper bars, were not included. This simplification is based on the assumption that the core losses and eddy current effects will have minimal impact on the fault induced harmonic spectrum. The generator and winding geometry was simplified, components with little effect on the magnetic field, like insulation and slot wedge, was modelled as air. The effect of the cooling channels in the stator core was not included. The simulations are done for no-load and full-load operation, the load in the full-load operation was modelled by a pure-resistive external circuit.

Simulations on the static eccentricity condition created by ovality in the stator bore, which is introduced in chapter 2.2, was not performed because of some technical issues with the modelling of this condition. The thesis was also limited to only looking at rotor ITSC faults with only one faulty pole.

1.5 Structure of the Thesis

Chapter 2: Presents a short overview of main types of faults in a hydrogenator, then gives a description of the eccentricity fault conditions, their causes and effects. The chapter ends with a description of the rotor interturn short circuit fault, its cause and effect.

Chapter 3: Presents the proposed method for condition monitoring of rotor interturn short circuit faults and eccentricity faults. The chapter ends with a theoretical calculation of the harmonics that the proposed method should be able to detect.

Chapter 4: Gives a description how the time-stepping finite element model (TSFEM) was created and how the fault conditions was modelled. The chapter also contains verifications of healthy and faulty models.

Chapter 5: Contains the results from the fault simulations

Chapter 6: Discuss the results of presented in chapter 5. With a focus on the proposed method's ability to detect eccentricity and differentiate between eccentricity and rotor ITSC.

Chapter 7: Contains a summary of the most important discoveries within the paper.

2 Fault Overview

2.1 Overview of the Hydrogenator Faults

Hydroelectric generators are large, rotating electrical machines, and as such they may be subjected to an array of faults. The faults can be caused by an internal fault condition or an external event stressing the machine [7]. The faults can be placed into four categories: electrical faults, mechanical faults, contamination faults and thermal faults. The rest of this subchapter give a short overview of these four categories, and are based on the theory of [7] and [8].

Electrical faults exert an electrical stress on the generator, the stress can come from events in the external grid, operating in unsuitable conditions or from an internal fault within the generator. Electrical stressing can cause short circuits in the rotor and stator windings, overvoltages, cause overheating and create unbalance between currents in the stator or rotor windings which can induce strong unwanted forces in the generator.

Mechanical faults are faults of a mechanical nature which induces vibration or exerts a force onto the generator as a whole or onto specific parts. It may be caused by faulty generator design or faulty assembly, operating under unsuited operating conditions or by mechanical degradation of certain components. Mechanical faults can cause bearing wear, slacking of bush gear, commutator and windings, mechanical degradation of the insulating materials, fatigue and fretting damage.

The contamination faults are related to accumulation of dust, foreign particles, debris from the brushes, oil spill from leakage in the oil circuit

and water spills from the cooling system. The accumulation of contamination may lay a protective layer over certain parts of the generator reducing its thermal efficiency, which may lead to thermal degradation. The accumulation may create conductive paths and lead to flashover between components. The contamination may also get into and cause problems in the bearings. Certain chemicals can also cause chemical degradation of the insulation.

Thermal faults are related to excessive heat accumulation within the generator, as a whole or in hotspots. The excessive heat may lead to thermal degradation of the insulation material. The thermal problems may arise with a reduction in the cooling systems efficiency, operating at or above rated limit for a prolonged duration and/or ambient temperature above normal values.

The rest of this thesis focuses on the mechanical fault condition of eccentricity and the electrical fault condition of rotor ITSC. The next subchapters will give a description of eccentricity fault conditions, their causes and effects, and later go into the description of the rotor ITSC fault condition, its cause and effect.

2.2 Eccentricity Fault Conditions

Hydroelectric generators are large machines subjected to both radial and axial forces [9]. To be able to ensure safe and stable operation of the generator, the generator have to operate with an approximately uniform air-gap. To achieve this the shaft of the rotor needs to be kept centred within the centre of the stator, and kept there, while at the same time having the ability to rotate without much resistance. To be able to do this the generator uses radial and axial bearings to connect the rotating shaft to the stationary parts of the generator. The generator uses several bearings placed along the rotor shaft in the axial direction to keep it steady [8]. If the generator has a non-uniform air-gap between the stator and the rotor then the generator has a condition which is called eccentricity. There are two types of eccentricity: static eccentricity and dynamic eccentricity [7].

Static eccentricity is the condition when the shortest length in a non-uniform air-gap distribution has a constant length and is fixed in space [10]. This means that the non-uniform air-gap is static seen from the stator reference. Static eccentricity can be caused by a stator which is not perfectly circular [11], illustrated in figure 2.1. A non-circular stator bore, the distribution of the inner radius of the stator core, leads to some parts of the stator being closer to the rotor than others. The non-circularity of the generator can be caused by imperfections in the generator design or assembly, or by the stator core being blocked from thermally expanding equally in all parts of the stator core. The asymmetric thermal expansion causes greater movement in certain sections of the stator core than others, leading to an asymmetrical stator bore when the generator is heated [12].

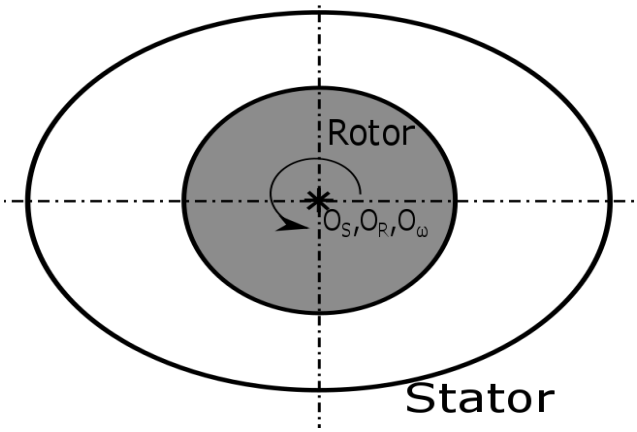

Figure 2.1: Illustration of static eccentricity caused by stator bore non-circularity. The stator centre is given by O_S, rotor centre by O_R and rotation centre by O_ω.

Static eccentricity can also be caused by incorrect positioning of the rotor shaft within the stator core [11]. If the rotor shaft is not positioned within the centre of the stator symmetry line when the generator is commissioned, there will be a fixed static displacement between the centre of the rotor and the centre of the stator. The rotor is then constantly be closer to one side of the stator, as illustrated in figure 2.2.

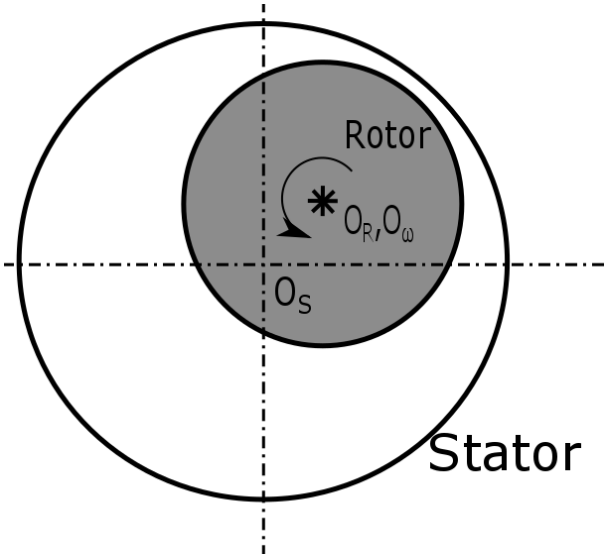

Figure 2.2: Static eccentricity caused by rotor displacement.
The stator centre is given by O_S, rotor centre by O_R and rotation centre by O_ω.

The effect of the static non-uniform air-gap is that there is no longer a balance between the magnetic forces acting on the generator and a static unbalanced magnetic pull (UMP) will act on the generator [9]. The static UMP can lead to a bent rotor shaft, increased wear on the bearings, vibrations leading to mechanical wear on stator frame and insulations, and if the rotor-shaft assembly is insufficiently stiff, the degree of static eccentricity will increase [10]. In reality all generators have some inherent static eccentricity, even at assembly [10]. Small degrees of eccentricity are normally unproblematic and does not reduce the life-time of the generator significantly. The tolerances for rotor and stator displacements and rotor and stator roundness are given in Table 2.1 [13], the given values are conservative.

Table 2.1: Table of conservative mechanical tolerance values for hydroelectric generator, given as deviation from the nominal air-gap [13].

	Deviation in the nominal air-gap		
Parameters	Assembly	Acceptable	Critical
Stator Roundness	< 7%	7 - 20%	> 20%
Stator Concentricity	< 5%	5 - 10%	> 10%
Rotor Roundness	< 6%	6 – 10%	> 10%
Rotor Concentricity	< 1.2%	1.2 - 4%	> 4%
Minimum Air-gap	> 85%	85 - 50%	< 50%

As mentioned the second type of eccentricity is dynamic eccentricity. Dynamic eccentricity is the condition where the centre of rotation does not coincide with the symmetry line of the rotor [10]. This means the centre of the rotor is not fixed in space, seen from the stator side, but will rotate around the rotation centre, as illustrated in figure 2.3. The smallest air-gap distance will rotate with the rotor and the air-gap distribution is both time and space dependent. Dynamic eccentricity can be caused by a bent rotor shaft, bearing wear, mechanical resonance at critical speeds, a tilted rotor caused by misalignment of the bearings and UMP [10, 6].

Dynamic eccentricity will induce a dynamic UMP, the UMP will follow the rotation of the rotor. The dynamic UMP will cause the same issues as

the static eccentricity UMP, but the added cyclic nature of the dynamic UMP will cause a higher degree of wear on the bearings [14].

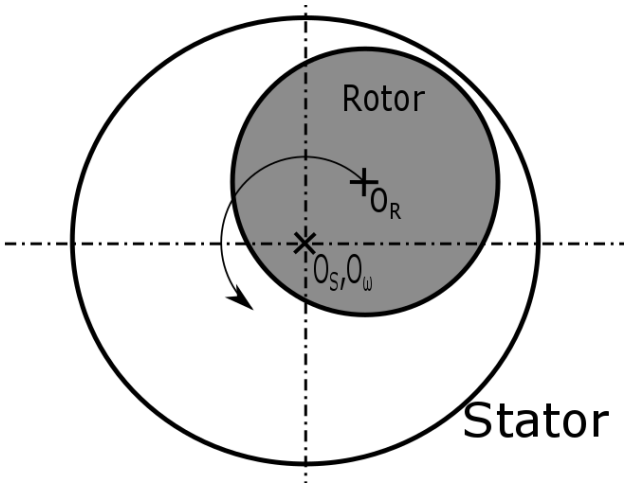

Figure 2.3: Illustration of dynamic eccentricity.
The stator centre is given by O_S, rotor centre by O_R and rotation centre by O_ω.

The two types of eccentricities may appear together and are then normally referred to as mixed eccentricity [10]. In the case of mixed eccentricity, the rotor centre will be displaced from both the stator centre and the centre of rotation, the rotational axis is also displaced from the stator centre. This will create a condition where the rotor rotates around the rotational centre which is displaced with a fixed distance from the stator centre, as illustrated in figure 2.4.b. The shortest air-gap length now varies in length and rotates with the rotor. Mixed eccentricity will happen in the case of a progressive static eccentricity fault condition, because increasing UMP will eventually lead to dynamic eccentricity [6]. Mixed eccentricity will also happen in most cases where we have a dynamic eccentricity, because of the inherent

static eccentricity in the machine. Mixed eccentricity can also appear with a non-circular stator bore and dynamic eccentricity as shown in figure 2.4.a.

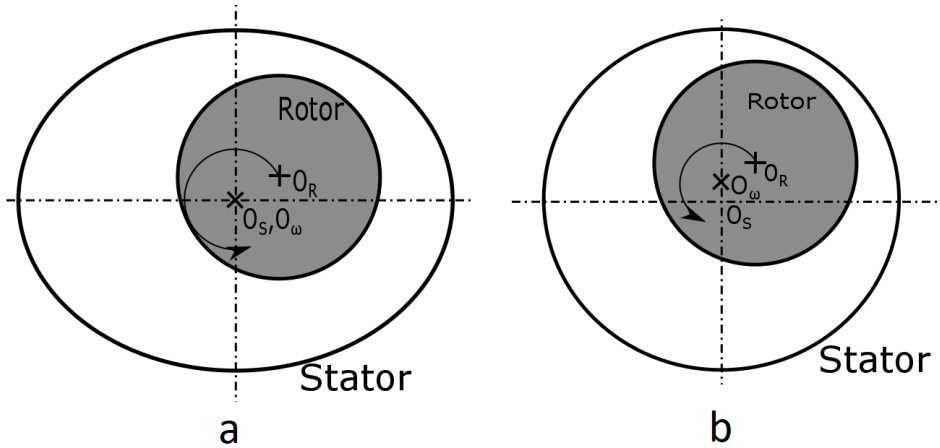

Figure 2.4: Illustration of Mixed eccentricity.

Illustration a) shows mixed eccentricity where the static component is caused by stator non-non-circularity, while in b) the static component is caused by rotor shaft displacement. The stator centre is given by O_S, rotor centre by O_R and rotation centre by O_ω.

This thesis will treat static, dynamic and mixed eccentricity separately, where dynamic eccentricity has a rotational centre coincided with the stator centre. The thesis will also only look at cases where the eccentricity is symmetrical in the axial-direction of the generator, and where the static eccentricity component in the static and mixed eccentricity conditions are produced by an improper positioning of the rotor shaft.

2.3 Rotor Interturn Short Circuit

Hydro generators are generally salient pole synchronous machines, where the poles are mounted on the rotor rim. Each pole is made up of laminated steel in a shape similar to that of a rectangle, with a pole shoe on the end facing towards the stator and the other end attached to the rotor rim. Around the rectangle part of the pole the field winding is wound. The field windings consist of several conducting copper turns which are insulated from each other and the rest of the pole. The field winding is supplied by a DC-current, and connected in such a way that each pole is neighboured by poles of the opposite polarity [15].

Rotor ITSC is a short-circuit which happens when the internal insulation between one or more turns is degraded to a such a degree that its unable to withstand applied mechanical or electrical stress, leading to a breakdown of the insulation. The effect of the rotor ITSC is that current will take the shortest path, leaving the shorted turns without current and reducing the total magnetomotive force (MMF) produced by the faulty pole. Since the reduction of MMF only happens over the faulty pole it will create an unbalanced magnetic field which will induce UMP. The UMP of the rotor ITSC fault will rotate with the rotor, similarly to the UMP produced by dynamic eccentricity. The UMP will have similar effects on the generator as the UMP produced by the dynamic eccentricity [9], this type of dynamic UMP can also cause dynamic eccentricity. The rotor ITSC can also lead to local overheating [5]. The UMP produced by the rotor ITSC is dependent on the number of shorted turns and the numbers of faulty poles and their location in reference to each other [33]. This thesis will only look at the effect of one fault affected pole, with varying number of shorted turns. As mentioned in chapter 2.2 all generators have some inherent eccentricity

therefore this thesis will look into both rotor ITSCs with and without static eccentricity.

According to [15] the degradation of the interturn isolation may be caused by thermal degradation, thermal expansion of the copper windings, contamination, abrasive air and centrifugal forces. The rest of this subchapter will give a brief explain of these degradation phenomena and is based on information given in [15].

Thermal ageing causes the insulation material to become brittle, reducing its resistance to mechanical stress. Thermal aging happens when the insulation material is subjected to temperatures higher than what the material is designed for. The high temperatures can be caused by overloading of the generator, poorly designed cooling system, over excitation of the rotor windings, and zero-sequence currents in the rotor windings caused by system voltage unbalance. The thermal degradation can also happen at normal temperatures if the material properties of the chosen insulating material is below the required level.

The thermal expansion problem is based in the fact that the copper windings and the interturn insulation have different coefficients for thermal expansion, so when the machine goes for cold to hot or hot to cold, there will be a relative motion between the copper and the interturn insulation. This relative motion will lead to abrasion damage on the insulation. The generator goes from cold to hot and hot to cold when it starts and stops, respectively. The main cause of thermal expansion damage is therefore frequent starting and stopping of the generator, along with poor generator design.

Contamination of the winding happens when dust, oil and moisture accumulate on the winding. The contamination can create a conductive path between turns, which can lead to rotor ITSC through electrical tracking. The winding insulation can also experience chemical degradation if they come in contact with certain chemicals.

Abrasive air damage is caused by the cooling system dragging abrasive dust into the generator, which will abrade the winding insulation.

The rotor windings are subjected to continuous centrifugal forces caused by the rotation and cyclic centrifugal forces, caused by starting and stopping the generator. If the rotor winding insulation has been degraded by thermal expansion or thermal degradation, then these forces can cause the winding insulation to crack. If bracings of the windings, the component holding the windings apart and in position, is not strong enough to withstand the mechanical stress the conductors can be distorted and the winding insulation will be subjected to mechanical wear, and might crack.

3 Proposed Detection Method

The proposed method has been presented and investigated for a hydro generator with rotor interturn short circuits in [1]. The proposed method utilizes the fact that asymmetrical flux density distributions within the air-gap can give rise to new harmonic sidebands within the stator phase current and voltage [7]. The air-gap will be asymmetrical for all the fault conditions in this thesis. The eccentricity conditions make the air-gap flux asymmetric by making the air-gap length asymmetric. The rotor ITSC-fault changes the air-gap flux symmetry by reducing the MMF produced by one pole [16].

The results of [1] show that the rotor ITSC produced sideband harmonics on both sides of the regular harmonics found in a healthy generator. The sidebands were found in both the stator phase current and stator phase voltage. This thesis will investigate if similar sidebands appear in the stator phase voltage and stator phase current when the asymmetrical flux density distribution is created by static eccentricity, dynamic eccentricity, mixed eccentricity or by rotor ITSC with static eccentricity. This is very likely, given that the harmonic sidebands have been observed in experimental testing of a permanent magnet synchronous motor (PMSM) for static, dynamic and mixed eccentricity in [17]. The sideband harmonics has also been observed in induction motor in [25] and for mixed eccentricity in a synchronous turbo generator [18], and in the line-current for mixed eccentricity in a synchronous motor [32].

The weakness of the proposed method is the fact that the frequency spectrum of the stator voltage and stator current is dependent on generator topology, winding layout and winding connection. The topology

dependency of the sideband harmonics has been investigated for a PMSM with a defect magnet in [19], which has similar characteristics to a rotor ITSC. The effect of different winding configurations (double-layer, single-layer, fractional and full-pitch), number of poles, number slots was investigated. The results from [19] showed that the frequency spectrum changed with changing topology. For a double-layer winding it was found that machines with relationship between the number of slot and the number of poles:

$$\frac{N_s}{2P} = 1.5k, \tag{1}$$

where k is a positive integer had a total elimination of all the fault induced harmonic sidebands. The same happens for single-layer windings, when the relationship is:

$$\frac{N_s}{2P} = 3k. \tag{2}$$

It was also found that 0.75^{th} harmonic (the 75Hz) and its multiples were eliminated in machines with a wye-connection from the current frequency spectrum, this was also found in [1]. The reason for this, according to [19], is that the star-connect balanced three-phase system have a floating neutral point which eliminates certain harmonics. In [33] it was found that when more than one pole was defect, the frequency spectrum was dependent on the severity and location of the defect poles. The effect of several faulty poles will not be looked into in this thesis.

3.1 Theoretical Calculation of the Harmonic Fault Signatures.

The harmonic sidebands that the proposed method is using as fault indicators are induced from the non-uniform magnetic flux ϕ in the airgap. The relation between the induced voltage e and magnetic flux is [20]:

$$e = C\frac{d\phi}{dt}, \tag{3}$$

where C is a constant dependent the generator design. This means that the harmonics found in the magnetic flux should be present in the induced voltage. The fault conditions affect the magnetic flux in different ways. The rotor ITSC fault produces an unbalance in the produced MMF, while eccentricity disrupts the balance of the permeance of the machine through the effect of the non-uniform air-gap length distribution. The relation between the magnetic flux, permeance and MMF is given by Hopkin's law [5] as:

$$\phi = MMF \cdot \Lambda, \tag{4}$$

where MMF is the magnetomotive force and Λ is permeance.

The following subchapters will through calculation find which sidebands the proposed method might be able to detect. The calculations use the simplification of a round smooth rotor and round smooth stator. The calculations also ignore the effect of saturation. The simplifications are not valid for the generator simulated in the thesis, but the calculation should nevertheless give an indication of which sidebands could appear under the different fault conditions.

3.1.1 Analysis of the Eccentricity Fault Signatures

For the eccentricity conditions, the difference in magnetic flux distribution, between a healthy and eccentric generator, is caused by a difference in the air-gap geometry. Therefore, the air-gap geometry of the eccentric generator is calculated first. The calculations use the simplification of a smooth round rotor, and a smooth round stator, and are based on the calculations presented in [21], but calculated based on the air-gap geometry for the static eccentricity shown in figure 3.2.

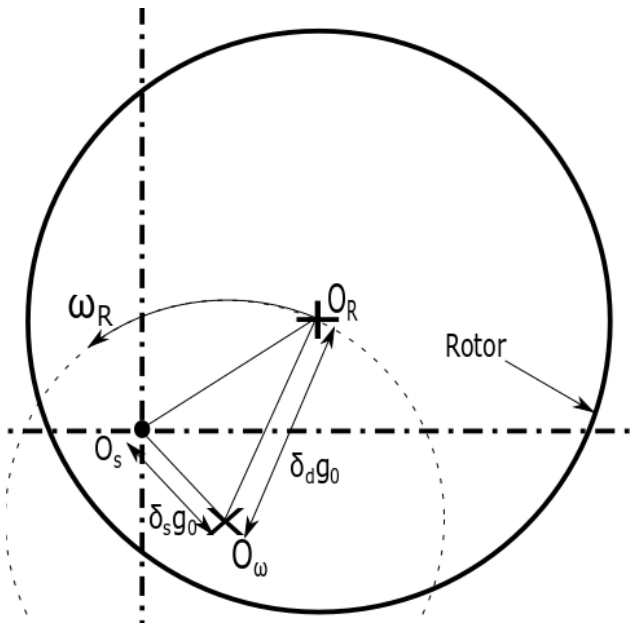

Figure 3.1: Illustration of a case of general mixed eccentricity.

The figure shows the rotational axis O_ω, rotor symmetry axis O_r and stator symmetry axis O_s in mixed eccentricity.

With reference to figure 3.1 the degree of static eccentricity δ_s and the degree of dynamic eccentricity δ_d can be defined as $\delta_s = \frac{|O_s O_\omega|}{g_o}$ [5] and $\delta_d = \frac{|O_\omega O_R|}{g_o}$ [5]. The angle between the vectors $\overrightarrow{O_s O_\omega}$ and $\overrightarrow{O_\omega O_R}$ are the static and dynamic eccentricity angles, respectively [21]. The geometry of

a generator experiencing static eccentricity shown in figure 3.2. Here the static eccentricity angle is set to zero, which is a valid assumption because the starting point of the reference frame, which defines the x-axis, is arbitrary.

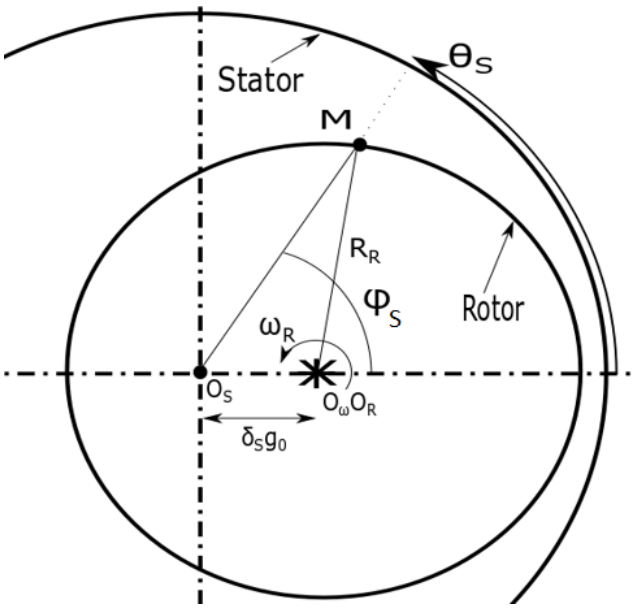

Figure 3.2: Illustration of the air-gap geometry in a generator with static eccentricity.

From figure 3.2 the distance between the stator centre and an arbitrary point M on the rotor surface can be expressed as:

$$O_sM = \delta_s g_0 \cos(\psi_s) + \sqrt{R_R^2 - \delta_s^2 g_0^2 \sin(\psi_s)}, \tag{5}$$

where R_R is the rotor radius and g_0 is the nominal air-gap in a healthy generator. The airgap length in this generator for a specific ψ_s, would be:

$$g_s(\psi_s) = R_s - O_sM$$
$$= R_s - \delta_s g_0 \cos(\psi_s) - \sqrt{R_R^2 - \delta_s^2 g_0^2 \sin(\psi_s)}, \quad (6)$$

where R_s is inner radius of the stator bore. In hydroelectric generators the radius of the rotor is much larger than the airgap length, which means the following assumption is valid:

$$\sqrt{R_R^2 - \delta_s^2 g_0^2 \sin(\psi_s)} \approx R_R. \quad (7)$$

Combining equation 5 and 7 yields the air-gap of the machine to be:

$$g_s(\psi) \approx R_s - \delta_s g_0 \cos(\psi_s) - \sqrt{R_R^2} = g_0(1 - \delta_s \cos(\psi_s)). \quad (8)$$

For the case of static eccentricity, it can be seen from figure 3.2, that $\psi = \theta_s$, where θ_s is the stator reference angle. This will result in the air-gap length distribution of a generator with static eccentricity seen from the stator frame reference:

$$g_s(\theta_s) = g_0(1 - \delta_s \cos(\theta_s)), \quad (9)$$

matching the air-gap length distribution for static eccentricity stated in [22].

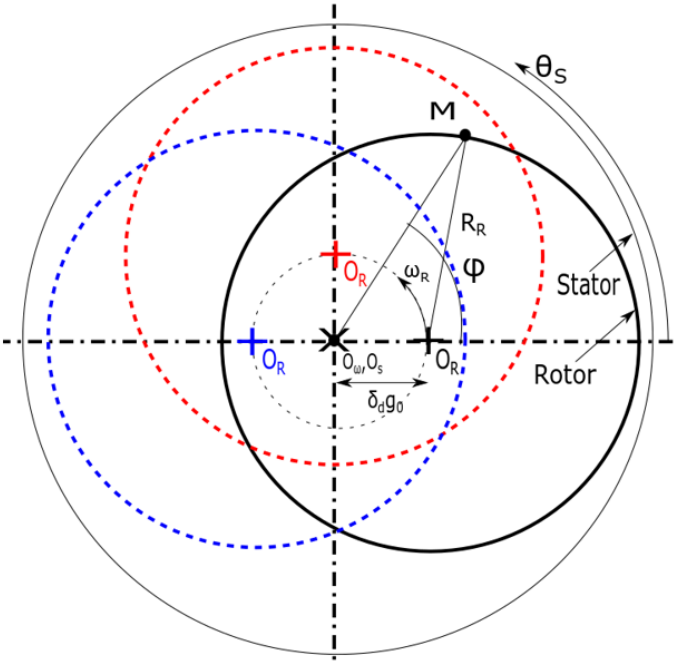

Figure 3.3: Illustration of the air-gap geometry in a generator with dynamic eccentricity.

Figure 3.3 illustrates the geometry of a generator experiencing dynamic eccentricity, doing the same calculations as for the static eccentricity, the air-gap length distribution for dynamic eccentricity is found to be:

$$g_d = g_0(1 - \delta_d \cos(\psi_d)), \tag{10}$$

For dynamic eccentricity seen from the stator frame reference, it can be seen that the air-gap length at a fixed stator angle θ_s^* is:

$$g_d\big(\theta_s^*(t_2)\big) = g_d\big(\theta_s^*(t_1) - \omega_R(t_2 - t_1)\big), \tag{11}$$

where ω_R is the mechanical rotor rotational speed. This means that $\psi_d = \theta_s - \omega_R t$. we have that $\omega_R = \frac{\omega_s}{P}$ [23], where ω_S is the electrical rotational

speed and P is the number of pole pairs. This gives the air-gap length distribution for dynamic eccentricity to be:

$$g_d = g_0\left(1 - \delta_{\mathrm{d}}\cos\left(\theta_s - \frac{\omega_s t}{P}\right)\right) = g_0\left(1 - \delta_d\cos\left(\frac{\omega_s t}{P} - \theta_s\right)\right), \tag{12}$$

matching the air-gap length distribution for dynamic eccentricity stated in [24].

With the air-gap length distribution for static and dynamic eccentricity calculated, the subchapter will continue by calculating the magnetic field in the air-gap, starting with dynamic eccentricity. The calculations are based on the calculation done in [25], and ignores the effect of saturation and the damper bars. If we assume the that the magnetic flux crosses the air-gap as it would in the case of a healthy generator, even though we have eccentricity, then the magnetic field in the air-gap is [25]:

$$B_S(\theta_s, t) = \Lambda(\theta_s, t)\int j_s(\theta_s, t)d\theta_s, \tag{13}$$

where Λ is the airgap permeance and $j_s(\theta_s, t)$ is the current density on the inner surface of the stator. Assuming sinusoidal variations in the stator MMF wave, $j_s(\theta_s, t)$ will be [17]:

$$j_s(\theta_s, t) = J_s\sin(\omega_s t - P\theta_s), \tag{14}$$

where J_s is the peak of the current density. Based on the calculated air-gap given in equation 12, the permeance in the case of dynamic eccentricity, Λ_d will be:

$$\Lambda_d(\theta_s, t) = \frac{\mu_0}{g_d(\theta_s, t)} = \frac{\mu_0}{g_0\left(1 - \delta_\mathrm{d}\cos\left(\frac{\omega_s t}{P} - \theta_s\right)\right)}, \tag{15}$$

where μ_0 is the permeability of free space. The permeance $\Lambda_d(\theta_s, t)$ can be expressed as the following power series [24]:

$$\Lambda_d(\theta_s, t) = \frac{\mu_0}{g_0}\left(1 + \delta_\mathrm{d}\cos\left(\frac{\omega_s t}{P} - \theta_s\right) - \frac{\left(\delta_\mathrm{d}\cos\left(\frac{\omega_s t}{P} - \theta_s\right)\right)^2}{2} + \frac{\left(\delta_\mathrm{d}\cos\left(\frac{\omega_s t}{P} - \theta_s\right)\right)^3}{6} - \cdots + \right). \tag{16}$$

Focusing on the first two terms and ignoring the rest, their effect will be included later. $\Lambda_d(\theta_s, t)$ becomes:

$$\Lambda_d = \frac{\mu_0}{g_0}\left(1 + \delta_d \cos\left(\frac{\omega_s t}{P} - \theta_s\right)\right). \tag{17}$$

By combining equation 13, 14 and 17 the magnetic field in the airgap becomes:

$$B_s = \frac{\mu_0}{g_0}\left(1 + \delta_d \cos\left(\frac{\omega_s t}{P} - \theta_s\right)\right) J_s \int \sin(\omega_\mathrm{s} t - P\theta) d\theta_s, \tag{18}$$

$$B_s = \frac{\mu_0 J_s}{g_0}\left(1 + \delta_d \cos\left(\frac{\omega_s t}{P} - \theta_s\right)\right) \cos(\omega_s t - P\theta_s). \tag{19}$$

With the sinusoidal identity:

$$2\cos(A)\cos(B) = \cos(A-B)\cos(A+B), \tag{20}$$

equation 19 can be rewritten as:

$$\begin{aligned} B_S = \frac{\mu_0 J_S}{g_0}\cos(\omega_s t - P\theta_s) \\ + \frac{\mu_0 J_S \delta_d}{2g_0}\cos\left(\left(1+\frac{1}{P}\right)\omega_s t - (P+1)\theta_s\right) \\ + \frac{\mu_0 J_S \delta_d}{2g_0}\cos\left(\left(1-\frac{1}{P}\right)\omega_s t - (P-1)\theta_s\right). \end{aligned} \tag{21}$$

By including more of the terms from the series given in equation 16, the magnetic field would become [24]:

$$\begin{aligned} B_{S,dynamic} = B_0\cos(\omega_s t - P\theta_s) \\ + \sum_{n=1}^{\infty} \mathrm{B}_{\mathrm{n,d}}^{+}\cos\left((1+\frac{n}{P})\omega_s t - (P+n)\theta_s\right) \\ + \sum_{n=1}^{\infty} \mathrm{B}_{\mathrm{n,d}}^{-}\cos\left((1-\frac{n}{P})\omega_s t - (P-n)\theta_s\right), \end{aligned} \tag{22}$$

where n=1,2,3… The expression for magnetic flux density is the same as calculated in [24].

Doing the same calculations for the static eccentricity condition, by basing the calculations on the air-gap described by equation 9. The resulting magnetic field in the static eccentricity condition is:

$$B_{S,static} = B_0 \cos(\omega_s t - P\theta_s) + \sum_{n=1}^{\infty} \mathrm{B}_{\mathrm{n,s}}^{+} \cos(\omega_s t - (P+n)\theta_s) + \sum_{n=1}^{\infty} \mathrm{B}_{\mathrm{n,s}}^{-} \cos(\omega_s t - (P-n)\theta_s), \tag{23}$$

where n=1,2,3…

According to [22] the flux in case of mixed eccentricity is approximately equal to the effect of static and dynamic eccentricity superimposed onto the healthy flux. This means that equations 22 and equation 23 give the magnetic flux density for the mixed eccentricity case to be:

$$B_{S,mixed} = B_0 \cos(\omega_s t - P\theta_s) + \sum_{n=1}^{\infty} \mathrm{B}_{\mathrm{n,d}}^{-} \cos\left((1+\frac{n}{P})\omega_s t - (P+n)\theta_s\right) + \sum_{n=1}^{\infty} \mathrm{B}_{\mathrm{n,d}_{\mathrm{d}}}^{-} \cos\left((1-\frac{n}{P})\omega_s t - (P-n)\theta_s\right) + \sum_{n=1}^{\infty} \mathrm{B}_{\mathrm{n,s}}^{+} \cos(\omega_s t - (P+n)\theta_s) + \sum_{n=1}^{\infty} \mathrm{B}_{\mathrm{n\,s}}^{-} \cos(\omega_s t - (P-n)\theta_s). \tag{24}$$

Looking at equation 22 and 24 it's clear that the dynamic and mixed eccentricity will produce harmonic waves with the frequency pattern:

$$f_{harmonics} = \left(1 \pm \frac{n}{P}\right) f_s, \tag{25}$$

where f_s is the synchronous electrical frequency and n=1,2,3,... The harmonics which do not overlap with harmonics produced by a healthy generator:

$$f_{harmonic,healthy} = nf_s, \tag{26}$$

where n=1,2,3,…, Will be the harmonic sidebands which may be detected by the proposed detection method.

The magnetic field for the static eccentricity condition does not have the same characteristic and will likely not produce any sidebands which could be detected with the proposed method.

3.1.2 Analysis of the Rotor Interturn Short Circuit Signature

The interturn short circuit of one or multiple turns within one of the rotor excitation windings, makes the flux distribution in the generator asymmetrical. As stated by [16], by neglecting the effect of magnetic saturation, the effect of the shorted turn can be seen as the effect of superimposing a fictitious coil onto the field of a healthy generator. To calculate the effects of rotor ITSC, a simple model of the generator was made, shown in figure 3.4. The model contains the MMF produced by the generator's eight poles and spans the entire 360° of the rotor. The simplification done in the model is that the poles produce a constant MMF over the entire pole span, and that the poles are directly adjacent to each other. These assumptions are not valid for the real generator. The poles are separated and the MFF will vary over the pole span, because of the distance between poles, the pole saliency, the shape of the pole, etc. The model

should however give an indication of the relation between the harmonics produced the rotor ITSC and the first harmonic of the healthy generator.

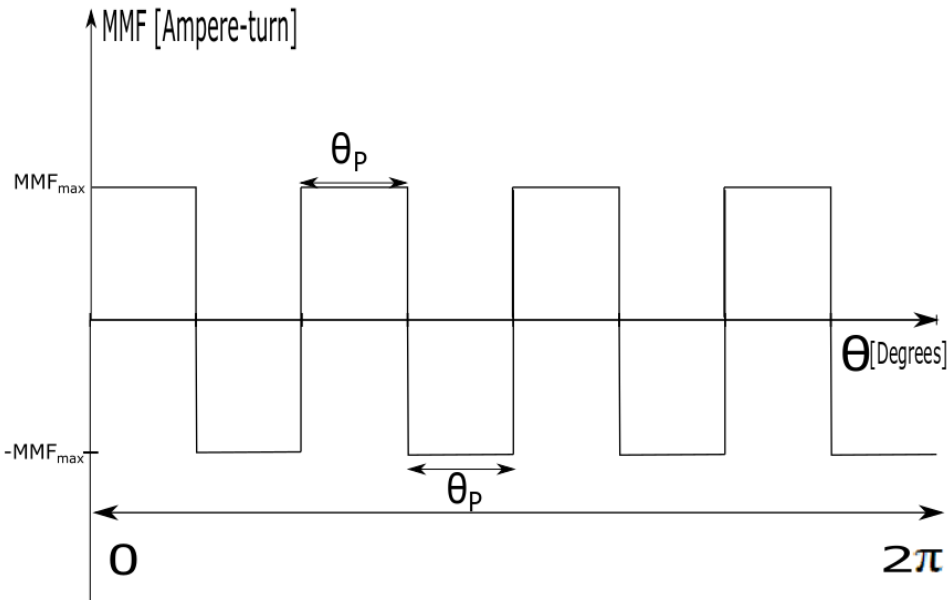

Figure 3.4: Model of the MMF produced by the rotor, seen from the rotor reference.

The model contains eight poles and spans entire 360° of the rotor surface.θ_P is the span of one pole.

The model for the fictitious coil was created based on the procedure given in [26] and the simplified model shown in figure 3.4. The fictitious coil model is shown in figure 3.5. The values C_1 and C_2 are calculated in [26] for the model used there, and are calculated based on the model geometry, the current reduced by the shorted turns and the principle that the upper and the lower magnetic potential is equal, meaning that area A is equal area B. C_1 and C_2 were not calculated in this thesis because it is mainly interested in the frequencies. They are non-zero and proportional with the number of shorted turns, so they will not disrupt the rest of the calculation. X is here

the half the pole span of one pole given in figure 3.4, which means the effect of one short circuit, effects the whole pole span of the faulty pole.

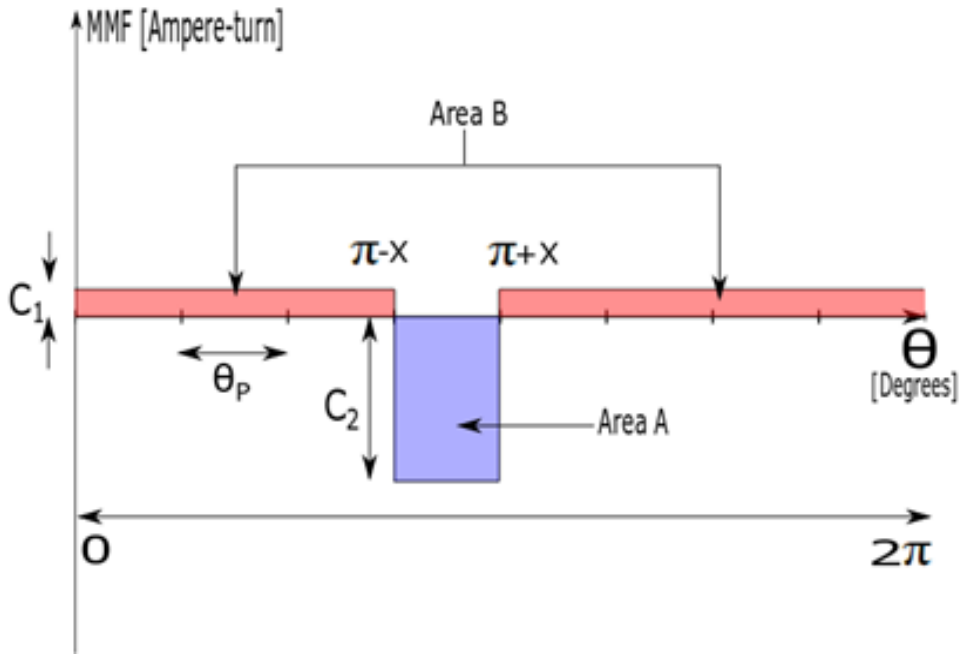

Figure 3.5: The produced MMF of the fictitious coil, simulating the effect of a rotor ITSC fault.

Seen from the rotor reference.

To find the harmonics produced by the fictitious coil, the Fourier series of the fictitious coil model was calculated, the Fourier series will have the shape of: $MMF_{fictitious} = A_0 + \sum_{n=1}^{\infty} A_n \cos(n\theta) + \sum_{n=1}^{\infty} B_n \sin(n\theta)$ [27]. The calculation of the coefficients are given below:

$$A_0 = \frac{1}{2\pi}\int_0^{2\pi} MMF_{ficitious}(\theta)$$

$$= \frac{1}{2\pi}\left(\int_0^{\pi-x} C_1 d\theta - \int_{\pi-x}^{\pi+x} C_2 d\theta + \int_{\pi+x}^{2\pi} C_1 d\theta\right), \tag{27}$$

$$A_0 = \frac{1}{2\pi}\left([C_1\theta]_0^{\pi-x} + [C_1\theta]_{\pi+x}^{2\pi} - [C_0\theta]_{\pi-x}^{\pi+x}\right) = Area\ B - Area\ A = 0. \tag{28}$$

$$A_n = \frac{1}{\pi}\int_0^{2\pi} MMF_{ficitious}(\theta)\cos(n\theta)$$

$$= \frac{1}{\pi}\left(\int_0^{\pi-x} C_1\cos(n\theta)d\theta - \int_{\pi-x}^{\pi+x} C_2\cos(n\theta)d\theta + \int_{\pi+x}^{2\pi} C_1\cos(n\theta)d\theta\right), \tag{29}$$

$$A_n = \frac{1}{2\pi}\left(\left[\frac{C_1\sin(n\theta)}{n}\right]_0^{\pi-x} - \left[\frac{C_2\sin(n\theta)}{n}\right]_{\pi-x}^{\pi+x} + \left[\frac{C_1\sin(n\theta)}{n}\right]_{\pi+x}^{2\pi}\right), \tag{30}$$

$$A_n = \frac{1}{\pi}\left(C_1\left(\sin\left(n(\pi-x)\right) - \sin\left(n(\pi+x)\right)\right) + C_2\left(\sin\left(n(\pi-x)\right) - sin\left(n(\pi+x)\right)\right)\right). \tag{31}$$

The sinusoidal identity of:

$$\sin\big(n(\pi - x)\big) - \sin\big(n(\pi + x)\big) = -2\cos(n\pi)\sin(nx) \\ = 2(-1)^{n+1}\sin(nx), \tag{32}$$

for n=1,2,3... gives:

$$A_n = \frac{2(C_1 + C_2)}{n\pi}(-1)^{n+1}\sin(nx). \tag{33}$$

$$\begin{aligned} B_n = \frac{1}{\pi}\int_0^{2\pi} MMF_{ficitious}(\theta)\sin(n\theta) \\ = \frac{1}{\pi}\Big(\int_0^{\pi-x} C_1\sin(n\theta)d\theta \\ - \int_{\pi-x}^{\pi+x} C_2\sin(n\theta)d\theta \\ + \int_{\pi+x}^{2\pi} C_1\sin(n\theta)d\theta\Big) \end{aligned} \tag{34}$$

$$\begin{aligned} B_n = \frac{1}{\pi}\Big(C_1\Big(\cos\big(n(\pi - x)\big) - \cos\big(n(\pi - x)\big)\Big) \\ - C_2\Big(\cos\big(n(\pi - x)\big) - \cos\big(n(\pi - x)\big)\Big)\Big). \end{aligned} \tag{35}$$

The sinusoidal identity of:

$$\Big(\cos\big(n(\pi - x)\big) - \cos\big(n(\pi - x)\big)\Big) = 0, \tag{36}$$

for all n=1,2,3… gives: $B_n = 0$. The result of the Fourier series is:

$$MMF_{ficitious}(\theta) = \sum_{n=1}^{\infty} A_n \cos(n\theta)$$

$$= constant * \sum_{n=1}^{\infty} \frac{\sin(nx)}{n} \cos(n\theta), \tag{37}$$

$$\begin{aligned} MFF_{fictitious}(\theta) \\ &= F_1 \cos(\theta) + F_2 \cos(2\theta) \\ &+ F_3 \cos(3\theta) \\ &+ F_4 \cos(4\theta) + F_5 \cos(5\theta) + F_6 \cos(6\theta) \\ &+ \cdots \end{aligned} \tag{38}$$

To find the first harmonic of the healthy model its Fourier series was calculated from the simplified model, shown in figure 3.4. The calculation is shown in Appendix C. The result of the calculation showed the first harmonic to be:

$$MMF_{healthy,first\ harmonic} = -\frac{4}{\pi} \sin(4\theta). \tag{39}$$

The first harmonic of the healthy MMF is the fundamental harmonic of the generator. Comparing the MMF harmonics of the fictitious coil, we see that the rotor ITSCs first harmonic, $F_1 \cos(\theta)$, travels four times faster than the fundamental, the second rotor ITSC harmonic, $F_2 \cos(2\theta)$, travels twice as fast, and so on. The frequency pattern of the rotor ITSC becomes:

$$f_{rotor\ ITSC} = \left(1 \pm \frac{k}{4}\right) f_s, \tag{40}$$

where $k = 1,2,3$ ... The number of pole pairs are 4, and based on our model and calculations the general expression would be:

$$f_{rotor\ ITSC\ sidebands} = \left(1 \pm \frac{k}{P}\right) f_s, \tag{41}$$

where k=1,2,3…

The found harmonic sideband pattern matches the proposed harmonic sideband pattern for rotor ITSC in [1] and magnetic defect in the rotor in [19]. The magnetic defect is similar to a rotor ITSC in that reduces the produced MMF of one pole.

The thesis also looks into the methods ability to detect rotor ITSC with static eccentricity. The pattern which this fault case would produce is assumed to be similar to that produced by mixed eccentricity. This is because rotor ITSC and dynamic eccentricity produces similar effects on the air-gap magnetic flux, both producing a magnetic flux with one peak value which rotates with the rotor. Therefore. combining rotor ITSC with static eccentricity, should be similar to combining dynamic eccentricity with static eccentricity. Therefore, the assumed frequency pattern for rotor ITSC with static eccentricity, based on equation 24, is:

$$f_{rotor\ ITSC\ with\ static\ eccentricy,sidebands} = \left(1 \pm \frac{k}{P}\right) f_s, \tag{42}$$

where k=1,2,3,…

4 Finite Element Modelling and Simulations

To study the effect of the fault conditions mentioned in chapter 2.2 and 2.3, TSFE-simulations were performed on 2D models of hydro generators. Four healthy generator models were created. The first was created based on technical drawings of a real hydro generator, the resulting model is shown figure 4.1 and its general information is shown in table 4.2. The second, third and fourth, was based on the first model, but with a change in the topology. The second has a reduced number of stator slots from 126 to 120, effectively changing the generator from a fractional slot machine into an integer slot machine, the 120-slot generator is shown in Appendix A.1. The third model has increased the slot pitch from 13 to 15. The fourth had the number of slots reduced to 114, shown in Appendix A.2. The models with modified topology was created to study the effect that the topology change has on fault signatures, therefore no other variable within the machine was changed. The first, second, third and fourth model will hereafter be referred to as Machine 1, Machine 2, Machine 3 and Machine 4 respectively. The differences between the models are shown in table 4.1.

The choice of a 2D model over a 3D model is based on the fact that a 3D model has a much longer computational time than a 2D model, this thesis has also been limited to fault conditions which are assumed symmetrical in axial-direction, making the 2D model the preferred approach. To further improve the computational time, the core and eddy current losses and eddy current effects in all other elements than for the damper bars was not simulated. This simplification is based on the assumption that the core losses and eddy current effects will have minimal impact on the fault induced harmonic spectrum. Another effect which was excluded from the

model was the effect of the cooling channels in the stator core. The result is that the real generator compared to the simulation may be more affected by saturation than what the results of simulations might imply.

The rest of this chapter describes how the healthy model was created and then how the fault conditions were modelled.

Table 4.1: Differences between the four models.

Machine	1	2	3	4
Number of slots [#]	126	120	126	114
Slot pitch	13	13	15	13

Table 4.2: General generator information.

Machine	1
Nominal effect	22 [MVA]
Nominal voltage	7.7 [kV]
Nominal current	1.65 [kA]
Number of poles	8
Number of damper bars per pole	8
Number of slots	126
Stator winding connection	Wye
Winding layout	Double-layered
Frequency, f_s	50 [Hz]
Outer rotor radius, R_R	997 [mm]
Outer stator radius	1320 [mm]
Generator length	1320 [mm]
Nominal air-gap, g_0	23 [mm]

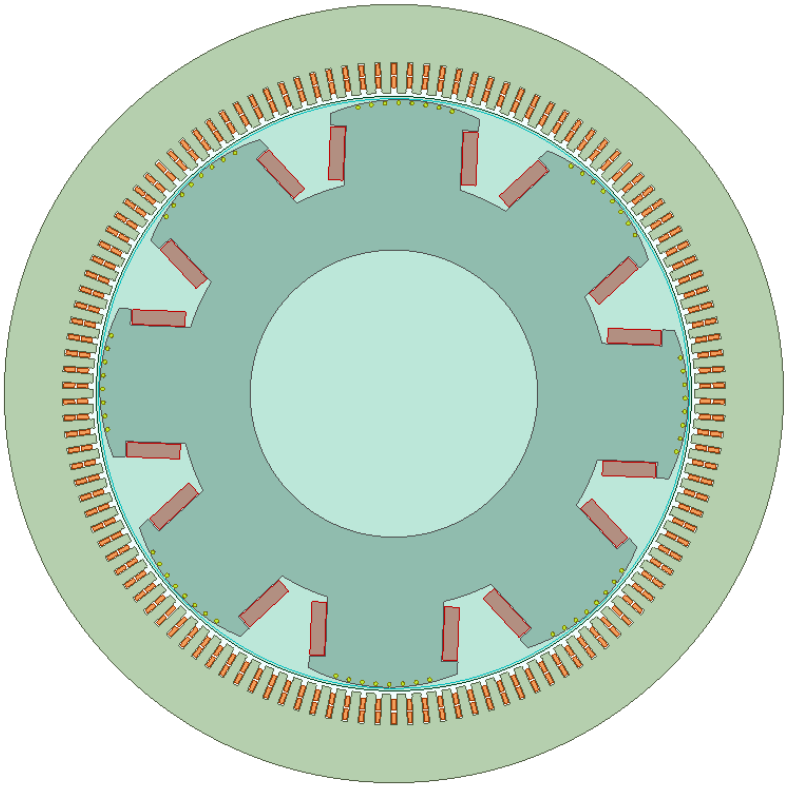

Figure 4.1: Picture of the FEM of the healthy generator, Machine 1.

4.1 Modelling of the Healthy Generator

This subchapter describes the modelling of Machine 1, the model based of the technical drawings, in healthy condition. Machine 2, Machine 3 and Machine 4 were created in the same way but with 120 slots instead of 126 slots for Machine 2, with a pole pitch of 15 instead of 13 for Machine 3 and with 114 slots instead of 126 slots for Machine 4.

4.1.1 Stator

The stator was created utilizing one of Ansys Maxwell's "user defined primitives" (UDP). UDP is a geometric modelling command in Ansys Maxwell, which recreates a pre-defined geometry based on user input values [28]. For the stator the UDP "SlotCore" was chosen and the input values can be seen in Appendix A.3, Appendix A.4 and A.5 shows the input values for Machine 2 and Machine 4. The stator was assigned the material property of M300-35A steel, which magnetically properties can be seen in appendix B.1. The choice of material is based on the fact that M300-35A steel has similar properties to the type of steel used in stator laminations [29] and has successfully been used in similar simulations [1].

4.1.2 Stator Windings

The stator windings are modelled as solid rectangles. This is a simplification seeing as the coils in the stator windings are made up of several strands. The simplification will however not influence the amount of total current flowing within each winding, since effect of the stranded coils were accounted for in the modelling. Since the machines have a doubled-layered winding layout, each slot contains two rectangles. The insulation and slot wedge have little effect on the magnetic fields which are of interest in this study and was therefore simply modelled as air.

The winding layout can be found by calculating the q, which is the slots per pole per phase, as given by equation 43 [20], and the knowledge that the machines are three-phase doubled-layered machine with a slot pitch of 13, 15 for Machine 3.

$$q = \frac{N_s}{3 * N_p}, \tag{43}$$

where N_s is the number of slots and N_p is the number of poles. For Machine 1 and 3 $q_{1,3} = 5 + \frac{1}{4}$, $q_2 = 5$ for Machine 2 and $q_4 = 4 + \frac{3}{4}$ for Machine 4. The resulting winding layouts are shown in Appendix A.6. The rectangles were assigned excitations, matching the winding layout shown in Appendix A.6. The rectangles were assigned the material property of copper.

4.1.3 Rotor

The rotor was modelled utilizing the UMP "SalientPoleCore", with the input values given in appendix A.7. The rotor was assigned the material property of steel 1010, which is a pre-defined material property within Ansys Maxwell. Steel 1010 is of a lower quality than M300-35A, which is realistic since the stator normally has better quality steel [29], Steel 1010 has also successfully been used in similar models [1]. Steel 1010 magnetic properties can be seen in appendix B.2.

4.1.4 Rotor Winding

The rotor winding are modelled as two solid rectangles on each side of the eight poles. This is the same simplification as made for the stator winding, seen as the rotor winding also are made up of several turns. The simplification does however not influence the amount of current following flowing around each pole, because of the homogeneous current coming

from the DC-supply. The insulation for the rotor windings were simulated as air-gaps with the same argument for the simplification as that given for the stator windings in chapter 4.1.2. The rectangles are given the material property of copper. Each rectangle is given an individual current excitation, with a current direction in such a way that following the right-hand rule, each pole has both its neighbouring poles with the opposite polarity.

4.1.5 Damper Bars

The damper bars were modelled as solid circles placed within the rotor damper bar slots. The damper bars were all excited by a single "end_connection"-excitation. The "end_connection"-excitation connects all the elements into a parallel. This effectively connects all the damper bars in parallel like they are in the technical drawings. The material property was set to copper. Eddy effect simulation was activated for the damper bar circles, which means that the effects of eddy current was simulated in the damper bars.

4.1.6 Boundary, Air-gap and Motion Setup.

The outer edge of the stator was given the boundary condition of zero flux penetration, thereby making the assumption that the magnetic flux escaping the stator is so small it is neglectable. This assumption is valid as long as the stator is not saturated, which did not happen during the simulations.

A circle with a radius equal to the outer stator radius was made and assigned the material property of air, effectively making the parts of the generator not assigned a material into air. This was done to simulate the air in the air-gap of the machine.

A circle encapsulating the rotating parts of the machine was created. The circle represents the band required by the software to differentiate between

moving and stationary parts of the model. This circle will hereafter be referred to as the band. A rotational motion setup was assign to the band. The rotating axis of the model was set to be the z axis of the global coordinate system, effectively making the stator, rotor and rotational centre equal. The rotational speed, calculated utilizing equation 44, was set to 750 rpm [23].

$$n_S = \frac{120 f_e}{P}. \tag{44}$$

4.1.7 Mesh

Ansys Maxwell is a finite element method software, as such it solves the calculations by reducing the problem's geometry into discretized building blocks. The collection of the discretized building blocks is called the mesh of the problem. The static algebraic equations of the problem are solved in the connecting points of the building blocks, the values outside the points are interpolated from the neighbouring points [28]. The refinement of the mesh, i.e. the number of elements the problem geometry is reduced into, effects both the accuracy and computation time of the simulations. The finer the mesh, the more accurate the results because we have more points of calculated values. With more points, more calculations have to be performed, and the simulations time increases. Therefore, when deciding the mesh refinement both accuracy and the computational time of the simulations were taken into consideration.

The refinement of the mesh can be specified for specific areas of the problem geometry. This way the accuracy can be improved in important areas and reduced in less important areas of the geometry, optimizing the

computational time without sacrificing the accuracy in important areas. Ansys Maxwell give several methods for specifying the mesh refinement of the model [28]. The length based mesh operation was chosen for this model, the length based mesh operation gives the opportunity to specify number of elements and the maximum distance between the points within the specific parts of the geometry. Ansys Maxwell then generates a mesh following these restrictions.

The most important part for this simulation, when it comes to accuracy, is the air-gap. The less important parts are the stator and rotor core. The generator was therefore divided into three mesh sections: the stator, the rotor and the air-gap mesh-section. The specifications for these sections are shown in table 4.3, the resulting mesh shown in figure 4.2 and the number of elements for each of the sections is given in table 4.4. The mesh contains a total of 211936 elements, which was deemed sufficient. The simulations should have an acceptable accuracy in the results, with a moderate simulation time [29].

Table 4.3: Restrictions for the mesh operations.

Section	Max length between elements [mm]	Max number of additional elements [#]
Air-gap	2	90000
Stator	3.5	40000
Rotor	3.5	40000

Table 4.4: Number of mesh elements in the different components of the generator.

Area	Elements [#]
Total	211936
Air-gap	94360
Rotor	29753
Stator	71493
Rotor-, stator- and damper winding	16330

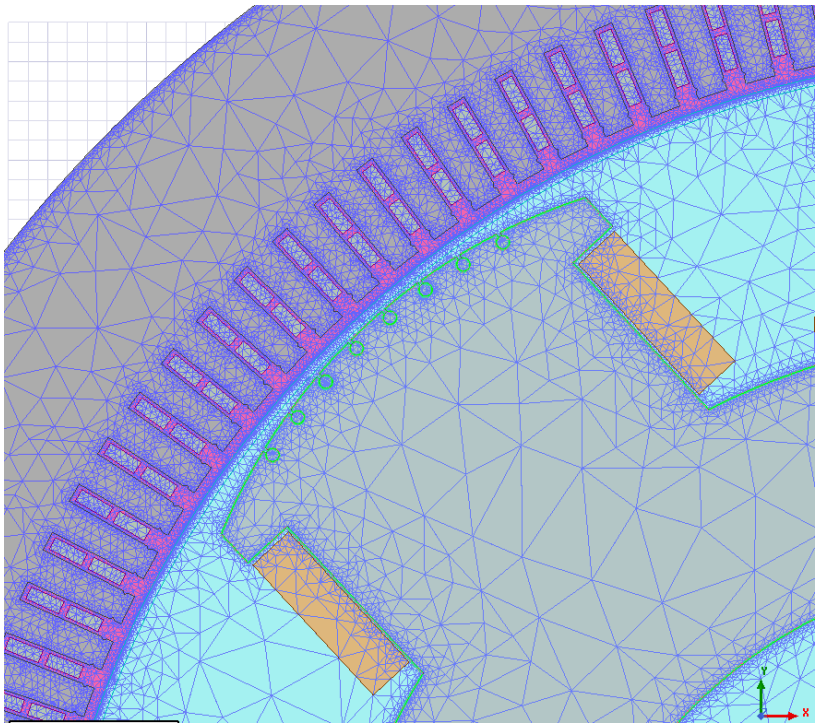

Figure 4.2: Picture of the mesh-plot.

4.1.8 Load Simulations and the External Circuit

In this thesis it was decided to look at both no-load and full-load scenarios, to see the effects the different load operations had in the produced harmonics. In the no-load simulation the excitation for the stator windings are simply set to have its currents equal zero. The field windings excitation for each pole winding was set to produce a total current of 17.4kA, simulating the effect of exciting the 58 turns of the field winding with an excitation current 300A, which was the value of the no-load excitation current given in the technical data sheets.

For the full-load there is a need to model a load connected to the generator. This was done by connecting the stator winding excitation to an external circuit. The external circuit contains three resistances and three inductances. The resistances represents the load, which in this thesis was modelled to be pure resistive. The inductances are the leakage flux inductances caused by the leakage flux of the stator end windings. Since the resistances are going to represent the full-load resistance they calculated based on the maximum power transfer theorem which results in equation 45 [30] and the inductances was calculated by equation 46, given in [31], and equation 47.

$$R_{load} = \frac{V_n}{\sqrt{3} * I_n} \approx 2.69\ \Omega, \tag{45}$$

$$X_{leakage,end-windings,pu} \approx \left(\frac{1.04 L_{ed} I_n 2P f_s}{V_n}\left(\frac{qN_t}{N_c}\right)^2\right)10^{-8}, \tag{46}$$

where V_n is the nominal voltage, I_n the nominal current, L_{ed} is the length of the endhead of the end-winding in [mm], f_S is the synchronous frequency, q is the number of slots per pole per phase, N_t is the number of turns per coil, N_c is the number of parallel circuits and P is the number of pole pairs. The leakage inductance will then be:

$$L_{leakage,end-windings} = \frac{2\pi f_s V_n}{I_n} X_{leakage,end-winding,pu} \approx 0.09mH. \quad (47)$$

The field windings excitation for each pole winding was initially set to produce a total current of 26.5kA, simulating the effect of exciting the 58 turns of the field winding with a excitation current 457 A, which was the value of the pure resistive full-load excitation current given in the technical data sheets. The results from the initial simulations with this excitation and the resistance calculated with equation 45, did however not give the nominal values given in table 4.2. The reason for this is most likely that the model is not a perfect replica of the real generator and the simplifications made in the modelling, especially the exclusion of core and eddy current related losses. The excitation current and the load resistance was therefore change until the nominal values were more in line with what was given in table 4.2. The result being a full-load excitation current of 438 A (a 4% deviation from the given value) and a load resistance of 2.38 Ω. The external circuit used for the full-load simulations are shown in figure 4.3.

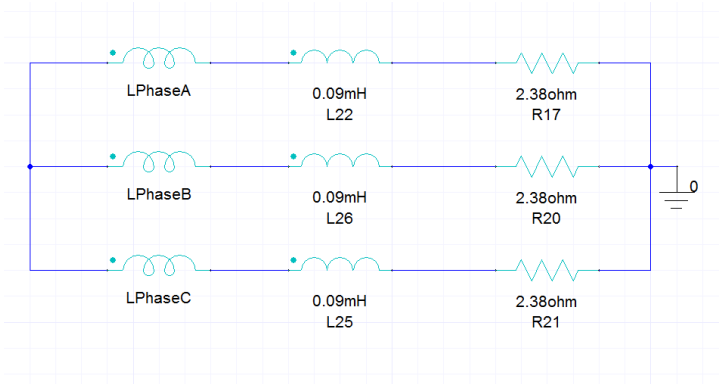

Figure 4.3: The external circuit for the full-load operation.

L22, L25 and L26 is the leakage inductances and R17, R20 and R21 is the load resistance

4.1.9 Results of the Healthy Machine Simulations.

The healthy generator was simulated for both the no-load and full-load operations. In both cases the generator gave a sinusoidal like current and voltage response, with a phase shift of 120 degrees between each phase, as shown in figure 4.4 for the voltage response for full-load operation. The full-load case reached a steady state RMS-value of ~7.67 kV (~0.4% error) for the voltage and ~1.66 kA (~0.1%) for the current, resulting in an RMS-value of ~22.05 MVA (~0.11% error) for the apparent effect. The no-load case reached a steady state RMS-value of ~7.66 kV (~0.5% $error$). The values were deemed to be within satisfactory limits and the modelling of the healthy generator was deemed acceptable.

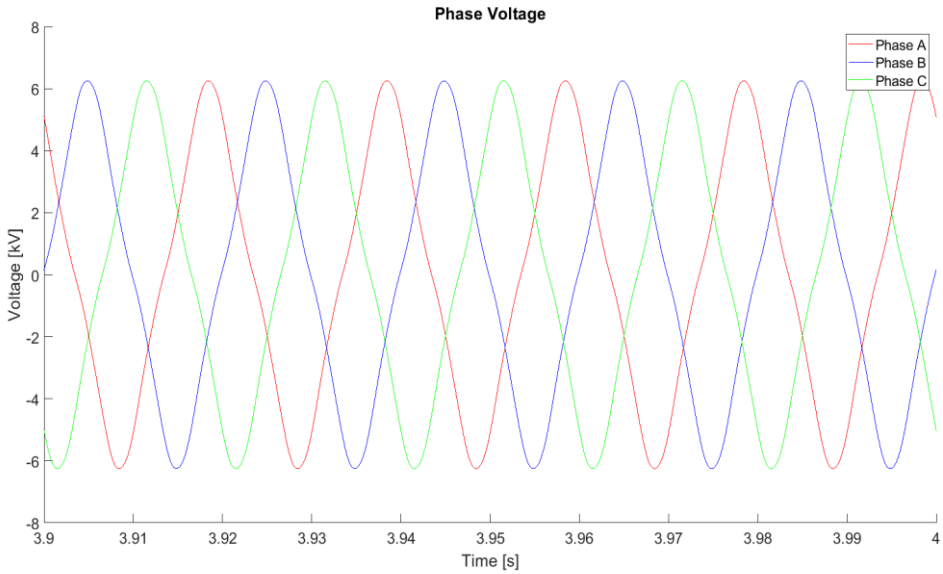

Figure 4.4: Plot of the three phase voltages from simulation done on the healthy Machine 1 model, at full-load operation.

4.2 Fault Modelling

This subchapter describes how the rotor ITSC fault with and without static eccentricity and static, dynamic and mixed eccentricity conditions were modelled. All the faults are modelled by modifying the healthy generator, described in chapter 4.1.

It is important to note that by changing the geometry, as is done when modelling for static, dynamic and mixed eccentricity, the generated mesh will be different from that of the healthy generator. Still, the specifications for the mesh operations given in table 4.3 gave mesh which was deemed satisfactory for all the simulated cases.

4.2.1 Modelling of Static Eccentricity

The modelling of the rotor static eccentricity, with the characteristics described in chapter 2.2, was done by moving all the rotating parts, i.e. the components with in the band, and the band towards one side of the stator, here chosen along the x-axis. Both the rotating parts and the band are moved with the distance $\delta_s g_0$ in the same direction. A new coordinate system was created with its centre in the centre of the now displaced band. The motion setup was changed to rotate around the z-axis of this new coordinate system. The results of the modification is a machine with a rotor centre and rotational centre which coincide, and are displaced with a fixed distance away from the stator centre. To verify the modelling of the static eccentricity, a rough simulation with a high degree of eccentricity was done. The resulting magnetic air-gap flux density as a function of stator angle is shown in figure 4.5.

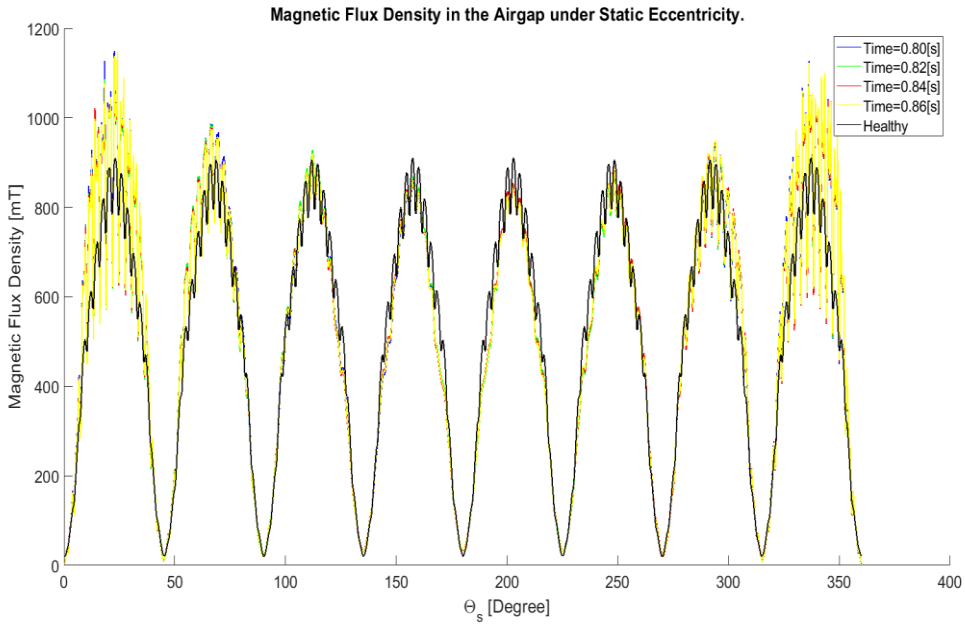

Figure 4.5: Magnetic air-gap flux density as a function of stator angle, θ_s. The figure shows plots of the generator under healthy condition(Black) and with 40% static eccentricity. The static eccentric case is shown at different timesteps T=0.80(Blue), T=0.82(green), T=0.84(yellow) and T=0.86(Red). The eight peaks are produced by the eight poles in the generator.

Figure 4.5 show the magnetic air-gap flux density for several time steps, all in steady state. The difference between the time of the plots shown in figure is a multiple of 0.2 seconds, 0.1 seconds are the time the rotor takes to rotate one whole pole span, this time difference was chosen to see if the field rotates with the rotor. From figure 4.5 it's clear to see that the eccentricity plots overlap each other, meaning that the seen from the stator side the magnetic field is time independent, i.e. the field is static. The second thing that is clear is that the field has the shape of a constant value with an added sinusoidal. The sinusoidal have one peak and one bottom

value within the span of the generator. The peak is caused by the smallest air-gap length located at $\theta_s = 0$, and the bottom value is caused by the largest air-gap length located at $\theta_s = 180°$. These characteristics is as expected from a machine with static eccentricity, verifying the modelling.

4.2.2 Modelling of Dynamic Eccentricity

The modelling of the dynamic eccentricity, with the characteristics described in chapter 2.2, was done by moving the rotating parts towards one side of the stator, here chosen along the x-axis. The rotating parts were moved with a distance $\delta_d g_0$. The radius of the band was increased to ensure that the band contained all the rotating parts. The result of the modifications is a model with rotor centre which is displaced away from the stator and rotational centre, which coincide. To verify the modelling of the dynamic eccentricity, a rough simulation with a high degree of eccentricity was done. The resulting magnetic air-gap flux density as a function of stator angle is shown in figure 4.6.

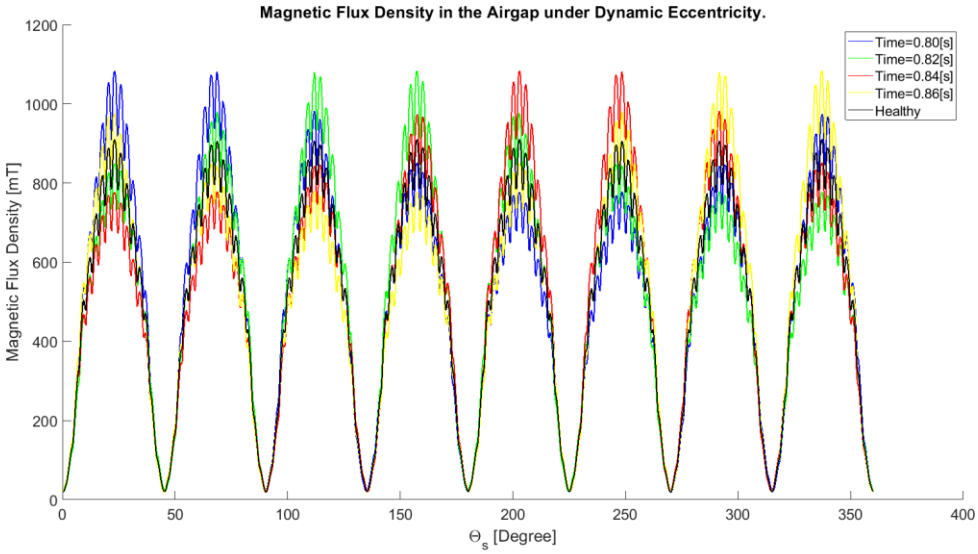

Figure 4.6: Magnetic air-gap flux density as a function of stator angle, θ_s.

The figure shows plots of the generator under healthy condition(Black) and with 40% dynamic eccentricity. The dynamic eccentric case is shown at four different timesteps T=0.80(Blue), T=0.82(green), T=0.84(yellow) and T=0.86(Red). The eight peaks are produced by the eight poles in the generator.

From figure 4.6 two things are clear. First that the magnetic air-gap flux density is time dependent, i.e. dynamic, seen by the fact that the plots taken at different times does not overlap. Second that the air-gap flux density has the shape of a constant value with an added time dependent a sinusoidal. The sinusoidal have one peak of contestant value within the span of generator, this is caused by the smallest air-gap length, with a constant distance, which rotates with the speed of rotor. These characteristics is as expected for a generator with dynamic eccentricity, therefore verifying the modelling.

4.2.3 Modelling of Mixed Eccentricity

The modelling of the mixed eccentricity, to get the air-gap characteristics as described in chapter 2.2, was done by moving the band, with a distance $\delta_s g_0$, towards the stator, here chosen along the x-axis. A new coordinate system was created with its origin on the now displaced band, and the motion setup was changed to rotate around the z-axis of this new coordinate system. The rotating parts were moved first in the same direction as band with the same distance $\delta_s g_0$, then moved again in a direction perpendicular to the previous movement, here being perpendicular to the x-axis, with the distance $\delta_d g_0$. The radius of the band were expanded to ensure all the rotating parts are encapsulated by the band. The result is a model where the stator centre, rotor centre and rotational centre were all displaced away from each other. The mixed eccentricity does not necessarily have to be model as described here, as long as the stator centre, rotor centre and rotational centre are all displaced away from one another. The described model gives an unnecessary constraint of the vector $\overrightarrow{O_s O_\omega}$ perpendicular with $\overrightarrow{O_\omega O_R}$, but the mixed eccentricity was modelled this way to have a better control of the degree of static and dynamic eccentricity within the mixed eccentricity.

To verify the modelling of the mixed eccentricity, a rough simulation with a high degree of eccentricity was done. The resulting magnetic air-gap flux density as a function of stator angle is shown in figure 4.7.

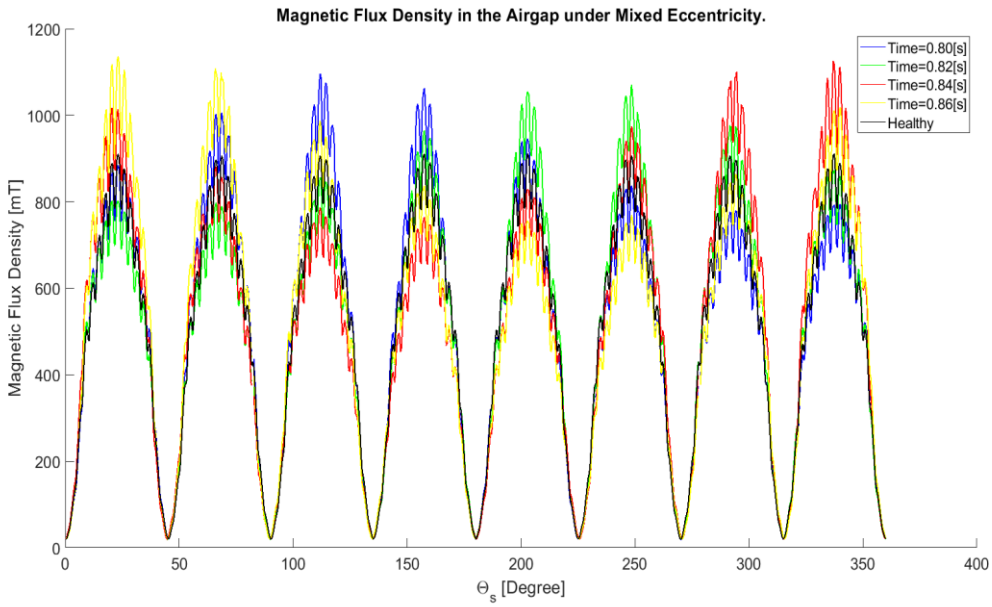

Figure 4.7: Magnetic air-gap flux density as a function of stator angle, θ_s.

The figure shows plots of the generator under healthy condition(Black) and with mixed eccentricity, consistent of 20% dynamic and 20% static eccentricity. The mixed eccentric case is shown at four different timesteps T=0.80(Blue), T=0.82(green), T=0.84(yellow) and T=0.86(Red). The eight peaks are produced by the eight poles in the generator

From figure 4.7 it can be observed that the magnetic air-gap flux density is dynamic, seen by the fact that the plots taken at different times does not overlap. It can also be seen that the magnetic air-gap flux density has the shape of a constant value with an added static sinusoidal and a dynamic sinusoidal. From the results we see peak value moves with time and varies in size, this means that the smallest air-gap length moves with the speed of rotor and varies in size. These characteristics is as expected for a generator with mixed eccentricity, therefore verifying the modelling.

4.2.4 Modelling of Rotor ITSC Faults

The rotor ITSC fault was modelled the same way as was done in [1], where the current in the rotor winding of the fault affected pole is reduced with the amount equal to that of current which should have flowed in the shorted turns if the fault was not presents. To verify the modelling of the rotor ITSC, a rough simulation with a high number of shorted turns was done. The resulting magnetic air-gap flux density as a function of stator angle is shown in figure 4.8.

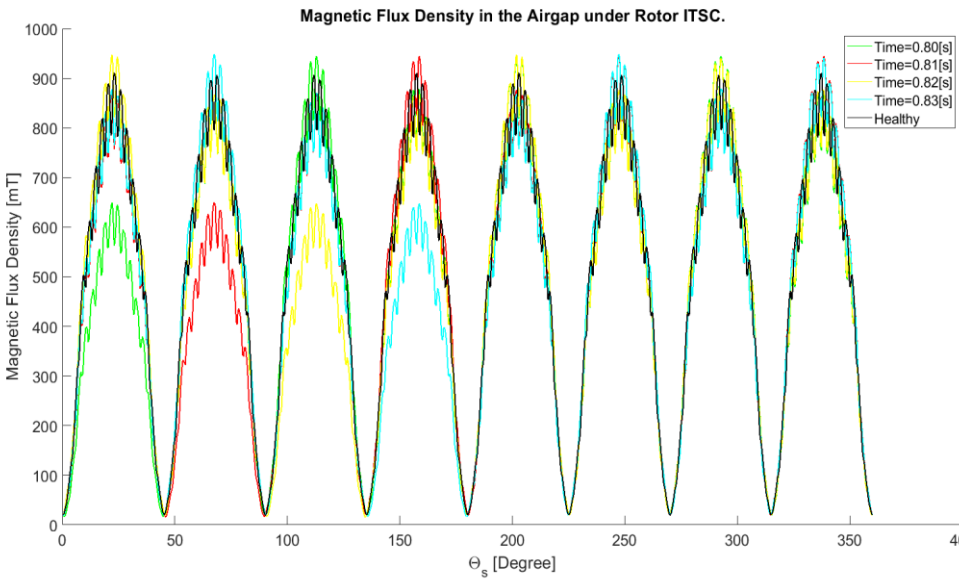

Figure 4.8: Magnetic air-gap flux density as a function of stator angle, θ_s. The figure shows plots of the generator under healthy condition(black) and with a rotor ITSC fault shorting 20 turns. The rotor ITSC fault case is shown at four different timesteps T=0.80(green), T=0.81(red), T=0.82(yellow) and T=0.83(cyan). The eight peaks are produced by the eight poles in the generator.

From figure 4.8 it can be observed that the magnetic air-gap flux density is dynamic, seen by the fact that the plots taken at different times does not overlap. The lowest peak, the one produced by the faulty pole, rotates with

the speed of the rotor. It can also be observed that field over the poles, with a polarity opposite that of the faulty pole, have a reduced peak compared to the healthy case, and the poles with the same polarity have a higher peak. These are the expected characteristics of the rotor ITSC fault verifying the modelling. Similar results were found in [1].

4.2.5 Modelling of Rotor ITSC Fault with Static Eccentricity

The modelling of the Rotor ITSC with static eccentricity was done by modelling a machine with static eccentricity as described in 4.2.1 and then model the faulty pole as described in chapter 4.2.4. To verify the modelling, a rough simulation with a high fault severity was done. The resulting magnetic air-gap flux density as a function of stator angle is shown in figure 4.9.

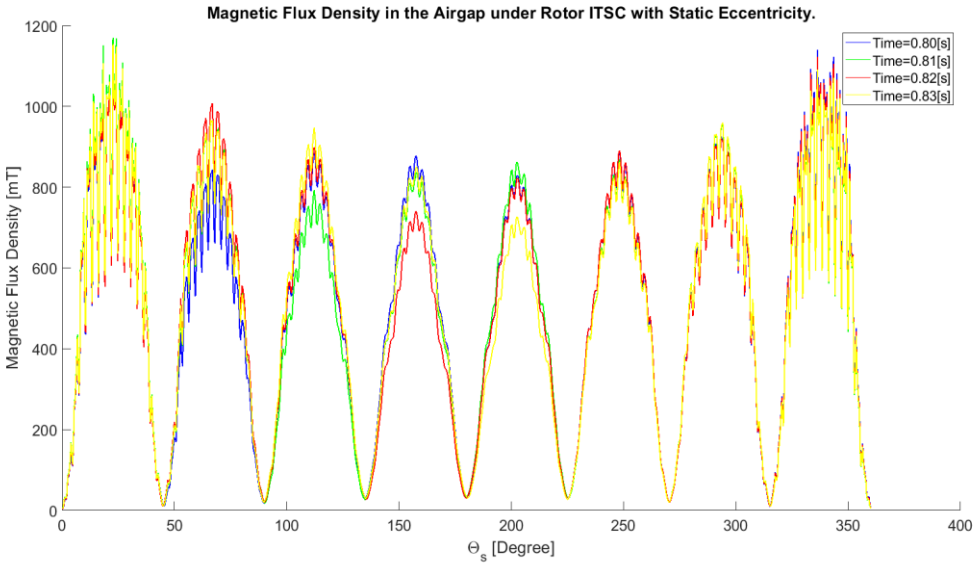

Figure 4.9: Magnetic air-gap flux density as a function of stator angle, θ_s. The figure shows plots of the rotor ITSC fault with static eccentricity case is shown at four different timesteps T=0.80(green), T=0.81(red), T=0.82(yellow) and T=0.83(cyan). The eight peaks are produced by the eight poles in the generator.

From figure 4.9 it can be observed that the magnetic air-gap flux density is dynamic, seen by the fact that the plots taken at different times does not overlap. It can also be seen that the shape of the magnetic flux is similar to that of a healthy generator with the effect of static eccentricity and rotor ITSC superimposed, which is as suspected. The sinusoidal shape is caused by the static component, and the traveling lowest peak is caused by the movement of the faulty pole. The high of the lowest peak varies with time.

5 Results of the Fault Simulations

This chapter presents the results of the TSFE-simulations of the rotor ITSC faults with and without static eccentricity, modelled as described in chapter 4.2.4 and 4.2.5. The chapter also presents the results of the static, dynamic and mixed eccentricity condition simulations, modelled as described in chapter 4.2.1, 4.2.2 and 4.2.3 respectively. The fault conditions were simulated on four different machines, that being Machine 1, 2, 3 and 4, described in chapter 4.1. The simulations were done in two different loading scenarios, that being no-load and full-load. The reason for simulating different load scenarios and machine topologies was to observe how loading and machine topology affect the fault signatures.

The results presented is the fast Fourier transformation (FFT) of the output stator phase current and stator phase voltage. The FFT requires a signal to be periodic [27]. Therefore, the simulations were run until steady state was achieved, the first second of signal after steady state was achieved was used in the FFT analysis. The result of the FFT gives the power spectra density (PSD) of the output signal, i.e. it gives the amplitude of the different frequency components the original signal is made up of [27]. Since the difference between the amplitudes of the different harmonics are very large, the results are presented in decibel normalized around the 50[Hz] amplitude. The amplitude scaling was done according to equation 48:

$$a_{f,dB} = 20\log_{10}\left(\frac{a_{f,not\ dB}}{a_{50[Hz],not\ dB}}\right)[dB], \tag{48}$$

where $a_{f,dB}$ is the amplitude of the given frequency in dB, $a_{f,not\ dB}$ is the amplitude in its original unit and $a_{50[Hz],not\ dB}$ is the amplitude of the fundamental frequency (50Hz) in its original unit.

To be able to get a good results from the FFT a high sampling frequency and signal with a long duration is required, both of which increases the computational time. A compromise between high sampling frequency and long sample duration, and a desire for short simulation time was meet with a sampling frequency of 4 [kHz] for Machine 1, 3 and 4, and 20 [kHz] for machine 2, and a signal duration of one second with steady [29]. The reason for the higher sampling frequency for machine 2 is that the change in topology gave rise to a significant ripple on the voltage signal, seen in figure 5.1. The ripple has a very high frequency, in the 1550-1800 [Hz] range. They are present in both healthy and faulty cases and therefore not fault related. The ripples disappear when the simulations are done without damper bars, see figure 5.2. Since they were not fault related, they were of no interest in this study, and are not be studied further in the thesis. The ripples did however create “fake” low frequency harmonics when the sampling frequency was too low. To avoid this machine 2 was therefore simulated with a higher sampling frequency than the rest.

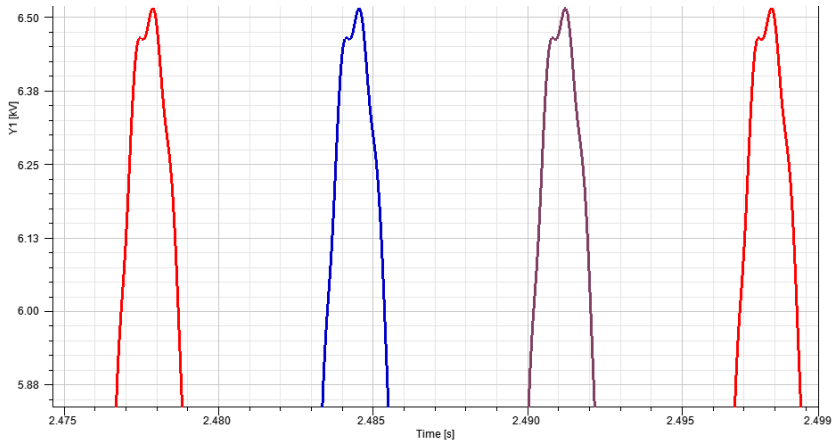

Figure 5.1: Plot showing the damper induced ripple on the phase voltage in Machine 2

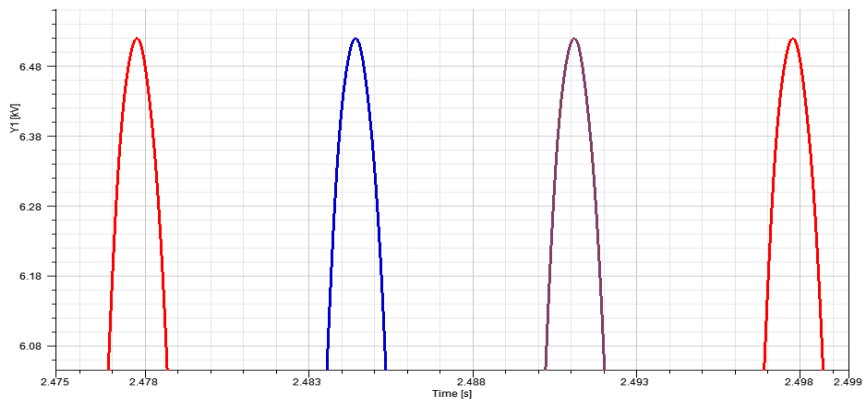

Figure 5.2: Plot of the phase voltage of Machine 2 without the damper bars.

The ripples seen in figure 5.1 are not present.

The samplings frequencies give, according to the Nyquist frequency [5], the ability to inspect frequencies up to 2 [kHz] for Machine 1, 3 and 4, and 10 [kHz] for machine 2. A quick overview of the result showed that the harmonic sidebands around the first two harmonics had the highest

amplitude. These are therefore the most relevant in regard to fault detection. Hence, to get a better resolution, the results are presented in the 0-200 [Hz] range.

5.1 Machine 1 No-load Simulation Results

5.1.1 Rotor ITSC Simulation Results

Figure 5.3 shows the frequency spectrum of the FFT analysed phase voltage of Machine 1 with varying degree of rotor ITSC, all simulated in the no-load operating condition. The figure shows clear fault induced sideband harmonics on both sides of the regular harmonics (the 50[Hz] and the 150[Hz]). The most prominent sideband harmonics are found at 25[Hz], 75[Hz], 125[Hz] and 175[Hz] frequencies. The amplitudes of the aforementioned frequencies are given in table 5.1 and the amplitude difference between the 25[Hz] and the 75[Hz] sideband harmonics are given in table 5.2.

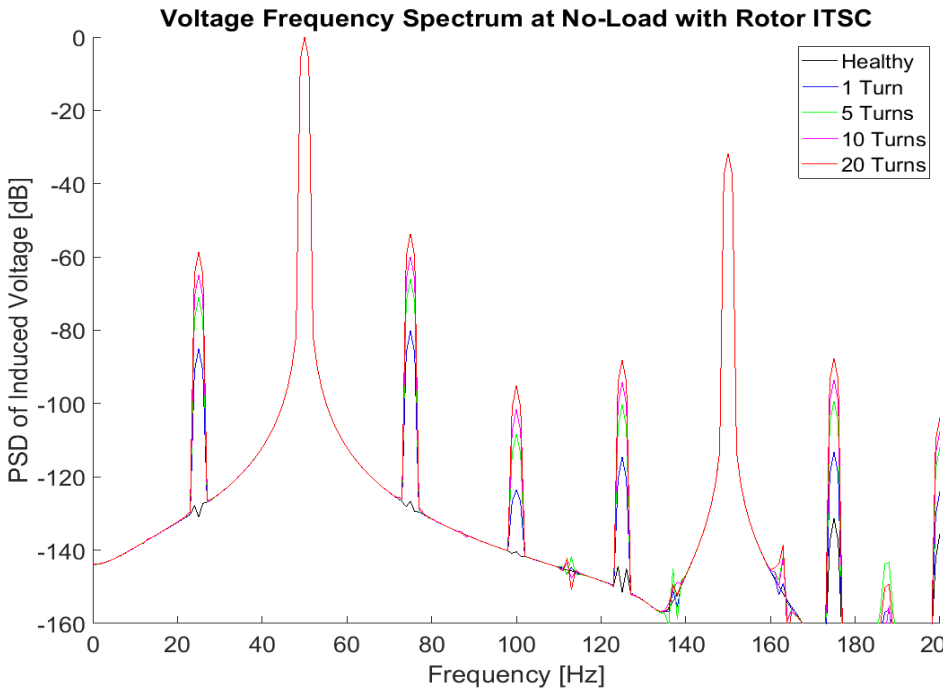

Figure 5.3: The PSD of the phase voltage of Machine 1 with different degrees of rotor ITSC fault at no-load operation.

Table 5.1: Amplitudes of the prominent sideband harmonics of stator phase voltage at no-load operation for different degrees of rotor ITSC fault severity.

Number of shorted turns [#]	25 [Hz] in [dB]	75 [Hz] in [dB]	125 [Hz] in [dB]	175 [Hz] in [dB]
0	-131	-126.7	-151.4	-131.3
1	-85.13	-80.18	-114.5	-113.2
5	-71.02	-66.07	-100.3	-99.26
10	-64.88	-59.92	-94.19	-93.48
20	-58.61	-53.65	-88.16	-87.63

Table 5.2: Amplitude difference between the 25[Hz] and the 75[Hz] harmonic sideband for stator phase voltage no-load operation for different degrees of rotor ITSC fault severity.

Number of shorted turns [#]	$A_{75[Hz]} - A_{25[Hz]}$ [dB]
1	4.95
5	4.95
10	4.96
20	4.96

5.1.2 Dynamic Eccentricity Simulation Results

Figure 5.4 shows the frequency spectrum of the FFT analysed phase voltage Machine 1 with degree of dynamic eccentricity, all simulated in the no-load operating condition. The figure shows clear fault induced sideband harmonics on both sides of the regular harmonics. The most prominent sideband harmonics are found at 25[Hz], 75[Hz] and 175[Hz] frequencies. The amplitude of the aforementioned frequencies, and the 125[Hz] is given in table 5.3 and the amplitude difference between the 25[Hz] and the 75[Hz] sideband harmonics are given in table 5.4.

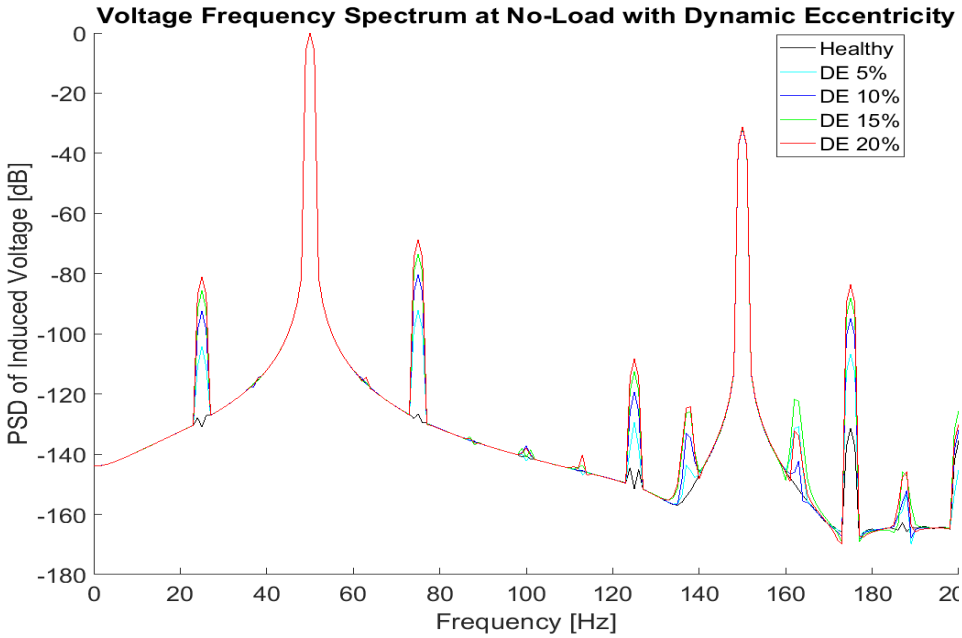

Figure 5.4: The PSD of the phase voltage of Machine 1 with different degrees of dynamic eccentricity at no-load operation. DE gives the degree of dynamic eccentricity.

Table 5.3: Amplitudes of the prominent sideband harmonics of stator phase voltage at no-load operation for different degrees of dynamic eccentricity.

Degrees of dynamic eccentricity	25 [Hz] in [dB]	75 [Hz] in [dB]	125 [Hz] in [dB]	175 [Hz] in [dB]
0	-131	-126.7	-151.4	-131.3
5%	-104.1	-92.24	-129.4	-106.8
10%	-92.45	-80.3	-119.2	-94.81
15%	-85.66	-73.41	-112.6	-88.18
20%	-81.04	-68.66	-108.3	-83.7

Table 5.4: Amplitude difference between the 25[Hz] and the 75[Hz] harmonic sideband for stator phase voltage no-load operation for different degrees of dynamic eccentricity.

Degree of dynamic eccentricity	$A_{75[Hz]} - A_{25[Hz]}$ [dB]
5%	11.86
10%	12.15
15%	12.25
20%	12.38

5.1.3 Static Eccentricity Simulation Results

Figure 5.5 shows the frequency spectrum of the FFT analysed phase voltage of Machine 1 with varying degree of static eccentricity, all simulated in the no-load operating condition. The figure shows no prominent sidebands. Only the high critical level of 40% static eccentricity produces a sideband which is detectable and the thesis assumes this is unacceptably high.

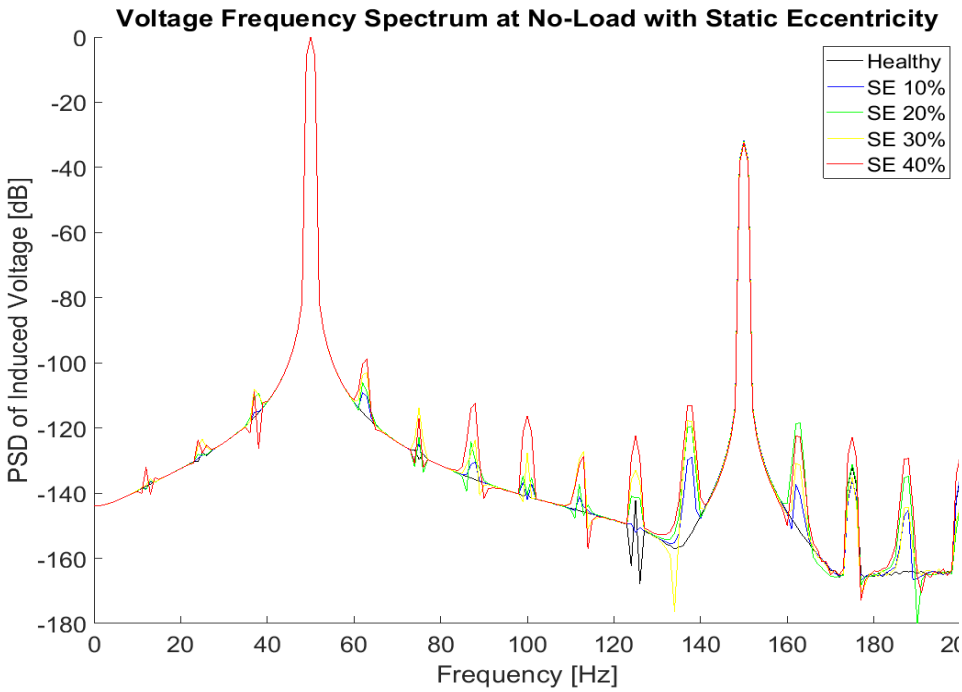

Figure 5.5: The PSD of the phase voltage of Machine 1 with different degrees of static eccentricity at no-load operation. SE gives the degree of static eccentricity.

5.1.4 Mixed Eccentricity Simulation Results

Figure 5.6 shows the frequency spectrum of the FFT analysed phase voltage of Machine 1 with different degrees of mixed eccentricity, all simulated in the no-load operating condition. The figure shows clear fault induced sideband harmonics on both sides of the regular harmonics. The most prominent sideband harmonics are found at 25[Hz], 37.5[Hz], 62.5[Hz] and 75[Hz]. The amplitude of the aforementioned frequencies, the 125[Hz] and the 175[Hz] harmonic sidebands is given in table 5.5, and the amplitude difference between the 25[Hz] and the 75[Hz] sideband

harmonics are given in table 5.7. The change in amplitude of the prominent sidebands caused by change in either the degree of dynamic or static eccentricity is shown in table 5.6.

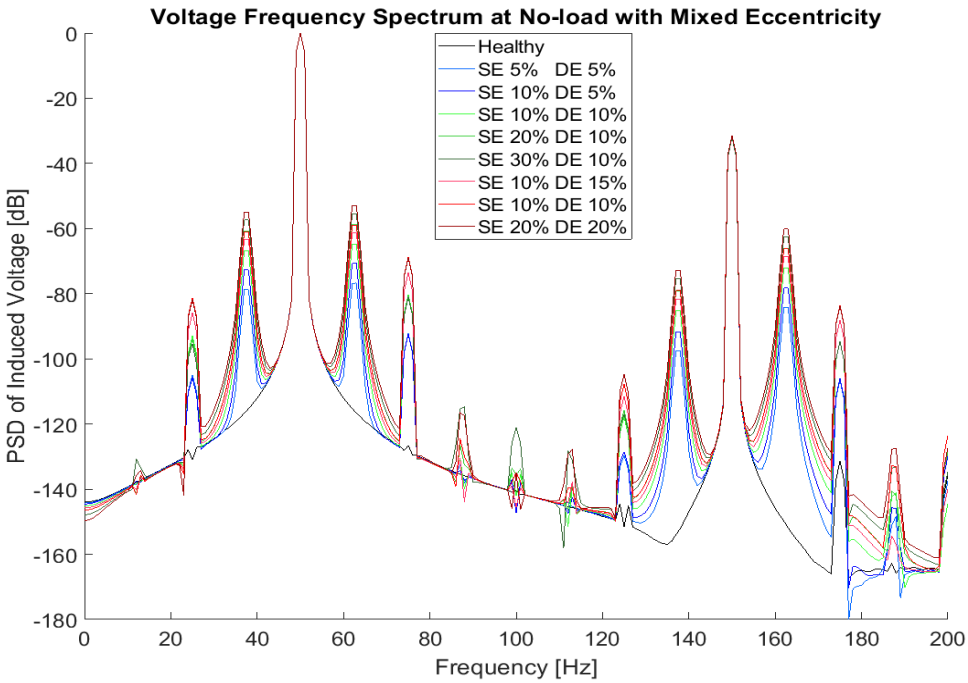

Figure 5.6: The PSD of the phase voltage of Machine 1 with different degrees of mixed eccentricity at no-load operation, with different degrees of static and dynamic eccentricity. DE and SE gives the degree of dynamic and static eccentricity respectively.

Table 5.5: Amplitudes of the prominent sideband harmonics of stator phase voltage at no-load operation for different degrees of mixed eccentricity.

δ_s	δ_d	25 [Hz] in [dB]	37.5 [Hz] in [dB]	62.5 [Hz] in [dB]	75 [Hz] in [dB]	125 [Hz] in [dB]	175 [Hz] in [dB]
0 %	0 %	-131	-115.3	-115.2	-126.7	-151.4	-131.3
5%	5%	-105	-78.75	-76.76	-92.24	-129.7	-106.6
10%	5%	-105.8	-72.7	-70.7	-92.46	-128.5	-106.1
10 %	10 %	-92.9	-66.83	-64.82	-80.41	-117.9	-94.72
10 %	15 %	-85.9	-63.34	-61.37	-73.47	-111.5	-88.13
10 %	20 %	-81.24	-60.92	-58.95	-68.73	-107.8	-83.63
20 %	20 %	-81.77	-54.96	-53	-68.93	-104.8	-83.84
20 %	10 %	-93.93	-60.81	-58.81	-80.59	-115.9	-94.7
30 %	10 %	-95.33	-57.38	-55.45	-80.99	-117	-94.63

Table 5.6: Change in amplitude of the prominent harmonics sidebands, caused by changing the degree of static or dynamic eccentricity for the stator phase voltage at no-load operation.

Change in δ_s	Change in δ_d	$\Delta A_{25[Hz]}$ [dB]	$\Delta A_{37.5[Hz]}$ [dB]	$\Delta A_{62.5[Hz]}$ [dB]	$\Delta A_{75[Hz]}$ [dB]
Change in amplitude caused by change in the degree of dynamic eccentricity					
10% to 10%	5% to 10%	12.9	5.87	5.88	12.05
10% to 10%	10% to 15%	7	3.49	3.45	6.94
10% to 10%	15% to 20%	4.66	2.42	2.42	4.74
10% to 10%	5% to 20%	24.56	11.78	11.75	23.73
Change in amplitude caused by change in the degree of static eccentricity					
10% to 20%	10% to 10%	-1.03	6.02	6.01	-0.18
20% to 30%	10% to 10%	-1.4	3.43	3.36	-0.4
10% to 30%	10% to 10%	-2.43	9.45	9.37	-0.58

Table 5.7: Amplitude difference between the 25[Hz] and the 75[Hz] harmonic sideband for stator phase voltage at no-load operation for different degrees of mixed eccentricity.

Degree of static eccentricity	Degree of dynamic eccentricity	$A_{75[Hz]} - A_{25[Hz]}$ [dB]
5%	5%	12.76
10%	5%	13.34
10%	10%	12.49
10%	15%	12.43
10%	20%	12.51
20%	20%	12.84
20%	10%	13.34
30%	10%	14.34

5.1.5 Rotor ITSC with Static Eccentricity Simulation Results

Figure 5.7 shows the frequency spectrum of the FFT analysed phase voltage of Machine 1 with different degrees of rotor ITSC with static eccentricity, all simulated in the no-load operating condition. The figure shows clear fault induced sideband harmonics on both sides of the regular machine harmonics. The most prominent sideband harmonics are found at 25[Hz], 37.5[Hz], 62.5[Hz] and 75[Hz]. The amplitude of the aforementioned frequencies, the 125 [Hz] and the 175[Hz] harmonic sidebands is given in table 5.8 and the amplitude difference between the 25[Hz] and the 75[Hz] sideband harmonics are given in table 5.10 The change in amplitude of the prominent sidebands caused by change in either the degree of static eccentricity or the number of shorted turns is shown in table 5.9.

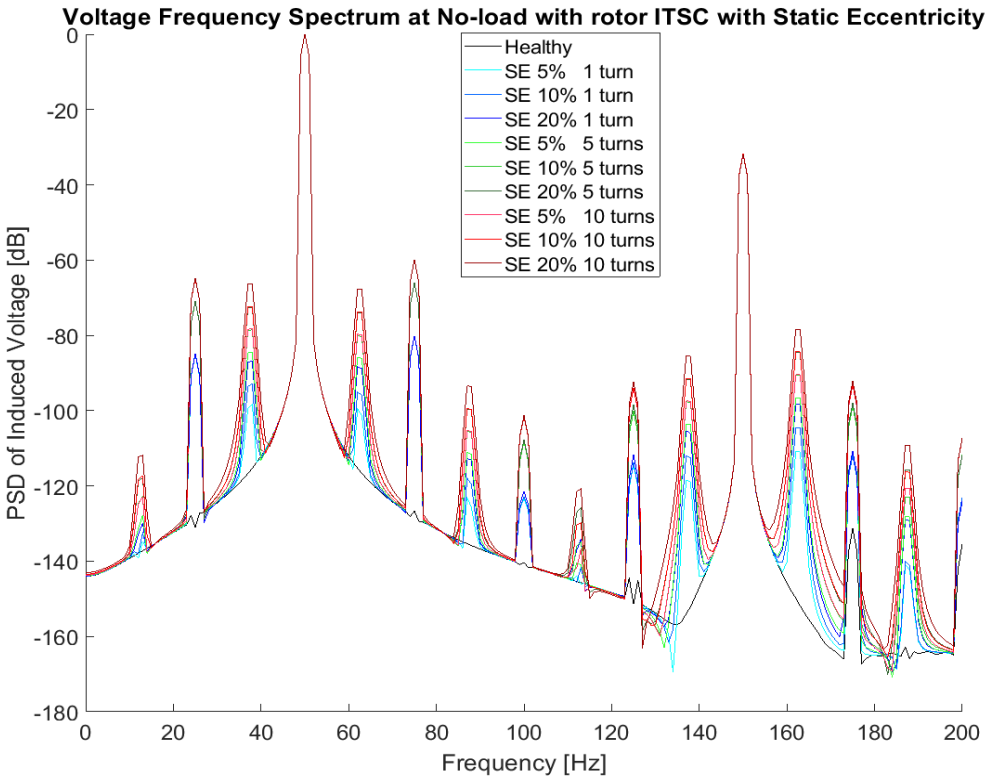

Figure 5.7: The PSD of the phase voltage of Machine 1 with different degrees of rotor ITSC with static eccentricity at no-load operation. Where SE gives the degree of static eccentricity. SE gives the degree of static eccentricity.

Table 5.8: Amplitudes of the prominent sideband harmonics of stator phase voltage at no-load operation for different severities of rotor ITSC with static eccentricity.

δ_S	Number of shorted turns [#]	25 [Hz] in [dB]	37.5 [Hz] in [dB]	62.5 [Hz] in [dB]	75 [Hz] in [dB]	125 [Hz] in [dB]	175 [Hz] in [dB]
0	0	-131	-116.7	-116.7	-126.7	-151.4	-131.3
5%	1	-85.09	-98.17	-99.47	-80.21	-114.2	-111.7
10%	1	-85.01	-92.92	-95.09	-80.17	-113.8	-112
20%	1	-84.74	-86.76	-88.31	-80.1	-111.7	-110.8
5%	5	-71.01	-84.42	-85.82	-66.08	-100.1	-98.86
10%	5	-70.99	-78.54	-80.13	-66.08	-99.92	-98.61
20%	5	-70.92	-72.55	-74.04	-66.02	-98.43	-97.99
5%	10	-64.87	-78.25	-79.68	-59.92	-94.08	-93.26
10%	10	-64.85	-72.31	-73.78	-59.9	-93.87	-92.91
20%	10	-64.79	-66.32	-67.74	-59.86	-92.44	-92.2

Table 5.9: Change in amplitude of the prominent harmonics sidebands, caused by changing the degree of static eccentricity or the number of shorted turns for stator phase voltage at no-load operation.

Change in δ_s	Change in number of shorted turns [#]	$\Delta A_{25[Hz]}$ [dB]	$\Delta A_{37.5[Hz]}$ [dB]	$\Delta A_{62.5[Hz]}$ [dB]	$\Delta A_{75[Hz]}$ [dB]
Change in amplitude caused by change in the number of shorted turns					
5% to 5%	1 to 5	14.08	13.75	13.65	14.13
5% to 5%	5 to 10	6.14	6.17	6.14	6.16
5% to 5%	1 to 10	20.22	19.92	19.79	20.29
10% to 10%	1 to 5	14.02	14.38	14.96	14.09
10% to 10%	5 to 10	6.16	12.11	12.04	6.18
10% to 10%	1 to 10	20.16	20.61	21.31	20.27
20% to 20%	1 to 5	13.82	14.21	14.27	14.08
20% to 20%	5 to 10	6.13	6.23	6.3	6.16
20% to 20%	1 to 10	19.95	20.44	20.57	20.24
Change in amplitude caused by change in the degree of static eccentricity					
5% to 10%	1 to 1	0.08	5.25	4.38	0.04
10% to 20%	1 to 1	0.27	6.16	6.78	0.07
5% to 20%	1 to 1	0.35	11.41	11.16	0.11
5% to 10%	5 to 5	0.02	5.88	5.69	0
10% to 20%	5 to 5	0.07	5.99	6.09	0.06
5% to 20%	5 to 5	0.09	11.87	11.78	0.06
5% to 10%	10 to 10	0.02	5.94	5.9	0.02
10% to 20%	10 to 10	0.06	5.99	6.04	0.04
5% to 20%	10 to 10	0.08	11.93	11.94	0.06

Table 5.10: Amplitude difference between the 25[Hz] and the 75[Hz] harmonic sideband for stator phase voltage at no-load operation for different severities of rotor ITSC with static eccentricity.

δ_S	Number of shorted turns [#]	$A_{75[Hz]} - A_{25[Hz]}$ [dB]
5%	1	4.88
10%	1	4.84
20%	1	4.64
5%	5	4.93
10%	5	4.91
20%	5	4.9
5%	10	4.95
10%	10	4.95
20%	10	4.93

5.2 Machine 1 Full-load Simulation Result

5.2.1 Rotor ITSC Simulation Results

Figure 5.8 shows the frequency spectrum of the FFT analysed phase voltage of Machine 1 with varying degree of rotor ITSC, all simulated in the full-load operating condition. The figure shows clear fault induced sideband harmonics on both sides of the regular harmonics (the 50[Hz] and the 150[Hz]). The most prominent sideband harmonics are found at 25[Hz], 75[Hz] and 125[Hz] frequencies. The amplitude of the aforementioned frequencies and 175[Hz] is given in table 5.11 and the amplitude difference between the 25[Hz] and the 75[Hz] sideband harmonics are given in table 5.12. Figure 5.9 shows the frequency spectrum of the FFT analysed phase current of Machine 1 with varying degree of rotor ITSC, all simulated in the full-load operating condition. The most prominent sideband harmonics are the 25[Hz], 125[Hz] and 175[Hz], and their amplitudes are shown in table 5.13.

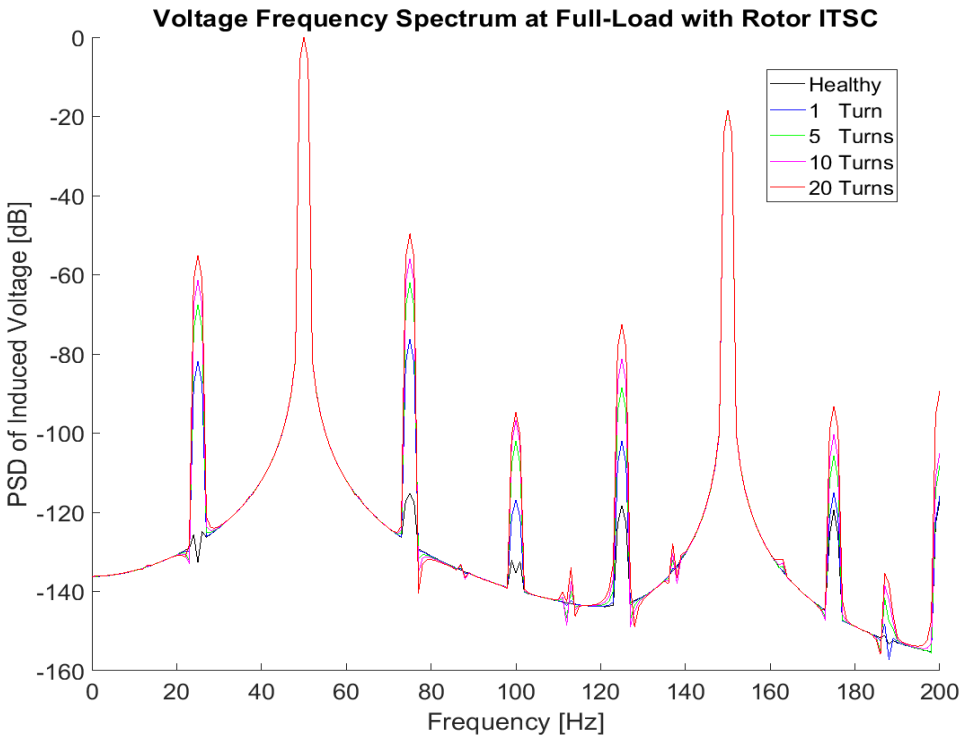

Figure 5.8: The PSD of the phase voltage of Machine 1 with different degrees of rotor ITSC faults at full-load operation.

Table 5.11: Amplitudes of the prominent sideband harmonics of stator phase voltage at full-load operation for different severities of rotor ITSC faults.

Number of shorted turns [#]	25 [Hz] in [dB]	75 [Hz] in [dB]	125 [Hz] in [dB]	175 [Hz] in [dB]
0	-132.6	-115.2	-118.3	-119.4
1	-81.77	-76.22	-102	-114.9
5	-67.63	-62.05	-88.43	-105.7
10	-61.44	-55.89	-81.15	-100.4
20	-55.12	-49.64	-72.45	-93.16

Table 5.12: Amplitude difference between the 25[Hz] and the 75[Hz] harmonic sideband for stator phase voltage full-load operation for different severities of rotor ITSC with static eccentricity.

Number of shorted turns [#]	$A_{75[Hz]} - A_{25[Hz]}$ [dB]
1	5.55
5	5.58
10	5.55
20	5.48

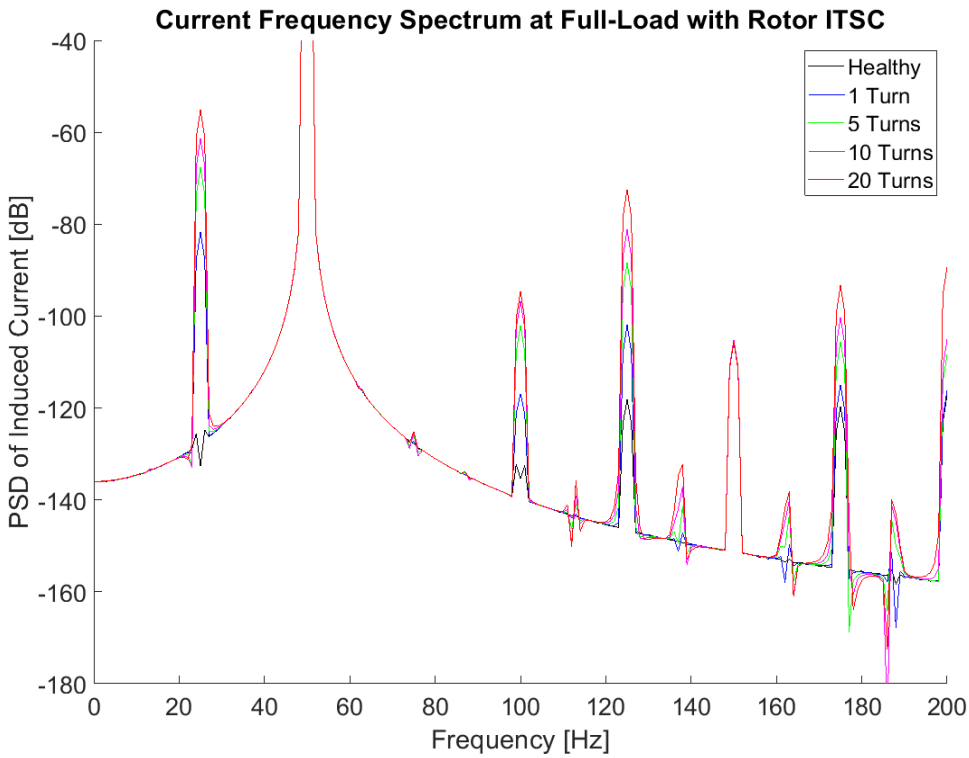

Figure 5.9: The PSD of the phase current of Machine 1 with different degrees of rotor ITSC at full-load operation.

Table 5.13: Amplitudes of the prominent sideband harmonics of stator phase voltage at full-load operation for different severities of rotor ITSC faults.

Number of shorted turns [#]	25 [Hz] in [dB]	125 [Hz] in [dB]	175 [Hz] in [dB]
0	-132.6	-118.1	-119.6
1	-81.76	-101.9	-114.9
5	-67.63	-88.43	-105.5
10	-61.43	-81.15	-100.3
20	-55.12	-72.46	-93.34

5.2.2 Dynamic Eccentricity Simulation Results

Figure 5.10 shows the frequency spectrum of the FFT analysed phase voltage of Machine 1 with varying degree of dynamic eccentricity, all simulated in the full-load operating condition. The figure shows clear fault induced sideband harmonics on both sides of the regular harmonics. The most prominent sideband harmonics are found at 25[Hz], 75[Hz] and 175 [Hz] frequencies. The amplitude of the aforementioned frequencies and 125[Hz] is given in table 5.14 and the amplitude difference between the 25[Hz] and the 75[Hz] sideband harmonics are given in table 5.15. The figure 5.11 shows the frequency spectrum of the FFT analysed phase current of Machine with varying degree of dynamic eccentricity, all simulated in the full-load operating condition. The most prominent sideband harmonics are the 25[Hz], 125[Hz] and 175[Hz], and their amplitudes are shown in table 5.16.

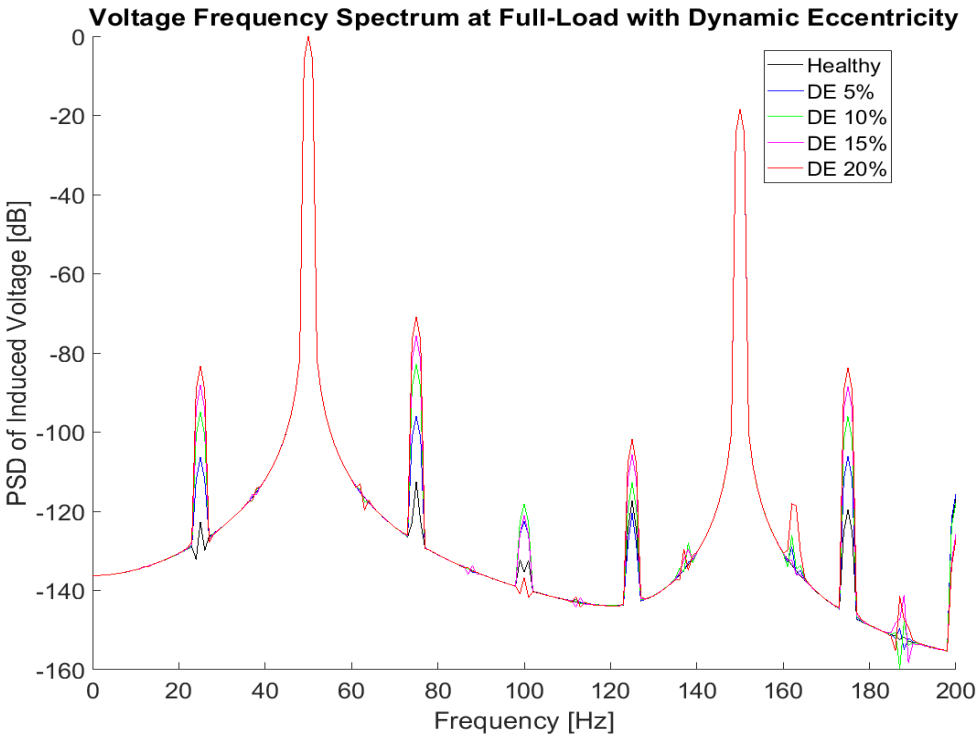

Figure 5.10: The PSD of the phase voltage of Machine 1 with different degrees of dynamic eccentricity at full-load operation. DE gives the degree of dynamic eccentricity.

Table 5.14: Amplitudes of the prominent sideband harmonics of stator phase voltage at full-load operation for different degrees of dynamic eccentricity.

Degrees of dynamic eccentricity	25 [Hz] in [dB]	75 [Hz] in [dB]	125 [Hz] in [dB]	175 [Hz] in [dB]
0	-122.7	-112.6	-117.4	-119.7
5%	-106.4	-95.96	-120.5	-106.2
10%	-94.9	-82.96	-112.7	-96.06
15%	-88.15	-75.74	-105.7	-88.41
20%	-83.32	-70.81	-101.8	-83.69

Table 5.15 Amplitude difference between the 25[Hz] and the 75[Hz] harmonic sideband for stator phase voltage full-load operation for different degrees of dynamic eccentricity.

Degree of dynamic eccentricity	$A_{75[Hz]} - A_{25[Hz]}$ [dB]
5%	10.44
10%	11.94
15%	12.41
20%	12.51

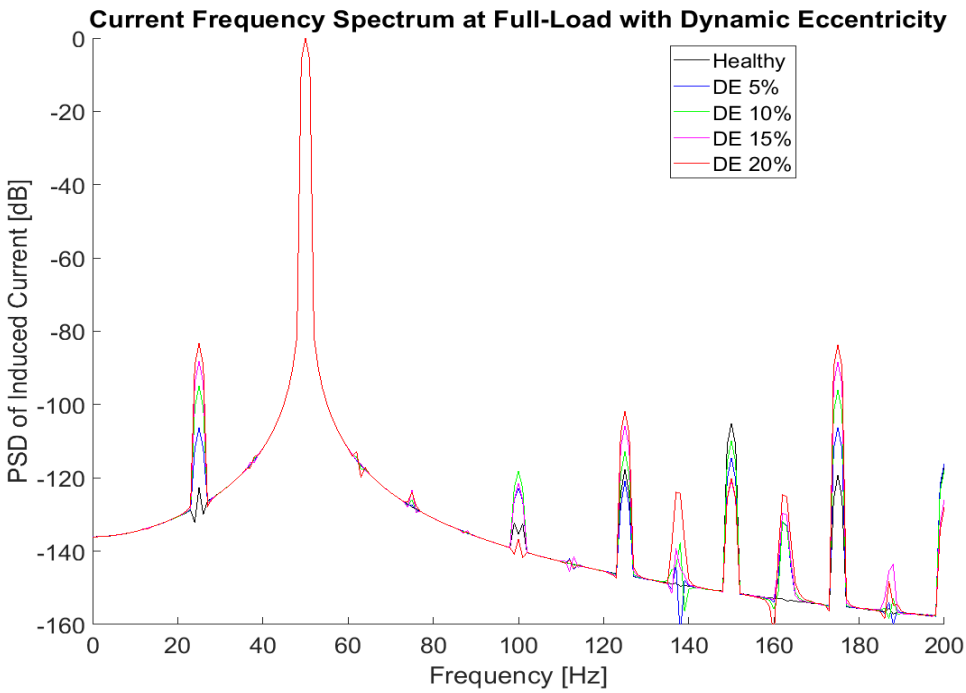

Figure 5.11: The PSD of the phase current of Machine 1 with different degrees of dynamic eccentricity at full-load operation. DE gives the degree of dynamic eccentricity.

Table 5.16: Amplitudes of the prominent sideband harmonics of stator phase current at full-load operation for different degrees of dynamic eccentricity.

Degrees of dynamic eccentricity	25 [Hz] in [dB]	125 [Hz] in [dB]	175 [Hz] in [dB]
0	-122.7	-117.7	-119.4
5%	-106.4	-120.8	-106.2
10%	-94.89	-112.7	-96.05
15%	-88.15	-105.8	-88.41
20%	-83.31	-101.8	-83.72

5.2.3 Static Eccentricity Simulation Results

Figure 5.12 and 5.13 shows the results of the FFT analysis for the stator phase voltage and stator phase current respectively. Both simulated on the Machine 1 model at full-load operating condition. The figure shows no prominent sidebands. Only the high critical level of 40% static eccentricity produces a sideband which is detectable and the thesis assumes this is unacceptably high.

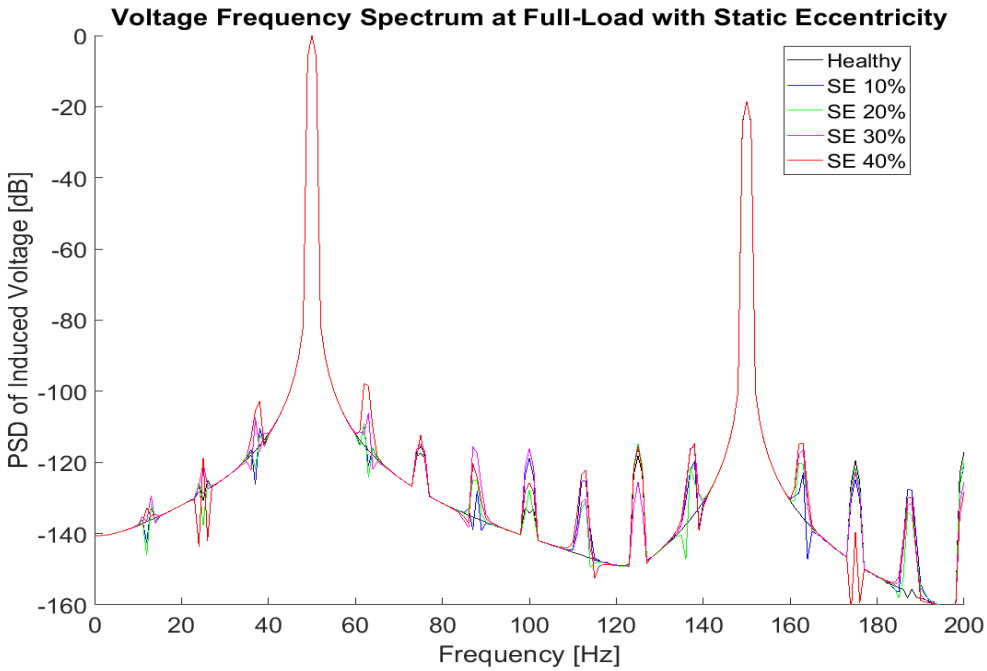

Figure 5.12: The PSD of the phase voltage of Machine 1 with different degrees of static eccentricity at full-load operation. SE gives the degree of static eccentricity.

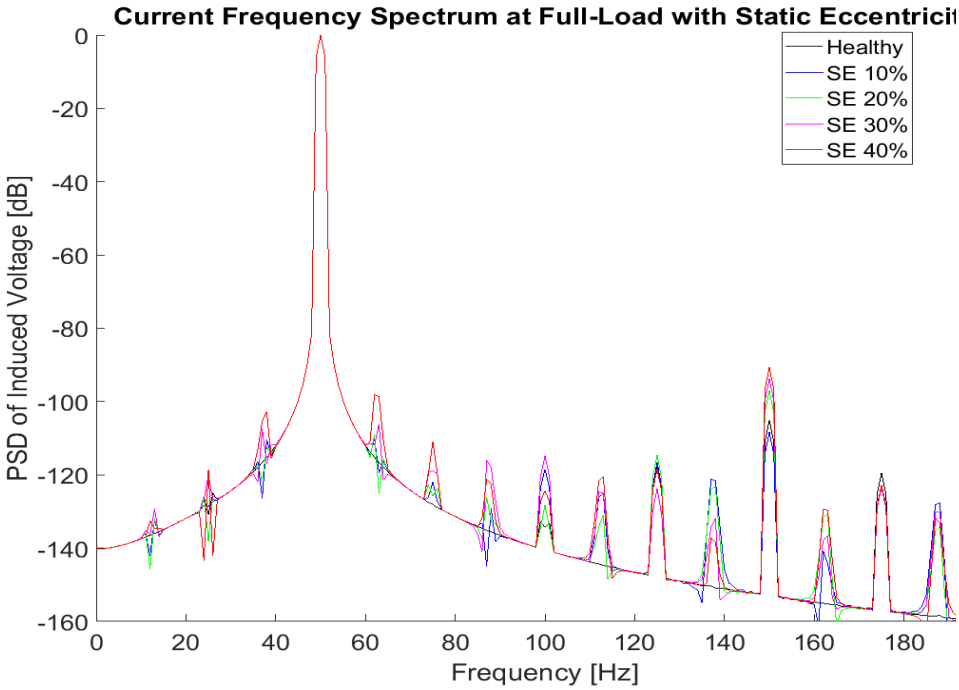

Figure 5.13: The PSD of the phase current of Machine 1 with different degrees of static eccentricity at full-load operation. SE gives the degree of static eccentricity.

5.2.4 Mixed Eccentricity Simulation Results

Figure 5.14 shows the frequency spectrum of the FFT analysed phase voltage of Machine 1 with varying degree of mixed eccentricity, all simulated in the full-load operating condition. The figure shows clear fault induced sideband harmonics on both sides of the regular harmonics. The most prominent sideband harmonics are found at 25[Hz], 37.5[Hz], 62.5[Hz] and 75[Hz] frequencies. The amplitude of the aforementioned frequencies and the 125[Hz] and the 175[Hz] is given in table 5.17 The change in amplitude of caused by changing either the degree of static or

dynamic eccentricity are shown in table 5.18. The amplitude difference between the 25[Hz] and the 75[Hz] sideband harmonics are given in table 5.19. The figure 5.15 shows the frequency spectrum of the FFT analysed phase current of Machine 1 with varying degree of mixed eccentricity, all simulated in the full-load operating condition. The most prominent sideband harmonics are the 25[Hz], 37.5[Hz] and 62.5[Hz] and their amplitudes as well as the amplitude of the 125[Hz] and 175[Hz] are shown in table 5.20

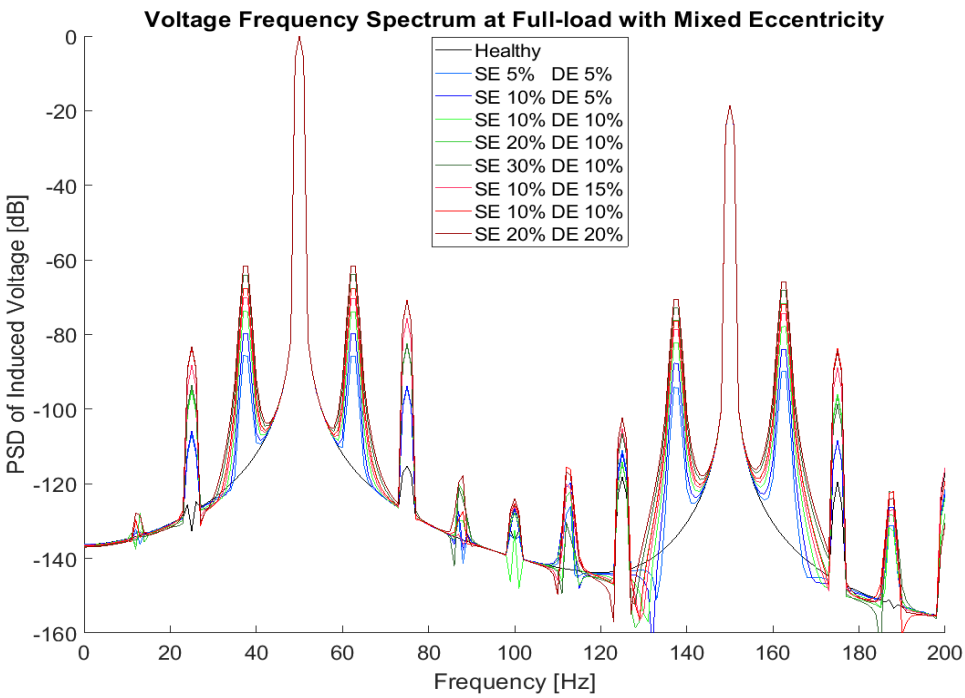

Figure 5.14: The PSD of the phase voltage of Machine 1 with mixed eccentricity at full-load operation, with different degrees of static and dynamic eccentricity. DE and SE gives the degree of dynamic and static eccentricity respectively.

Table 5.17: Amplitudes of the prominent sideband harmonics of stator phase voltage at full-load operation for different degrees of mixed eccentricity.

δ_s	δ_d	25 [Hz] in [dB]	37.5 [Hz] in [dB]	62.5 [Hz] in [dB]	75 [Hz] in [dB]	125 [Hz] in [dB]	175 [Hz] in [dB]
0%	0 %	-132.6	-115.1	-115.1	-115.2	-118.3	-119.4
5%	5%	-106.7	-85.88	-85.83	-94.03	-110.9	-108.4
10%	5%	-105.8	-79.85	-79.82	-93.72	-111.9	-108.5
10%	10%	-95.06	-73.78	-74	-82.69	-114.2	-95.89
10%	15%	-88.21	-70.2	-70.33	-75.73	-105.1	-88.94
10%	20%	-83.46	-62.7	-67.79	-70.81	-102.3	-83.75
20%	20%	-83.16	-61.67	-61.7	-70.87	-102.3	-84.46
20%	10%	-94.24	-67.6	-61.61	-82.36	-114.9	-96.42
30 %	10%	-93.56	-64.01	-63.94	-82.58	-106.5	-98.72

Table 5.18: Change in amplitude of the prominent harmonics sidebands, caused by changing the degree of static or degree of dynamic eccentricity for stator phase voltage at full-load operation.

Change in δ_s	Change δ_d	$\Delta A_{25[Hz]}$ [dB]	$\Delta A_{37.5[Hz]}$ [dB]	$\Delta A_{62.5[Hz]}$ [dB]	$\Delta A_{75[Hz]}$ [dB]
Change in amplitude caused by change in the degree of dynamic eccentricity					
10% to 10%	5% to 10%	10.74	6.07	5.82	11.03
10% to 10%	10% to 15%	6.85	3.58	3.67	6.96
10% to 10%	15% to 20%	4.75	7.5	2.54	4.92
10% to 10%	5% to 20%	22.34	17.15	12.03	22.91
Change in amplitude caused by change in the degree of static eccentricity					
10% to 20%	10% to 10%	0.82	6.18	12.39	0.33
20% to 30%	10% to 10%	0.68	3.59	-2.33	-0.22
10% to 30%	10% to 10%	1.5	9.77	10.06	0.11

Table 5.19: Amplitudes of the prominent sideband harmonics of stator phase voltage at full-load operation for different degrees of mixed eccentricity.

δ_s	δ_d	$A_{75[Hz]} - A_{25[Hz]}$ [dB]
5%	5%	12.67
10%	5%	12.08
10%	10%	12.37
10%	15%	12.48
10%	20%	12.65
20%	20%	12.29
20%	10%	11.88
30%	10%	10.98

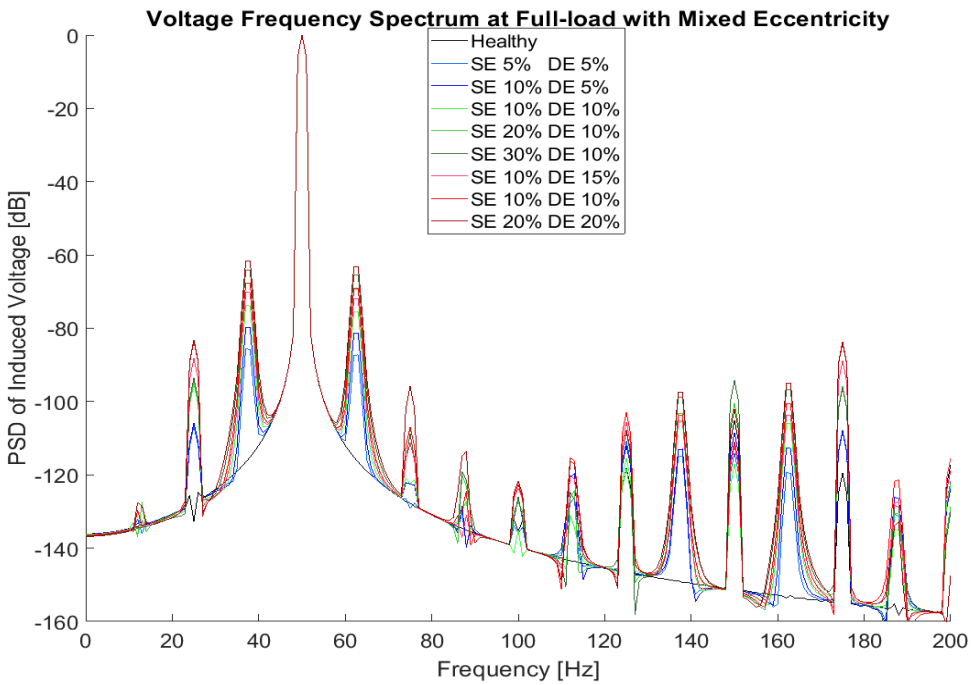

Figure 5.15: The PSD of the phase current of Machine 1 with mixed eccentricity at full-load operation, with different degrees of static and dynamic eccentricity. DE and SE gives the degree of dynamic and static eccentricity respectively.

Table 5.20: Amplitudes of the prominent sideband harmonics of stator phase current at full-load operation for different degrees of mixed eccentricity.

δ_s	δ_d	25 [Hz] in [dB]	37.5 [Hz] in [dB]	62.5 [Hz] in [dB]	75 [Hz] in [dB]	125 [Hz] in [dB]	175 [Hz] in [dB]
0%	0 %	-132.6	-115.1	-115.1	-127.7	-118.1	-119.6
5%	5%	-106.7	-85.56	-87.26	-129.1	-110.9	-108.2
10%	5%	-105.8	-79.68	-81.29	-122.5	-112.2	-107.8
10%	10%	-95.04	-73.78	-75.32	-121.4	-115.4	-95.76
10%	15%	-88.2	-70.19	-71.84	-111.3	-105.5	-88.83
10%	20%	-83.43	-67.7	-69.29	-106.9	-102.9	-83.65
20%	20%	-83.15	-61.67	-63.19	-95.85	-107.8	-84.94
20%	10%	-94.23	-67.6	-69.1	-107.2	-118.3	-95.87
30 %	10%	-93.58	-64.05	-65.41	-108.8	-108	-96.18

5.2.5 Rotor ITSC with Static Eccentricity Simulation Results

Figure 5.16 shows the frequency spectrum of the FFT analysed phase voltage of Machine 1 with varying degree rotor ITSC with static eccentricity fault severity, all simulated in the full-load operating condition. The figure shows clear fault induced sideband harmonics on both sides of the regular machine harmonics. The most prominent sideband harmonics are found at 25[Hz], 37.5[Hz], 62.5[Hz] and 75[Hz] frequencies. The amplitude of the aforementioned frequencies and the 125[Hz] and the 175[Hz] is given in table 5.21 The change in amplitude is caused by changing either the degree of static or dynamic eccentricity are shown in table 5.22. The amplitude difference between the 25[Hz] and the 75[Hz] sideband harmonics are given in table 5.23. Figure 5.17 shows the frequency spectrum of the FFT analysed phase current of Machine 1 with varying degree rotor ITSC with static eccentricity fault severity, all

simulated in the full-load operating condition. The most prominent sideband harmonics are the 25[Hz], 37.5[Hz] and 62.5[Hz] and their amplitudes as well as the amplitude of the 125[Hz] and 175[Hz] are shown in table 5.24

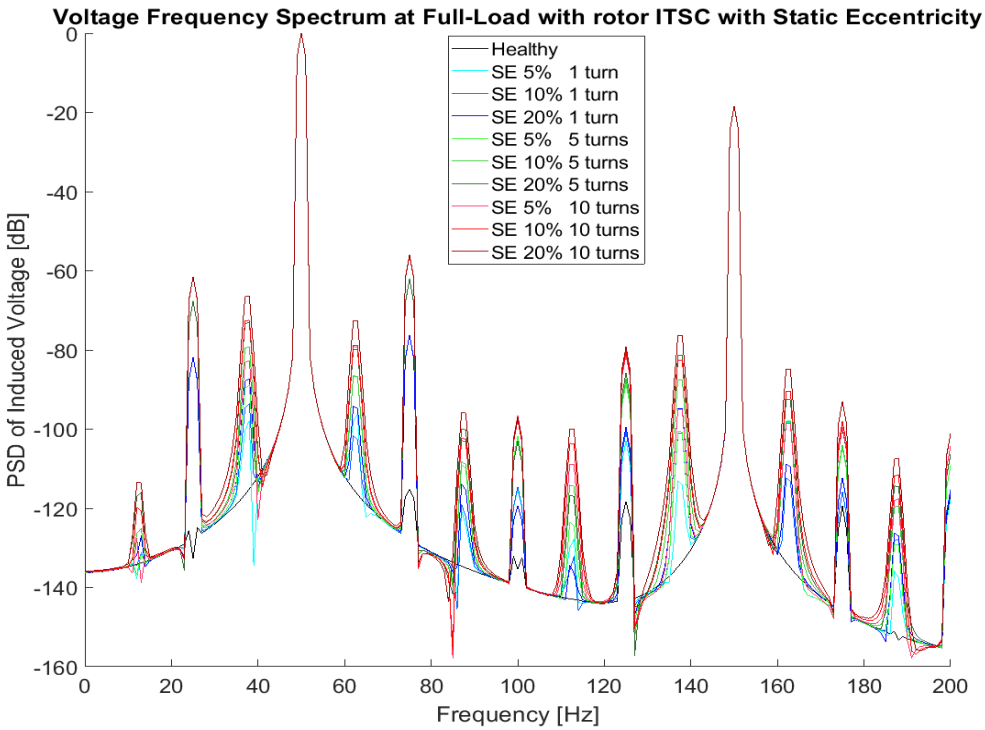

Figure 5.16: The PSD of the phase voltage of Machine 1 with different degrees of rotor ITSC with static eccentricity at full-load operation. SE gives the degree of static eccentricity.

.

Table 5.21: Amplitudes of the prominent sideband harmonics of stator phase voltage at full-load operation for different severities of rotor ITSC with static eccentricity.

δ_s	Number shorted turns [#]	25 [Hz] in [dB]	37.5 [Hz] in [dB]	62.5 [Hz] in [dB]	75 [Hz] in [dB]	125 [Hz] in [dB]	175 [Hz] in [dB]
0%	0	-132.6	-116.5	-115.1	-115.2	-118.3	-119.4
5%	1	-81.8	-97.82	-96.2	-76.21	-102.9	-112.5
5%	5	-81.85	-93.52	-101.6	-76.22	-100.8	-115.9
5%	10	-81.93	-87.27	-94.25	-76.27	-99.53	-112.3
10%	1	-67.66	-88.87	-86.69	-62.06	-88.45	-104.7
10%	5	-67.67	-79.26	-86.52	-62.09	-87.36	-104
10%	10	-67.74	-73.12	-79.9	-62.18	-85.86	-99.86
20%	1	-61.46	-82.72	-79.16	-55.9	-81.16	-99.55
20%	5	-61.48	-72.51	-78.78	-55.94	-80.41	-98.13
20%	10	-61.57	-66.48	-72.59	-56.07	-79.25	-93.01

Table 5.22: Change in amplitude of the prominent harmonics sidebands, caused by changing the degree of static or number of shorted turns for stator phase voltage at full-load operation.

Change in δ_s	Change in number of shorted turns	$\Delta A_{25[Hz]}$ [dB]	$\Delta A_{37.5[Hz]}$ [dB]	$\Delta A_{62.5[Hz]}$ [dB]	$\Delta A_{75[Hz]}$ [dB]
Change in amplitude caused by change in number of shorted turns					
5% to 5%	1 to 5	14.14	8.95	9.51	14.15
5% to 5%	5 to 10	6.2	6.15	7.53	6.16
5% to 5%	1 to 10	20.34	15.1	17.04	20.31
10% to 10%	1 to 5	14.18	14.26	15.08	14.13
10% to 10%	5 to 10	6.18	16.36	7.91	6.12
10% to 10%	1 to 10	20.37	21.01	22.82	20.28
20% to 20%	1 to 5	14.19	14.15	14.35	14.09
20% to 20%	5 to 10	6.17	6.64	7.31	6.11
20% to 20%	1 to 10	20.36	20.79	21.66	20.2
Change in amplitude caused by change in the degree of dynamic eccentricity					
5% to 10%	1 to 1	-0.05	4.3	-5.4	-0.01
10% to 20%	1 to 1	-0.08	6.25	7.35	-0.05
5% to 10%	5 to 5	-0.13	10.55	1.95	-0.06
10% to 20%	5 to 5	-0.01	9.61	0.17	-0.03
5% to 10%	10 to 10	-0.07	6.14	6.62	-0.09
10% to 20%	10 to 10	-0.08	15.75	6.79	-0.12
5% to 20%	10 to 10	-0.02	10.21	0.38	-0.04

Table 5.23: Amplitude difference between the 25[Hz] and the 75[Hz] harmonic sideband for stator phase voltage full-load operation for different severities of rotor ITSC with static eccentricity.

δ_s	Number of shorted turns [#]	$A_{75[Hz]} - A_{25[Hz]}$ [dB]
5%	1	5.59
5%	5	5.63
5%	10	5.66
10%	1	5.6
10%	5	5.58
10%	10	5.56
20%	1	5.56
20%	5	5.54
20%	10	5.5

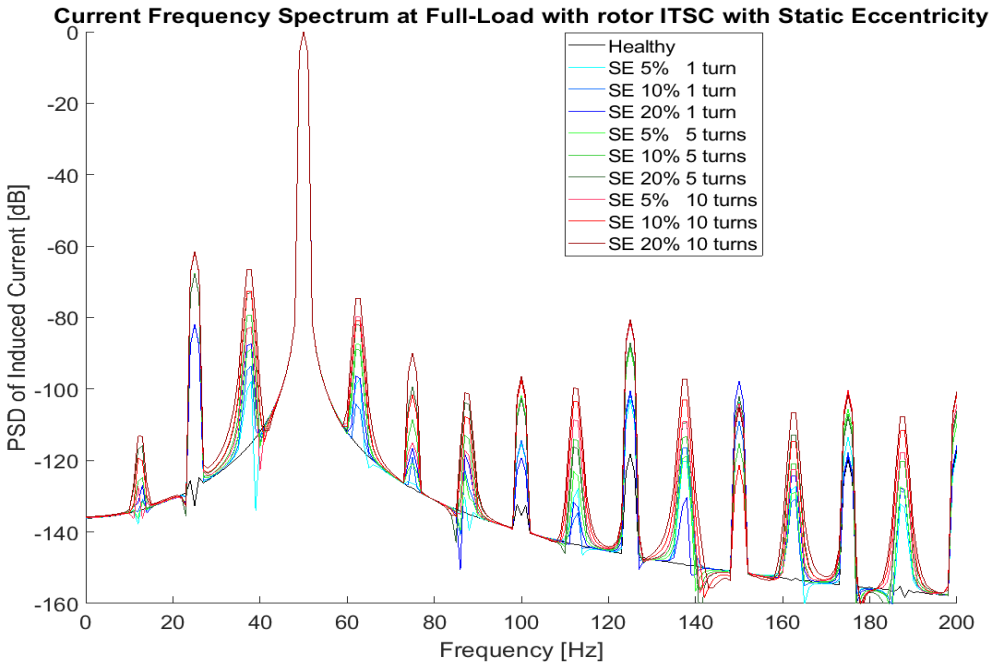

Figure 5.17: The PSD of the phase current of Machine 1 with different degrees of rotor ITSC with static eccentricity at full-load operation. SE gives the degree of static eccentricity.

Table 5.24: Amplitudes of the prominent sideband harmonics of stator phase current at full-load operation for different severities of rotor ITSC with static eccentricity.

δ_s	Number of shorted turns [#]	25 [Hz] in [dB]	37.5 [Hz] in [dB]	62.5 [Hz] in [dB]	75 [Hz] in [dB]	125 [Hz] in [dB]	175 [Hz] in [dB]
0%	0	-132.6	-116.5	-115.1	-127.7	-118.1	-119.6
5%	1	-81.79	-97.82	-96.89	-126.4	-103	-113.5
5%	5	-81.85	-93.52	-104.2	-119	-101.2	-117.8
5%	10	-81.92	-87.27	-96.4	-116.5	-100.4	-118.6
10%	1	-67.65	-88.86	-87.47	-120.8	-88.5	-105.5
10%	5	-67.67	-79.26	-88.4	-108.6	-87.79	-107
10%	10	-67.74	-73.12	-82.04	-99.36	-87.07	-107.7
20%	1	-61.46	-82.72	-79.81	-115.1	-81.23	-100.3
20%	5	-61.48	-72.51	-80.77	-101.6	-80.79	-100.8
20%	10	-61.57	-66.48	-74.56	-89.9	-80.5	-101.6

5.3 Machine 2 Simulation Results

This subchapter presents the results of fault simulations done on Machine 2. The results for the full-load phase voltage, full-load phase current and the no-load phase voltage have the same characteristics and only the full-load phase voltage results are presented, the rest are found in Appendix D.

The result of the simulations of Machine 2 show elimination of some of the sideband harmonics. The result of the dynamic eccentricity and rotor ITSC simulations show that the prominent sideband harmonics for the dynamic eccentricity and rotor ITSC fault are all eliminated, seen in figure 5.18 and 5.19, for dynamic eccentricity and rotor ITSC respectively. The same eliminations occur for the mixed eccentricity simulations, that being the elimination of prominent sidebands of 25 [Hz], 75[Hz], 125[Hz] and the 175[Hz]. As shown figure 5.21, the PSD still have prominent harmonic sidebands of 37.5[Hz], 62.5[Hz], 137.5[Hz] and 162.5[Hz]. The small sideband harmonics produced by the static eccentricity seems to be unaffected, as seen in figure 5.20.

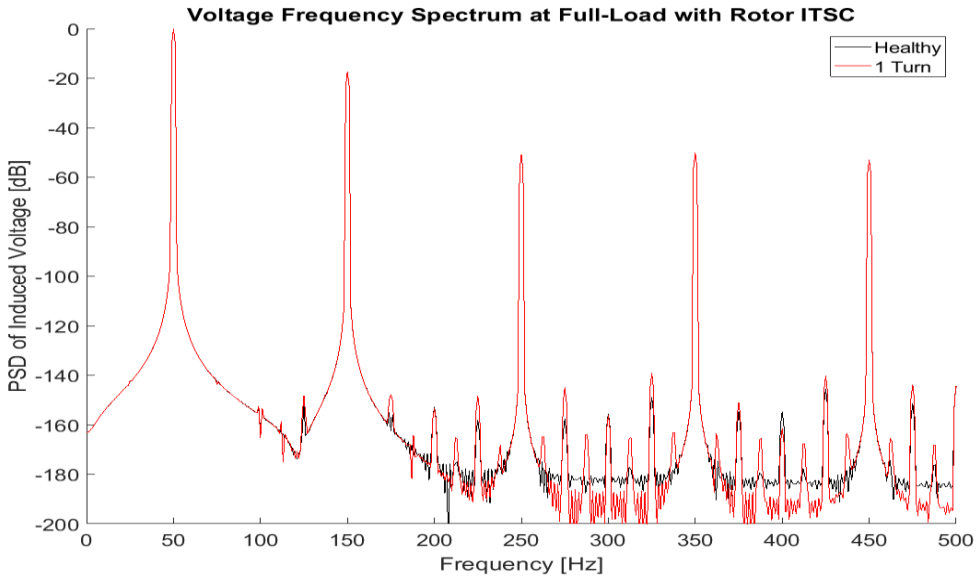

Figure 5.18: The PSD of the phase voltage of Machine 2 with rotor ITSC fault at full-load operation.

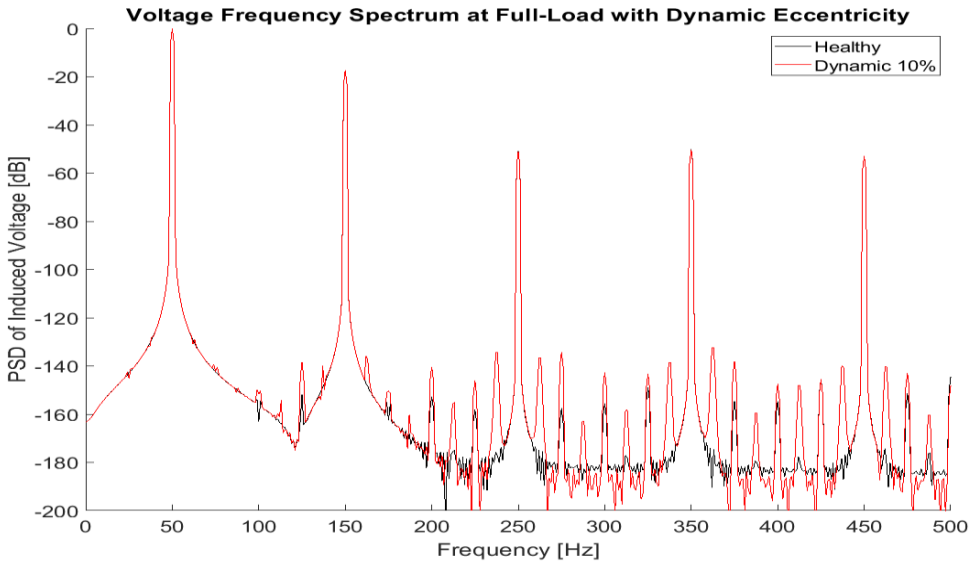

Figure 5.19: The PSD of the phase current of Machine 2 with dynamic eccentricity at full-load operation.

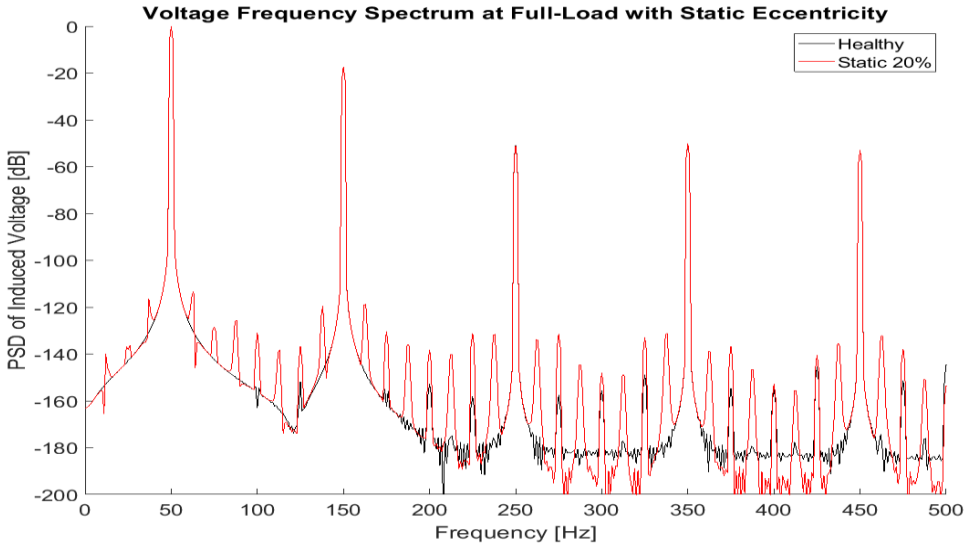

Figure 5.20: The PSD of the phase voltage of Machine 2 with static eccentricity at full-load operation.

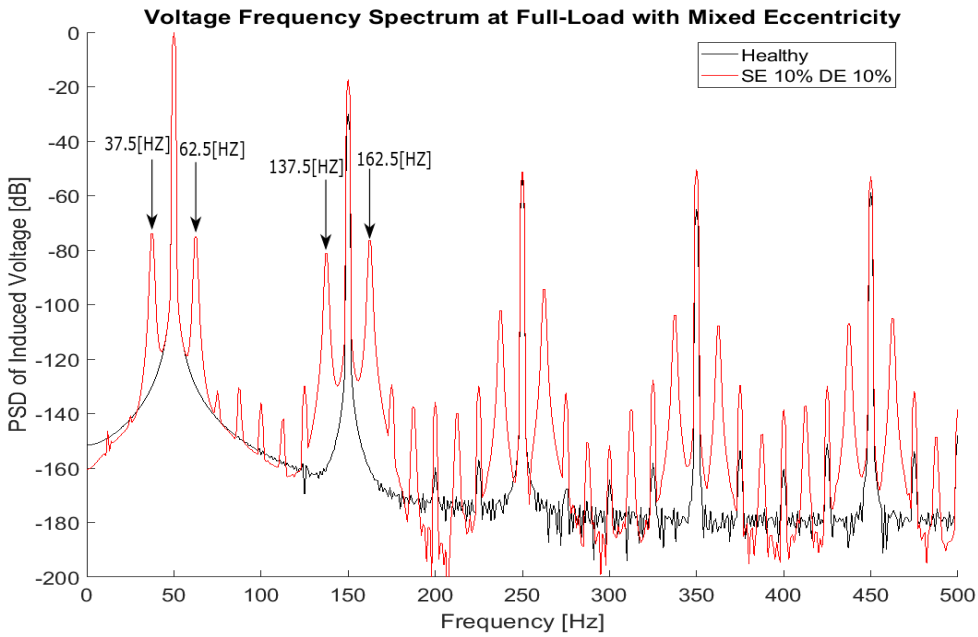

Figure 5.21: The PSD of the phase voltage of Machine 2 with mixed eccentricity at full-load operation. The mixed eccentricity have a static degree of 10% and a dynamic degree of 10%.

5.4 Machine 3 and Machine 4 Simulation Results

The simulations of Machine 3 gave result which was very similar to the results of Machine 1, with the same characteristics and sideband harmonics, therefore the result is not presented here but placed in Appendix E. The specific changes did not result in elimination or rise of any new harmonics and is not discussed further in this thesis. Similarly, the results of Machine 4 gave very similar the results of Machine 1, with the same characteristics and sideband harmonics, therefore the result is not presented here, but placed in Appendix F. The specific change did not result in any elimination or rise of new harmonics.

6 Discussion

The following chapter discuss the results presented in chapter 5. To argue for the detectability of fault induced harmonics there is a need to define a lower limit for the detectability of the harmonic sidebands. Without an experimental setup or prior knowledge about the level of noise in a hydrogenator, this thesis bases the lowest level of detectability on the noise level shown in the results of the experimental setup of [17]. The noise for the static and dynamic eccentricity conditions are lower than -100 [dB] even for high degrees of static and dynamic eccentricity, shown by figure 6.1 and 6.2. The noise level for mixed eccentricity is higher, as seen in figure 6.3. The highest level of noise here seems to lay below -85 [dB]. Therefore, the lowest detectability limit for the dynamic and static eccentricity is set to -100 [dB] and -85 [dB] for mixed eccentricity. Since there were no experimental setup of rotor ITSC with static eccentricity, this thesis assumes the harshest detectability limit of -85 [dB] for rotor ITSC with static eccentricity.

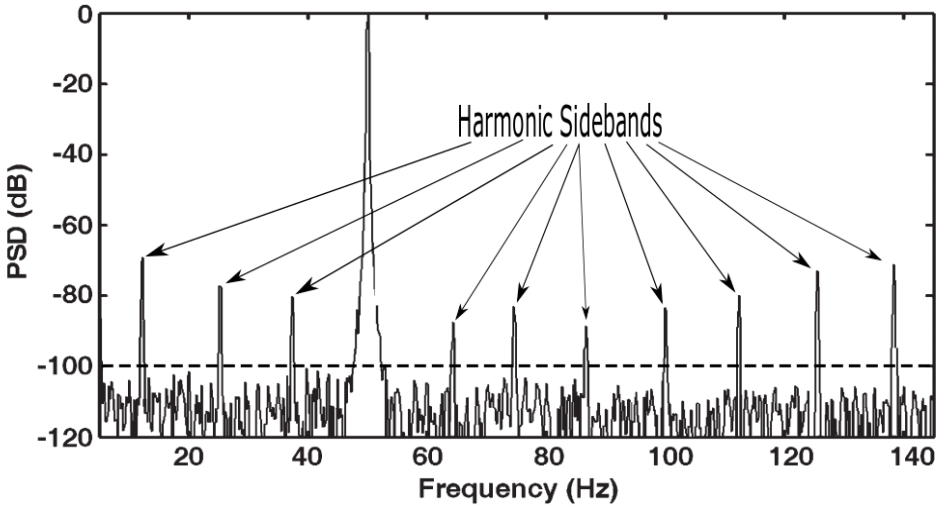

Figure 6.1: Experimental results from a PMSM with static eccentricity, taken from [13].

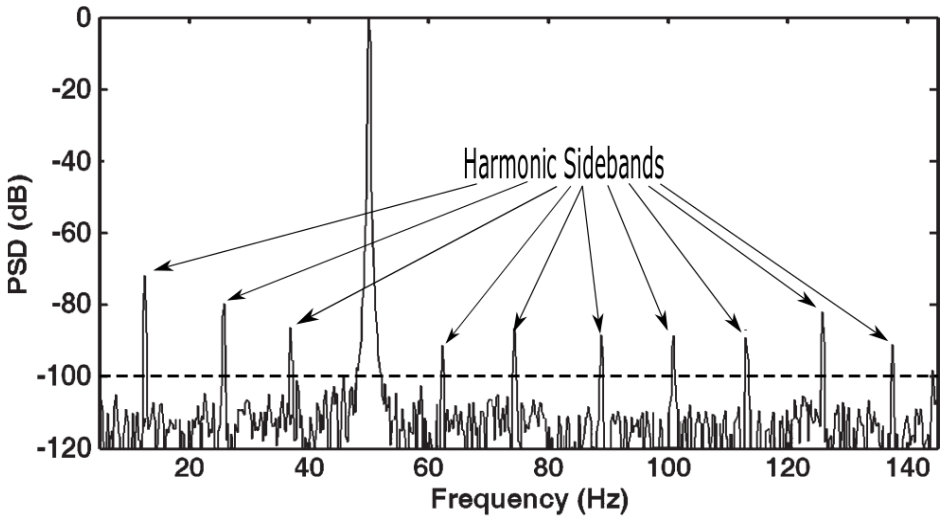

Figure 6.2: Experimental results from a PMSM with dynamic eccentricity, taken from [13].

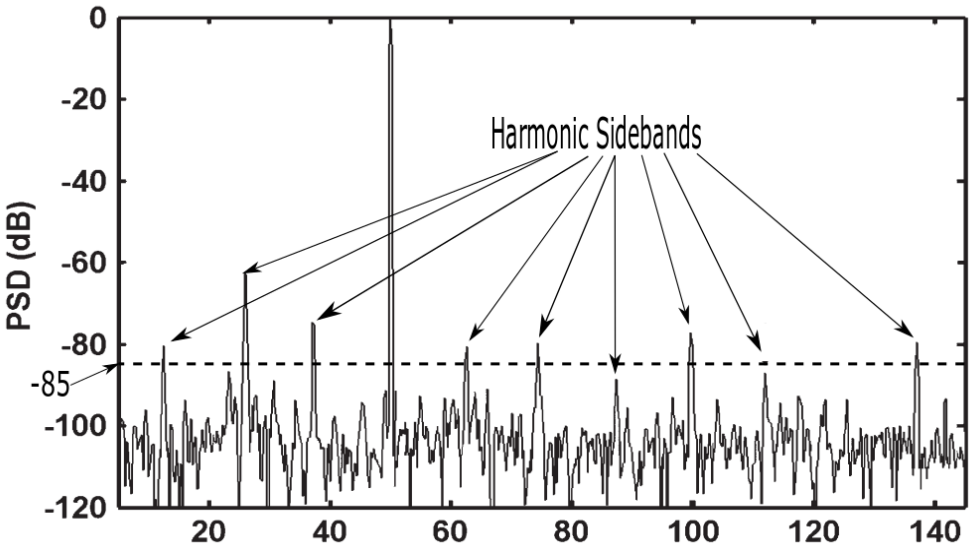

Figure 6.3: Experimental results from a PMSM with mixed eccentricity, taken from [13].

6.1.1 Discussion No-load Simulation Results

The results from chapter 5.1 show that in the no-load condition the rotor ITSC faults, both with and without static eccentricity, and the eccentricity conditions produce fault induced harmonic sidebands in the phase voltage. The amplitude of these harmonic sidebands are dependent on the degree of fault severity and therefore might be suitable for detection and monitoring of the condition of the generator.

From figure 5.5 it is clear that the proposed method unsuited for detection of static eccentricity. This because the harmonic sidebands produced by the static eccentricity conditions are only detectable at very high, critical levels of fault severity.

From figure 5.3 the most prominent harmonic sidebands produced by the rotor ITSC without static eccentricity are the 25[Hz], 75[Hz], 125[Hz] and the 175[Hz], they all increase in amplitude with increasing fault severity and are therefore all suitable for fault detection and condition monitoring. From table 5.1 it is clear that the 75[Hz] has the highest amplitude and is the most suited indicator. The 75[Hz] has amplitudes above the assumed lowest detection level even at low degrees of fault severity and could be used early detection and condition monitoring, this was already found in [1].

From figure 5.4 the most prominent harmonic sidebands produced by the dynamic eccentricity conditions are the 25[Hz], 75[Hz], 125[Hz] and 175[Hz], where they all increase with increasing fault severity. From table 5.3 it is clear that the 75[Hz] has the highest amplitude, with the assumed lowest detection level, it should be detectable around the level where the degree of dynamic eccentricity becomes problematic, according to the conservative tolerance values given by table 2.1. The 75 [Hz] can be used for detection of problematic levels of dynamic eccentricity.

As mentioned in the two previous paragraphs, and also seen by comparing figure 5.3 and figure 5.4, the same detectable harmonic sidebands are produced by rotor ITSC faults and the dynamic eccentricity conditions. This means that a using a single sideband harmonic, like the 75[Hz], cannot differentiate the two fault cases from each other. Being able to discriminate between the two cases can reduce the time spent troubleshooting, saving time and money in the process. Although the two cases produce the sideband harmonics of the same frequencies, the amplitude relation between the sideband harmonics are not the same. This difference can be used to differentiate the cases, there are most likely several relations which

can be used for this. This thesis proposes using the difference in amplitude between two of the most prominent harmonic sidebands, the 25 [Hz] and the 75 [Hz], seen in table 5.4 and 5.2 for dynamic eccentricity and rotor ITSC, respectively. As seen from the table 5.2 the $A_{75[Hz]} - A_{25[Hz]} \sim 5dB$ for all the simulated cases of rotor ITSC, here $A_{25[Hz]}$ and $A_{75[Hz]}$ is the amplitude of the 25[Hz] and the 75[Hz] harmonic sideband, respectively. For dynamic eccentricity the difference starts at $A_{75[Hz]} - A_{25[Hz]} > 11dB$, and seems to be increasing with fault severity, as seen in table 5.4. These characteristics can therefore be used to differentiate the cases. If the 25[Hz] is not detectable, the fault is dynamic eccentricity, because the 25[Hz] would be detectable for even low levels of rotor ITSC. This assuming the lowest detectability level of -100[dB] and the that no other fault induce similar harmonics, or there the 25[Hz] has been eliminated by the generator topology, which we will see can happen later in the discussion.

From figure 5.7 the most prominent harmonic sidebands in the case of rotor ITSC fault with static eccentricity is the 25[Hz], 37.5[Hz], 62.5[Hz] and 75[Hz], they all increase with increasing fault severity, and could be used for fault detection. The 75[Hz] has the highest amplitude for all the simulated cases, but as seen in table 5.9, the 75[Hz] is highly dependent on the number of shorted turns and the effect of static eccentricity is nearly neglectable. Therefore, either the 37.5[Hz] or the 62.5[Hz], which are dependent on the degree of static eccentricity, should be used with the 75[Hz] to detect and monitor the condition. Since the condition is caused by two fault conditions there is a benefit in being able to classify the

severity of each of them to be able optimize the maintenance. For the classification the 25[Hz] or the 75[Hz] can be used to estimate the number of shorted turns since they are almost exclusively dependent on the number of shorted circuits. The 37.5[Hz] and the 62.5[Hz] are dependent on both and can be used together with the estimated number of shorted turns to estimate the degree of static eccentricity. Table 5.8 show that if there are less than 5 shorted turns, the 37.5[Hz] and the 62.5[Hz] would not be detectable even at critical levels of static eccentricity. This means that the method can detect the rotor ITSC with static eccentricity fault at low severities, but the static eccentricity component would be hidden with less than 5 shorted turns.

From figure 5.6 the most prominent harmonics in the case of mixed eccentricity are the 25 [Hz], 37.5 [Hz], 62.5 [Hz] and 75[Hz], they all increase with increasing fault severity, and could be used for fault detection. Like for the case of rotor ITSC with static eccentricity, the 25[Hz] and the 75[Hz] are heavily dependent on the degree of dynamic eccentricity and marginally affected by the degree of static eccentricity, seen in table 5.6. Therefore, the same classification technic as proposed for rotor ITSC with static eccentricity can be used for mixed eccentricity, where the 25[Hz] or the 75[Hz] is used to estimate the degrees of dynamic eccentricity. However, based on the values in table 5.5 and the assumed lowest detectability to be around the -85 [dB], the classification only works for eccentricity conditions which are well into the critical region. The eccentricity condition fault should however be detectable as it enters the critical levels by the 62.5 [Hz] sideband.

As seen in the previous two paragraphs, and by comparing figure 5.6 and figure 5.7, the rotor ITSC with static eccentricity and mixed eccentricity give rise to the same detectable harmonic sidebands. However, like for the case of dynamic eccentricity condition and rotor ITSC without static eccentricity, they can be separated by $A_{75[Hz]} - A_{25[Hz]}$, where for rotor ITSC with static eccentricity $A_{75[Hz]} - A_{25[Hz]} \sim 5$ [dB] and for mixed $A_{75[Hz]} - A_{25[Hz]} > 12$ [dB] and increasing. If the 25[Hz] or the 75[Hz] is not detectable it indicates mixed eccentricity, because as seen in table 5.8 even the lowest number of shorted turns makes them detectable. This is based on the same assumptions as given for the differentiation of dynamic eccentricity and rotor ITSC without static eccentricity.

Differentiating between pure dynamic eccentricity and rotor ITSC with static eccentricity can be done by detecting the 37.5[Hz] or the 62.5[Hz] sidebands, or by the difference in the amplitude of the 25[Hz] and the 75[Hz]. Pure dynamic eccentricity can be differentiated from the mixed eccentricity by detecting the 37.5[Hz] and the 62.5[Hz].

Similarly, the rotor ITSC without static eccentricity can be discriminated from mixed eccentricity by the difference in the 25[Hz] and the 75[Hz] amplitudes or by the detection of the 37.5 [Hz] and the 62.5[Hz] harmonic sideband. The rotor ITSC without static eccentricity can be separated from rotor ITSC with static eccentricity by the detection of the 37.5 [Hz] and the 62.5[Hz]. This might not always be possible, and as seen by table 5.8 a high degree of static eccentricity can be hidden from the detection method.

The differentiation and classification technique require prior knowledge about how the generator reacts to certain degrees of fault conditions, this can be found through simulations.

6.1.2 Discussion of the Full-load Simulation Results

The full-load results for stator phase voltage found in chapter 5.2 are quite similar to the no-load results, the same prominent harmonic sidebands are produced and they are still affected by the fault severity. The amplitude and relation between them has changed slightly. The amplitude of the rotor ITSC faults, both with and without static eccentricity, has been increased for all the prominent sidebands, as seen in table 5.11 and 5.21. The amplitude sidebands for dynamic and mixed eccentricity has decreased, making the fault conditions harder to detect. The method should still be able to detect dynamic eccentricity as it enters into critical levels, as seen in table 5.14. The method might however not be able to detect lower critical levels of mixed eccentricity, as seen by table 5.17. The 75[Hz] are still the most suited indicator detection of all the faults, but the 62.5[Hz] seems to no longer be strictly increasing with fault severity, seen in figure 5.18 and 5.22, but the 37.5[Hz] is, and is therefore more suited as fault indicator.

The differentiation, discussed for the no-load simulation, based on the difference in amplitude of the 75[Hz]'s and the 25[Hz]'s is still valid, as seen by table 5.12, 5.15, 5.19 and 5.23. The classification technique is also still valid as seen by the 25[Hz] and 75[Hz] high dependency on the rotor ITSC or degree of dynamic eccentricity, as seen in table 5.18 and 5.22.

The results of the full-load phase current show the same prominent harmonic sidebands as the full-load phase voltage, except for the 75[Hz] and it's multiples (i.e. 150 [Hz], 225[Hz], etc.). In the case of rotor ITSC and dynamic eccentricity, 75[Hz] and 225[Hz] sideband harmonics are eliminated. The reason for this, as mentioned in chapter 3, is that the winding configuration of a wye-connected generator has a floating neutral

point which eliminates certain harmonics, as stated and found in [19]. The 75[Hz] and its multiples are drastically reduced in the case of mixed eccentricity and rotor ITSC with static eccentricity. The reason why the sidebands are not entirely eliminated is probably connected to the static eccentricity component. For as seen in figure 5.12 and 5.13 the sidebands of the static eccentricity are unaffected by this phenomenon. The reason for this is was not found in this study. Since the 75[Hz] harmonic sideband is the most useful indicator for detection, differentiation and classification analysing the phase voltage is better suited for the proposed method.

With an overview of the simulations on Machine 1, it is clear that some of the fault conditions produce detectable sideband harmonics, and that the relationship between them is dependent on the type of fault condition which produced them. The thesis has already proposed some solutions for detecting, differentiating and classifying the faults based on the harmonic spectrum they produce, but it is worth mentioning that a neural-network might be better suited for the detection classification and differentiation. The indicators, that being the frequencies and their amplitudes, are well suited for a neural-network. The neural-network might be able to find hidden relations between the harmonic sidebands, which might improve the detection and classification of the different fault conditions. A neural-network was successfully used to classify the degree of static and dynamic eccentricity of a PMSM within mixed eccentricity in [17]. This thesis will not look further into the use of a neural-network.

The results of the simulations of Machine 2, chapter 5.3, shows that the proposed methods detection capability is highly dependent on the generator topology. The change from 126 slots to 120 slots, effectively going from a generator with a fractional to an integer winding layout, has eliminated some sidebands from the frequency spectrum. The change has caused the elimination of the sidebands with the frequencies:

$$f_{sideband} = \left(1 \pm \frac{k}{2}\right) f_s, \tag{49}$$

where k=1,3,5… This effectively eliminates all the harmonic sidebands found in the simulations of the dynamic eccentricity conditions and rotor ITSC faults. This is similar to the results found in [19], where all the sideband harmonics in a PMSM with double layer-windings and with a defect pole magnet were eliminated with generators when the relation:

$$\frac{N_s}{2P} = \frac{3}{2}k, \tag{50}$$

where $k = 1,2,3$ ... With 120 slots and 8 poles this generator matches the pattern with k=10. This indicates that the method might not be suited for detection of dynamic eccentricity and rotor ITSC faults in hydro generators which fits the relation of equation 50, but further testing is required to verify this. Machine 4 does not follow the pattern and does not have elimination of any prominent sideband harmonics.

For Machine 2 with mixed eccentricity, the proposed method can still detect the eccentricity condition by looking at the 37.5[Hz] and the 62.5[Hz]. However, the elimination has removed all the sidebands which

had a high dependency on the degree of dynamic eccentricity and the proposed method for classification of mixed eccentricity is no longer valid.

The rotor ITSC with static eccentricity was not simulated for Machine 3, because of the time constraint. However, based on the result of the rotor ITSC without static eccentricity and the results from the mixed eccentricity simulation, it can be assumed that the same harmonic sidebands are eliminated and that the remaining prominent sidebands of 37.5[Hz] and 62.5[Hz] can still be used for fault detection. This needs to be verified through simulations or physical experiment. The elimination of the 75[Hz] and the 25[Hz] sidebands has drastically reduced the capability to detect faults and a moderate number of short circuits and/or a large degree of static eccentricity has to occur before method detects the fault condition.

The results of simulation of Machine 2, shows that the method is highly dependent on the generator topology. This dependency should be studied further both in relation to harmonic elimination, but also with a focus on how the relation between the harmonic sidebands change with change topology.

With an overview of chapter 5.1, 5.2 and 5.3 its clear that rotor ITSC, both with and without static eccentricity and dynamic and mixed eccentricity condition give rise to detectable sideband harmonics. The detected harmonic sidebands all fall within the frequency spectrum calculated in chapter 3. That being, they all fit equation 51:

$$f_{harmonic} = \left(1 \pm \frac{k}{P}\right) f_s, \tag{51}$$

where P is the number of pole pairs and f_s is the synchronous frequency and k=1,2,3…

Not all the sidebands predicted by equation 51 appear, especially in the case for dynamic eccentricity and rotor ITSC where the sideband harmonics around the main harmonic follow the pattern in equation 52:

$$f_{harmonic} = \left(1 \pm \frac{2k}{P}\right) f_s, \tag{52}$$

K=1,2,3,… The reason for the “missing” sideband harmonics in all the fault cases is probably the simplifications done when calculating the pattern given in equation 51. The simplifications of not taking into account the generator saliency, effect of stator and damper slots, the effect of the damper bars, winding layout, etc. have probably given a too inclusive frequency pattern. The impact of the slots is highlighted by the results of Machine 2. The calculations also do not take the values of the coefficients in equation 22, 23 and 24 into account, so some elimination might be caused by those. Further study, with more advanced calculations is needed to give a better understanding of the harmonics produced by the different fault cases, but are out of scope in this thesis.

The static eccentricity, which was calculated to not have sideband harmonics do. The reason for why static eccentricity induce fault related sidebands was not found in this study and further study is needed.

7 Conclusion and Further Work

The aim of this master thesis's was to investigate an on-line, non-invasive fault detection method's capability to detect and monitor the static eccentricity, dynamic eccentricity, mixed eccentricity and rotor ITSC with static eccentricity in a hydrogenator and its ability differentiate between eccentricity and rotor ITSC faults. The method is based on the fact that an asymmetrical air-gap flux distribution produces sideband harmonics in the terminal output signals. These harmonics can then be found through a harmonic analysis of the terminal signals. The method was investigated by simulating the eccentricity conditions and the rotor ITSC through TSFE-simulations and the resulting stator phase voltage and current was analysed. The simulations were done on a model based on a real hydrogenator and three other models which were based on the same generator, but with minor modifications. The conclusion is based on an assumed lowest detectability of -100[dB] for rotor ITSC, dynamic and static eccentricity, and -85[dB] for mixed eccentricity and rotor ITSC with static eccentricity and the assumption of eccentricity tolerances given by table 2.1.

The simulation of one of the modified models showed that the method is highly dependent on the generator topology and is in some cases unable to detect rotor interturn fault or dynamic eccentricity, even with high fault severity. The method was not able to detect these fault conditions on an integer generator. Where the relation between the number slots over number of poles matches the pattern found in [19] to eliminate the fault related sideband harmonics, that being $\frac{N_s}{2P} = \frac{3}{2}k$, where k=1,2,3....

The analysis of the unmodified model showed that the method is not suited for detection of static eccentricity. The harmonics produced by the static

eccentricity was too small, even at high critical levels of static eccentricity. The method was shown to be able to detect dynamic eccentricity as the degree of dynamic eccentricity enters the critical levels, at both full-load and no-load, by using the 75[Hz] harmonic sideband as indicator. The same was found for mixed eccentricity at no-load, but at full-load low critical levels of mixed eccentricity might go undetected. Mixed eccentricity uses the 75[Hz] and the 37.5[Hz] harmonic sideband as indicators. The rotor ITSC with static eccentricity was shown to be able to detect and monitor the faults at low levels of fault severity, using the 75[Hz] and 37.5[Hz] as indicator, although the static eccentricity component might be hidden. The rotor ITSC without static eccentricity was found to be detectable using the 75[Hz] as indicator as found in [1].

A technique based on the difference in amplitude between the 25[Hz] and the 75[Hz] harmonic sideband was proposed for differentiating between the cases with rotor ITSCs and those with dynamic or mixed eccentricity. A technique to classify the degrees of dynamic and static eccentricity in a generator with mixed eccentricity, and the degrees of static eccentricity and number of shorted turns in a generator with rotor ITSC with static eccentricity was proposed. This technique uses the amplitude 75[Hz] sideband, which is highly dependent on either dynamic eccentricity in mixed eccentricity or number of shorted turns in rotor ITSC with static eccentricity, to estimate the severity of either dynamic eccentricity or the ITSC. From this it uses the amplitude of the 37.5[Hz] to estimate the degree of static eccentricity. The techniques require some prior knowledge of how the generator responses to the different fault types and levels, which can be found through simulations. The classification technique is unsuited for low

to moderate levels of fault severity, depending on the fault type. Therefore, as future work the development of a neural-network, which might be able to find hidden relations between the sideband harmonics, was proposed.

Since the results were achieved through simulations, and the lowest detectability level is based on assumption, there is a dire need for verifying the results through physical experimentation. The produced harmonic sidebands' dependency on generator topology and loading also needs to be studied further, both with more complex mathematics and through simulation and physical experimentation.

To further improve the understanding of this fault monitoring method. A study on how the generator responds to a fault scenario where mixed eccentricity occurs together with rotor ITSC, and a study on how location and severity of rotor ITSC on multiple poles affects the frequency spectrum of the terminal signals, could be of interest.

The conclusion is that the proposed method is highly dependent on the generator topology, but might be used for early detection and monitoring of rotor ITSCs with static eccentricity, and without as found by [1]. The method might be used to detect dynamic eccentricity as it enters critical levels, while some critical levels of mixed eccentricity can go undetected with the proposed method. The method was unable to detect static eccentricity. There is a need for physical experiments to verify the simulation results, and the detectability assumption made in this thesis.

Bibliography:

[1] K. G. Jørstad, “Modelling, Simulation, and Online Detection of Rotor Fault in Hydrogenerators,” M.S. thesis, Dept. Electrical Power Engineering, NTNU, Trondheim, 2017.

[2] Elektrisitet https://www.ssb.no/energi-og-industri/statistikker/elektrisitet, Accessed: 2018-5-20.

[3] M. Rausand and A. Høyland System reliability theory: models and statistical methods, 2th ed. New York, Wiley, 1994.

[4] T. C. Wiborg, Maintenance strategies: Principles and practical applications, Trondheim, Norway, Norwegian University of Science and Technology, 2002.

[5] Peter Tavner, Li Ran and Jim Penman. Condition monitoring of electrical machines. Vol 56. IET, 2008.

[6] Jawad Faiz and S.M.M.Moosavi “Eccentricity fault detection – From induction machines to DFIG—A review” in Renewable and Sustainable Energy Reviews, Vol 55, March 2016, Pages 169-179

[7] Hamid A Toliyat, et al. Electric machines: modelling, condition monitoring and fault diagnosis. CRC press, 2012.

[8] Course material: “Vannkraftgenerator, drift og vedlikehold”, Oslo: EBL kompetanse AS, 2008.

[9] L. Wang, R. W. Cheung, Z. Ma, J. Ruan and Y. Peng, "Finite-Element Analysis of Unbalanced Magnetic Pull in a Large Hydro-Generator Under Practical Operations," in IEEE Transactions on Magnetics, vol. 44, no. 6, pp. 1558-1561, June 2008.

[10] S. Nandi, H. A. Toliyat and X. Li, "Condition monitoring and fault diagnosis of electrical motors-a review," in IEEE Transactions on Energy Conversion, vol. 20, no. 4, pp. 719-729, Dec. 2005.

[11] J. R. Cameron, W. T. Thomson and A. B. Dow, "Vibration and current monitoring for detecting airgap eccentricity in large induction motors," in IEE Proceedings B - Electric Power Applications, vol. 133, no. 3, pp. 155-163, May 1986.

[12] E. A. Kaggestad, private communication, Februar 2018.

[13] Mechanical Tolerance Guidelines for Hydroelectric Generators. https://vibrosystm.com/wp-content/uploads/AN001-a.pdf. Accessed: 2018-5-20.

[14] A general guide to the principles, operation and troubleshooting of hydrodynamic bearings", Kingsbury Inc, Philadelphia, PA, pp 16-24

[15] G. C. Stone, M. Sasic, J. Stein and C. Stinson, "Using magnetic flux monitoring to detect synchronous machine rotor winding shorts," Conference Record of 2012 Annual IEEE Pulp and Paper Industry Technical Conference (PPIC), Portland, OR, 2012, pp. 1-7.

[16] W. Yucai, L. Yonggang and L. Heming, "Diagnosis of turbine generator typical faults by shaft voltage," 2012 IEEE Industry Applications Society Annual Meeting, Las Vegas, NV, 2012, pp. 1-6.

[17] B. M. Ebrahimi, J. Faiz and M. J. Roshtkhari, "Static-, Dynamic-, and Mixed-Eccentricity Fault Diagnoses in Permanent-Magnet Synchronous Motors," in IEEE Transactions on Industrial Electronics, vol. 56, no. 11, pp. 4727-4739, Nov. 2009.

[18] C. P. Salomon et al., "Discrimination of Synchronous Machines Rotor Faults in Electrical Signature Analysis Based on Symmetrical Components," in IEEE Transactions on Industry Applications, vol. 53, no. 3, pp. 3146-3155, May-June 2017.

[19] M. Zafarani, T. Goktas and B. Akin, "A Comprehensive Magnet Defect Fault Analysis of Permanent-Magnet Synchronous Motors," in IEEE Transactions on Industry Applications, vol. 52, no. 2, pp. 1331-1339, March-April 2016.

[21] JAWAD FAIZ, IMAN TABATABAEI & E. SHARIFI-GHAZVINI (2010) “A Precise Electromagnetic Modeling and Performance Analysis of a Three-Phase Squirrel-Cage Induction Motor under Mixed Eccentricity Condition”, Electromagnetics, 24:6, 471-489.

[22] C. Bruzzese, "Diagnosis of Eccentric Rotor in Synchronous Machines by Analysis of Split-Phase Currents—Part I: Theoretical Analysis," in IEEE Transactions on Industrial Electronics, vol. 61, no. 8, pp. 4193-4205, Aug. 2014.

[23] S. J. Chapman, “AC Machinery Fundamentals”, in Electric Machinery Fundamentals, 5th ed. New York, USA: Mc Graw Hill Education, 2012, ch. 3, sec 2, pp. 164-166.

[24] B. M. Ebrahimi, M. Javan Roshtkhari, J. Faiz and S. V. Khatami, "Advanced Eccentricity Fault Recognition in Permanent Magnet Synchronous Motors Using Stator Current Signature Analysis," in IEEE Transactions on Industrial Electronics, vol. 61, no. 4, pp. 2041-2052, April 2014.

[25] D. G. Dorrell, W. T. Thomson and S. Roach, "Analysis of airgap flux, current, and vibration signals as a function of the combination of static and

dynamic airgap eccentricity in 3-phase induction motors," in IEEE Transactions on Industry Applications, vol. 33, no. 1, pp. 24-34, Jan/Feb 1997.

[26] Li Yonggang, Li Heming, Zhao Hua and Wan Shuting, "Fault identification method of rotor inter turn short-circuit using stator winding detection," Sixth International Conference on Electrical Machines and Systems, 2003. ICEMS 2003., Beijing, China, 2003, pp. 856-860 vol.2.

[27] P. V. O'Neil, "Fourier Series", in Advanced Engineering Mathematics, 6th ed. Toronto, Nelson, 2007. ch. 14, pp. 583-699.

[28] Ansys, "Ansys 18.2 Maxwell Online help", Ansys, Inc. and Ansys Europe, July 2017.

[29] Mostafa Valavi, private communication, October 2017.

[30] J. W. Nilsson, S. A. Riedel, "Techniques of Circuit Analysis", in Electric Circuits, 10th ed. Boston, USA: Pearson, 2015, ch. 4, sec 12, pp. 142.

[31] O.W Andersen, "Synchronous Machine Stator Leakage Reactance", Notat, Institutt For Elektriske Maskiner, Norges Tekniske Høgskole. Trondheim, 1985.

[32] C. Bruzzese, "Diagnosis of Eccentric Rotor in Synchronous Machines by Analysis of Split-Phase Currents—Part II: Experimental Analysis," in IEEE Transactions on Industrial Electronics, vol. 61, no. 8, pp. 4206-4216, Aug. 2014.

[33] M. Zafarani, T. Goktas, B. Akin and S. E. Fedigan, "An Investigation of Motor Topology Impacts on Magnet Defect Fault Signatures," in IEEE Transactions on Industrial Electronics, vol. 64, no. 1, pp. 32-42, Jan. 2017.

Appendix A: Figures and Input data related to the modelling:

A.1 FEM of Machine 2

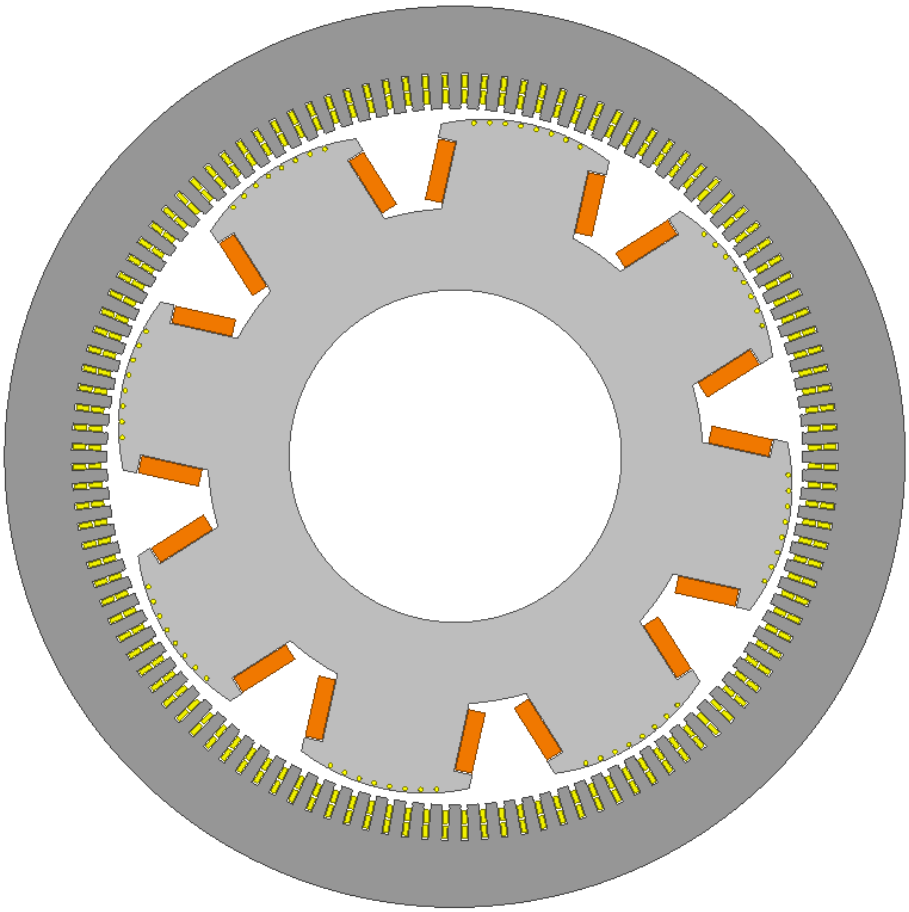

Figure A.1: Figure of the FEM model of Machine 2.

A.2 FEM of Machine 4

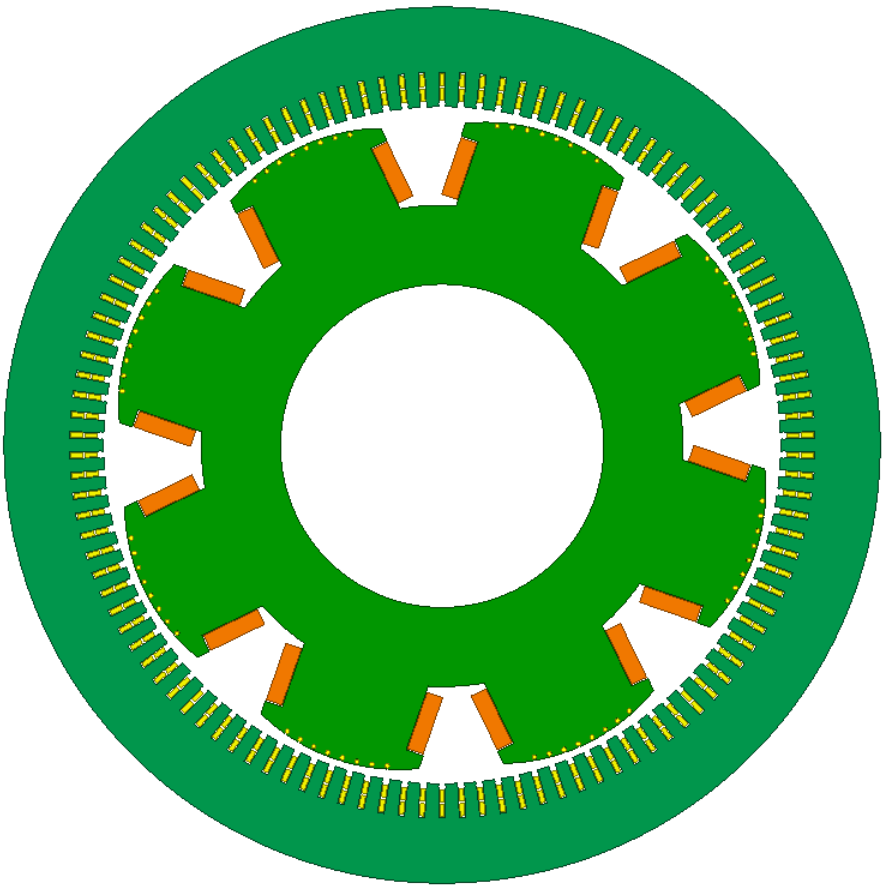

Figure A.2: Figure of the FEM of Machine 4.

A.3 Stator UDP Input values for Machine 1 and 2

	Name	Value	Unit	Evaluated Value	Description
	Command	CreateUserDefinedPart			
	Coordinate System	Global			
	Name	RMxprt/SlotCore.dll			
	Location	syslib			
	Version	12.1			
	DiaGap	2040	mm	2040mm	Core diameter on gap side, DiaGap<DiaYoke for outer c
	DiaYoke	2640	mm	2640mm	Core diameter on yoke side, DiaYoke<DiaGap for inner c
	Length	0	mm	0mm	Core length
	Skew	0	deg	0deg	Skew angle in core length range
	Slots	126		126	Number of slots
	SlotType	6		6	Slot type: 1 to 6
	Hs0	7	mm	7mm	Slot opening height
	Hs01	0	mm	0mm	Slot closed bridge height
	Hs1	6	mm	6mm	Slot wedge height
	Hs2	91	mm	91mm	Slot body height
	Bs0	0	mm	0mm	Slot opening width
	Bs1	25	mm	25mm	Slot wedge maximum width
	Bs2	20	mm	20mm	Slot body bottom width, 0 for parallel teeth
	Rs	0	mm	0mm	Slot body bottom fillet
	FilletType	0		0	0: a quarter circle; 1: tangent connection; 2&3: arc botto
	HalfSlot	0		0	0 for symmetric slot, 1 for half slot
	SegAngle	0	deg	0deg	Deviation angle for slot arches (10~30, <10 for true surfa
	LenRegion	3000	mm	3000mm	Region length
	InfoCore	0		0	0: core; 1: solid core; 100: region.

Figure A.3: Input values for the UDP used for the stator for Machine 1 and 2

A.4 Stator UDP Input values for Machine 2

	Name	Value	Unit	Evaluated Value	Description
	Command	CreateUserDefinedPart			
	Coordinate System	Global			
	Name	RMxprt/SlotCore.dll			
	Location	syslib			
	Version	12.1			
	DiaGap	2040	mm	2040mm	Core diameter on gap side, DiaGap<DiaYoke for outer core
	DiaYoke	2640	mm	2640mm	Core diameter on yoke side, DiaYoke<DiaGap for inner con
	Length	0	mm	0mm	Core length
	Skew	0	deg	0deg	Skew angle in core length range
	Slots	120		120	Number of slots
	SlotType	6		6	Slot type: 1 to 6
	Hs0	7	mm	7mm	Slot opening height
	Hs01	0	mm	0mm	Slot closed bridge height
	Hs1	6	mm	6mm	Slot wedge height
	Hs2	91	mm	91mm	Slot body height
	Bs0	0	mm	0mm	Slot opening width
	Bs1	25	mm	25mm	Slot wedge maximum width
	Bs2	20	mm	20mm	Slot body bottom width, 0 for parallel teeth
	Rs	0	mm	0mm	Slot body bottom fillet
	FilletType	0		0	0: a quarter circle; 1: tangent connection; 2&3: arc bottom.
	HalfSlot	0		0	0 for symmetric slot, 1 for half slot
	SegAngle	0	deg	0deg	Deviation angle for slot arches (10~30, <10 for true surface
	LenRegion	3000	mm	3000mm	Region length
	InfoCore	0		0	0: core; 1: solid core; 100: region.

Figure A.4: Input values for the UDP used for the stator for Machine 3

A.5 Stator UDP Input values for Machine 4

	Name	Value	Unit	Evaluated Value	Description
	Command	CreateUserDefinedPart			
	Coordinate System	Global			
	Name	RMxprt/SlotCore.dll			
	Location	syslib			
	Version	12.1			
	DiaGap	2040	mm	2040mm	Core diameter on gap side, DiaGap<DiaYoke for outer cores
	DiaYoke	2640	mm	2640mm	Core diameter on yoke side, DiaYoke<DiaGap for inner core
	Length	0	mm	0mm	Core length
	Skew	0	deg	0deg	Skew angle in core length range
	Slots	114		114	Number of slots
	SlotType	6		6	Slot type: 1 to 6
	Hs0	7	mm	7mm	Slot opening height
	Hs01	0	mm	0mm	Slot closed bridge height
	Hs1	6	mm	6mm	Slot wedge height
	Hs2	91	mm	91mm	Slot body height
	Bs0	0	mm	0mm	Slot opening width
	Bs1	25	mm	25mm	Slot wedge maximum width
	Bs2	20	mm	20mm	Slot body bottom width, 0 for parallel teeth
	Rs	0	mm	0mm	Slot body bottom fillet
	FilletType	0		0	0: a quarter circle; 1: tangent connection; 2&3: arc bottom.
	HalfSlot	0		0	0 for symmetric slot, 1 for half slot
	SegAngle	0	deg	0deg	Deviation angle for slot arches (10~30, <10 for true surface).
	LenRegion	3000	mm	3000mm	Region length
	InfoCore	0		0	0: core; 1: solid core; 100: region.

Figure A.3: Input values for the UDP used for the stator for Machine 4

A.7 Rotor UDP Input Values

Name	Value	Unit	Evaluated Value
Command	CreateUserDefinedPart		
Coordinate System	Global		
Name	RMxprt/SalientPoleCore.dll		
Location	syslib		
Version	17.0		
DiaGap	1994	mm	1994mm
DiaYoke	974	mm	974mm
Length	0	mm	0mm
Skew	0	deg	0deg
Slots	8		8
SlotType	1		1
Hs0	3.75	mm	3.75mm
Hs01	0	mm	0mm
Hs1	0	mm	0mm
Hs2	0	mm	0mm
Bs0	4	mm	4mm
Bs1	13.5	mm	13.5mm
Bs2	13.5	mm	13.5mm
Rs	0	mm	0mm
FilletType	1		1
SlotPitch	4.5	deg	4.5deg
CenterPitch	4.5	deg	4.5deg
Poles	8		8
PoleType	1		1
WidthShoe	504	mm	504mm
HeightShoe	95.85	mm	95.85mm
WidthBody	395	mm	395mm
HeightBody	203.15	mm	203.15mm
AirGap2	0	mm	0mm
Offset	400	mm	400mm
Off2_x	0	mm	0mm
Off2_y	0	mm	0mm
Bp1/Rp1	0	mm	0mm
Bp2/Rp2	0	mm	0mm
CoilEndExt	2	mm	2mm
EndRingType	2		2
BarEndExt	2	mm	2mm
RingLength	5	mm	5mm
RingHeight	6	mm	6mm
SegAngle	0	deg	0deg
LenRegion	2000	mm	2000mm
InfoCore	0		0

Figure A.7 Input values for the UDP used for the rotor in all the models

A.6 Winding layout Machine for all the Models

Table A.6: The table shows the winding layout of the four machine models. A, B, C symbolises the three different phases and Top and Bot symbolises if the winding is placed in the top or bottom layer of the slot.

	Machine 1		Machine 2		Machine 3		Machine 4	
Slot Nr.	**Top**	**Bot**	**Top**	**Bot**	**Top**	**Bot**	**Top**	**Bot**
1	**A**	**A**	**A**	**A**	**A**	**A**	**A**	**A**
2	**A**	**A**	**A**	**A**	**A**	**A**	**A**	**A**
3	**A**	**A**	**A**	**A**	**A**	**A**	**A**	**A**
4	**A**	**-B**	**A**	**-B**	**A**	**A**	**A**	**-B**
5	**A**	**-B**	**A**	**-B**	**A**	**A**	**A**	**-B**
6	**A**	**-B**	**-B**	**-B**	**A**	**-B**	**A**	**-B**
7	**-B**	**-B**	**-B**	**-B**	**-B**	**-B**	**-B**	**-B**
8	**-B**	**-B**	**-B**	**-B**	**-B**	**-B**	**-B**	**-B**
9	**-B**	**C**	**-B**	**C**	**-B**	**-B**	**-B**	**C**
10	**-B**	**C**	**-B**	**C**	**-B**	**-B**	**-B**	**C**
11	**-B**	**C**	**C**	**C**	**-B**	**C**	**-B**	**C**
12	**C**	**C**	**C**	**C**	**C**	**C**	**C**	**C**
13	**C**	**C**	**C**	**C**	**C**	**C**	**C**	**C**
14	**C**	**-A**	**C**	**-A**	**C**	**C**	**C**	**-A**
15	**C**	**-A**	**C**	**-A**	**C**	**C**	**C**	**-A**
16	**C**	**-A**	**-A**	**-A**	**C**	**-A**	**C**	**-A**
17	**-A**	**-A**	**-A**	**-A**	**-A**	**-A**	**-A**	**-A**
18	**-A**	**-A**	**-A**	**-A**	**-A**	**-A**	**-A**	**-A**
19	**-A**	**-A**	**-A**	**B**	**-A**	**-A**	**-A**	**-A**
20	**-A**	**B**	**-A**	**B**	**-A**	**-A**	**-A**	**B**

21	-A	B	B	B	-A	-A	-A	B
22	B	B	B	B	B	B	B	B
23	B	B	B	B	B	B	B	B
24	B	B	B	-C	B	B	B	B
25	B	-C	B	-C	B	B	B	-C
26	B	-C	-C	-C	B	B	B	-C
27	B	-C	-C	-C	B	-C	-C	-C
28	-C	-C	-C	-C	-C	-C	-C	-C
29	-C	-C	-C	A	-C	-C	-C	-C
30	-C	A	-C	A	-C	-C	-C	A
31	-C	A	A	A	-C	-C	-C	A
32	-C	A	A	A	-C	A	A	A
33	A	A	A	A	A	A	A	A
34	A	A	A	-B	A	A	A	A
35	A	-B	A	-B	A	A	A	-B
36	A	-B	-B	-B	A	A	A	-B
37	A	-B	-B	-B	A	-B	-B	-B
38	-B	-B	-B	-B	-B	-B	-B	-B
39	-B	-B	-B	C	-B	-B	-B	-B
40	-B	-B	-B	C	-B	-B	-B	C
41	-B	C	C	C	-B	-B	-B	C
42	-B	C	C	C	-B	-B	C	C
43	C	C	C	C	C	C	C	C
44	C	C	C	-A	C	C	C	C
45	C	C	C	-A	C	C	C	-A
46	C	-A	-A	-A	C	C	C	-A
47	C	-A	-A	-A	C	C	C	-A
48	C	-A	-A	-A	C	-A	-A	-A

49	-A	-A	-A	B	-A	-A	-A	-A
50	-A	-A	-A	B	-A	-A	-A	B
51	-A	B	B	B	-A	-A	-A	B
52	-A	B	B	B	-A	-A	-A	B
53	-A	B	B	B	-A	B	B	B
54	B	B	B	-C	B	B	B	B
55	B	B	B	-C	B	B	B	-C
56	B	-C	-C	-C	B	B	B	-C
57	B	-C	-C	-C	B	B	B	-C
58	B	-C	-C	-C	B	-C	-C	-C
59	-C	-C	-C	A	-C	-C	-C	-C
60	-C	-C	-C	A	-C	-C	-C	-C
61	-C	-C	A	A	-C	-C	-C	A
62	-C	A	A	A	-C	-C	-C	A
63	-C	A	A	A	-C	-C	A	A
64	A	A	A	-B	A	A	A	A
65	A	A	A	-B	A	A	A	A
66	A	A	-B	-B	A	A	A	-B
67	A	-B	-B	-B	A	A	A	-B
68	A	-B	-B	-B	A	A	-B	-B
69	A	-B	-B	C	A	-B	-B	-B
70	-B	-B	-B	C	-B	-B	-B	-B
71	-B	-B	C	C	-B	-B	-B	C
72	-B	C	C	C	-B	-B	-B	C
73	-B	C	C	C	-B	-B	C	C
74	-B	C	C	-A	-B	C	C	C
75	C	C	C	-A	C	C	C	C
76	C	C	-A	-A	C	C	C	-A

77	C	-A	-A	-A	C	C	C	-A
78	C	-A	-A	-A	C	C	-A	-A
79	C	-A	-A	B	C	-A	-A	-A
80	-A	-A	-A	B	-A	-A	-A	-A
81	-A	-A	B	B	-A	-A	-A	B
82	-A	-A	B	B	-A	-A	-A	B
83	-A	B	B	B	-A	-A	B	B
84	-A	B	B	-C	-A	-A	B	B
85	B	B	B	-C	B	B	B	B
86	B	B	-C	-C	B	B	B	-C
87	B	B	-C	-C	B	B	B	-C
88	B	-C	-C	-C	B	B	B	-C
89	B	-C	-C	A	B	B	-C	-C
90	B	-C	-C	A	B	-C	-C	-C
91	-C	-C	A	A	-C	-C	-C	A
92	-C	-C	A	A	-C	-C	-C	A
93	-C	A	A	A	-C	-C	-C	A
94	-C	A	A	-B	-C	-C	A	A
95	-C	A	A	-B	-C	A	A	A
96	A	A	-B	-B	A	A	A	-B
97	A	A	-B	-B	A	A	A	-B
98	A	-B	-B	-B	A	A	A	-B
99	A	-B	-B	C	A	A	-B	-B
100	A	-B	-B	C	A	-B	-B	-B
101	-B	-B	C	C	-B	-B	-B	-B
102	-B	-B	C	C	-B	-B	-B	C
103	-B	-B	C	C	-B	-B	-B	C
104	-B	C	C	-A	-B	-B	C	C

105	-B	C	C	-A	-B	-B	C	C
106	C	C	-A	-A	C	C	C	C
107	C	C	-A	-A	C	C	C	-A
108	C	C	-A	-A	C	C	C	-A
109	C	-A	-A	B	C	C	-A	-A
110	C	-A	-A	B	C	C	-A	-A
111	C	-A	B	B	C	-A	-A	-A
112	-A	-A	B	B	-A	-A	-A	B
113	-A	-A	B	B	-A	-A	-A	B
114	-A	B	B	-C	-A	-A	B	B
115	-A	B	B	-C	-A	-A	B	B
116	-A	B	-C	-C	-A	B	B	B
117	B	B	-C	-C	B	B	B	-C
118	B	B	-C	-C	B	B	B	-C
119	B	-C	-C	A	B	B	-C	-C
120	B	-C	-C	A	B	B	-C	-C
121	B	-C			B	-C	-C	-C
122	-C	-C			-C	-C	-C	A
123	-C	-C			-C	-C	-C	A
124	-C	-C			-C	-C		
125	-C	A			-C	-C		
126	-C	A			-C	-C		

Appendix B: Magnetic properties of the steel used in the modelling:

B.1: M300-35A Steel

Typical data for SURA® M300-35A

T	W/kg at 50 Hz	VA/kg at 50 Hz	A/m at 50 Hz	W/kg at 100 Hz	W/kg at 200 Hz	W/kg at 400 Hz	W/kg at 1000 Hz	W/kg at 2500 Hz
0,1	0,03	0,07	30,9	0,04	0,09	0,23	1,07	4,45
0,2	0,08	0,17	40,2	0,17	0,40	1,00	4,08	16,1
0,3	0,15	0,30	46,4	0,35	0,85	2,15	8,48	33,6
0,4	0,24	0,45	52,1	0,58	1,41	3,61	14,0	56,9
0,5	0,35	0,62	57,9	0,84	2,06	5,36	20,9	86,6
0,6	0,48	0,82	64,4	1,14	2,81	7,42	29,2	124
0,7	0,61	1,05	72,0	1,46	3,66	9,75	39,0	170
0,8	0,76	1,31	81,1	1,83	4,61	12,4	50,6	227
0,9	0,92	1,63	92,6	2,23	5,65	15,4	64,1	297
1,0	1,10	2,03	108	2,66	6,80	18,8	79,8	382
1,1	1,30	2,55	130	3,16	8,09	22,5	98,0	
1,2	1,54	3,32	168	3,72	9,54	26,8		
1,3	1,82	4,71	250	4,39	11,2	31,6		
1,4	2,20	8,61	510	5,23	13,4	37,7		
1,5	2,62	23,7	1440	6,22	15,7	44,3		
1,6	2,98	64,1	3490					
1,7	3,25	138	6700					
1,8	3,41	255	11300					

Loss at 1.5 T , 50 Hz, W/kg	2,62
Loss at 1.0 T , 50 Hz, W/kg	1,10
Anisotropy of loss, %	10
Magnetic polarization at 50 Hz	
H = 2500 A/m, T	1,55
H = 5000 A/m, T	1,65
H = 10000 A/m, T	1,78
Coercivity (DC), A/m	45
Relative permeability at 1.5 T	830
Resistivity, μΩcm	50
Yield strength, N/mm²	370
Tensile strength, N/mm²	490
Young's modulus, RD, N/mm²	185 000
Young's modulus, TD, N/mm²	200 000
Hardness HV5 (VPN)	185

RD represents the rolling direction
TD represents the transverse direction
Values for yield strength (0.2 % proof strength) and tensile strength are given for the rolling direction
Values for the transverse direction are approximately 5% higher

cogent
Surahammars Bruks AB

June 2008

Figure B.1: The material properties of M300-35A Steel [1]

[1] Cogent, Surahammers Bruks AB. Available: https://cogent-power.com/cms-data/downloads/m300-35a.pdf, Accessed on: 04.06.2018

B.2: Steel 1010:

Table B.2: Table of the magnetic values of steel 1010, extracted from Ansys Maxwell's material library.

H [A/m]	B [T]
0	0
235.7	0.2003
318.3	0.3204
358.1	0.40045
437.7	0.50055
477.7	0.5606
636.6	0.7908
795.8	0.931
1114.1	1.1014
1273.2	1.2016
1591.5	1.302
2228.2	1.4028
3183.1	1.524

H [A/m]	B [T]
2228.2	1.4028
3183.1	1.524
4774.6	1.626
6366.2	1.698
7957.7	1.73
15915.5	1.87
31831	1.99
47746.5	2.04
63662	2.07
79577.5	2.095
159155	2.2
318310	2.4

Appendix C: Fourier Series Calculation of the simplified MMF-model

Fourier analysis of the signal shown in below, where the length x-axis length of each peak is $\theta_P = \frac{2\pi}{8}$

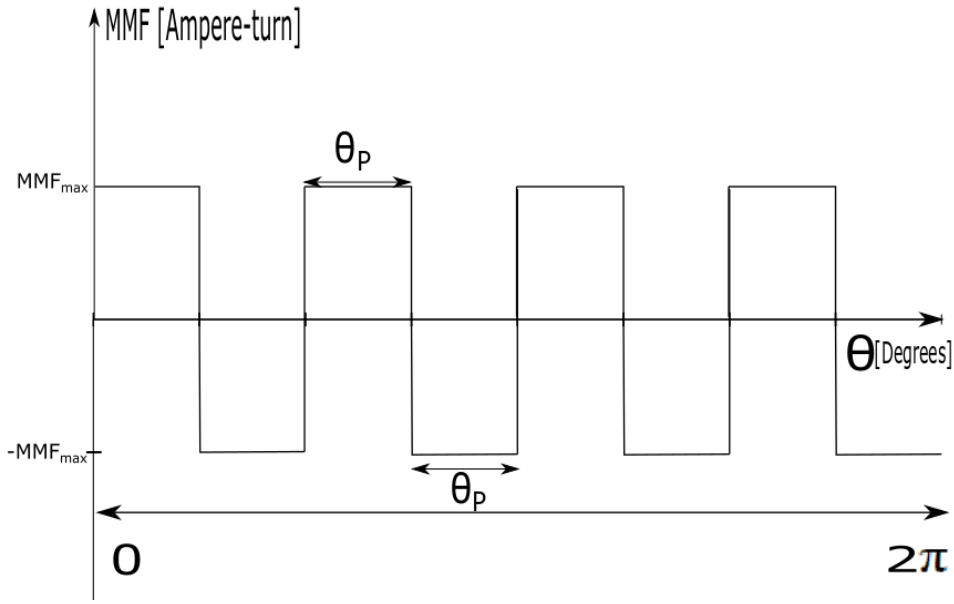

Figure C.1: Simplified model of the MMF produced by the rotor, seen from the rotor reference.

The model contains eight poles and spans entire 360° of the rotor surface.θ_P is the span of one pole.

$$A_o = \frac{1}{2\pi}\left(\int_0^{\theta_P} MMF_{max} - \int_{\theta_P}^{2\theta_P} MMF_{max} + \int_{2\theta_P}^{3\theta_P} MMF_{max} - \int_{3\theta_P}^{4\theta_P} MMF_{max} + \int_{4\theta_P}^{5\theta_P} MMF_{max} - \int_{5\theta_P}^{6\theta_P} MMF_{max} + \int_{6\theta_P}^{7\theta_P} MMF_{max} - \int_{7\theta_P}^{8\theta_P} MMF_{max}\right) = 0.$$

$$A_n = \frac{1}{\pi}\left(\int_0^{\theta_P} MMF_{max}\cos(n\theta) - \int_{\theta_P}^{2\theta_P} MMF_{max}\cos(n\theta)\right.$$

$$+ \int_{2\theta_P}^{3\theta_P} MMF_{max}\cos(n\theta) - \int_{3\theta_P}^{4\theta_P} MMF_{max}\cos(n\theta)$$

$$+ \int_{4\theta_P}^{5\theta_P} MMF_{max}\cos(n\theta) - \int_{5\theta_P}^{6\theta_P} MMF_{max}\cos(n\theta)$$

$$\left.+ \int_{6\theta_P}^{7\theta_P} MMF_{max}\cos(n\theta) - \int_{7\theta_P}^{8\theta_P} MMF_{max}\cos(n\theta)\right).$$

$$A_n = \frac{1}{\pi}\left(\left[\frac{MFF_{max}\sin(n\theta)}{n}\right]_0^{\frac{\pi}{4}} - \left[\frac{MFF_{max}\sin(n\theta)}{n}\right]_{\frac{\pi}{4}}^{\frac{2\pi}{4}} + \left[\frac{MFF_{max}\sin(n\theta)}{n}\right]_{\frac{2\pi}{4}}^{\frac{3\pi}{4}}\right.$$

$$- \left[\frac{MFF_{max}\sin(n\theta)}{n}\right]_{\frac{3\pi}{4}}^{\frac{4\pi}{4}} + \left[\frac{MFF_{max}\sin(n\theta)}{n}\right]_{\frac{4\pi}{4}}^{\frac{5\pi}{4}}$$

$$- \left[\frac{MFF_{max}\sin(n\theta)}{n}\right]_{\frac{5\pi}{4}}^{\frac{6\pi}{4}} + \left[\frac{MFF_{max}\sin(n\theta)}{n}\right]_{\frac{6\pi}{4}}^{\frac{7\pi}{4}}$$

$$\left.- \left[\frac{MFF_{max}\sin(n\theta)}{n}\right]_{\frac{7\pi}{4}}^{\frac{8\pi}{4}}\right),$$

$$A_n = \frac{1}{\pi}\left(\frac{MFF_{max}\sin\left(n*\frac{\pi}{4}\right)}{n} - \frac{MFF_{max}\sin(0)}{n} + \frac{MFF_{max}\sin\left(n*\frac{\pi}{4}\right)}{n}\right.$$

$$- \frac{MFF_{max}\sin\left(n*\frac{2\pi}{4}\right)}{n} - \frac{MFF_{max}\sin\left(n*\frac{2\pi}{4}\right)}{n}$$

$$+ \frac{MFF_{max}\sin\left(n*\frac{3\pi}{4}\right)}{n} + \frac{MFF_{max}\sin\left(n*\frac{3\pi}{4}\right)}{n}$$

$$- \frac{MFF_{max}\sin\left(n*\frac{4\pi}{4}\right)}{n} - \frac{MFF_{max}\sin\left(n*\frac{4\pi}{4}\right)}{n}$$

$$+ \frac{MFF_{max}\sin\left(n*\frac{5\pi}{4}\right)}{n} + \frac{MFF_{max}\sin\left(n*\frac{5\pi}{4}\right)}{n}$$

$$- \frac{MFF_{max}\sin\left(n*\frac{6\pi}{4}\right)}{n} - \frac{MFF_{max}\sin\left(n*\frac{6\pi}{4}\right)}{n}$$

$$+ \frac{MFF_{max}\sin\left(n*\frac{7\pi}{4}\right)}{n} + \frac{MFF_{max}\sin\left(n*\frac{7\pi}{4}\right)}{n}$$

$$\left. - \frac{MFF_{max}\sin\left(n*\frac{8\pi}{4}\right)}{n}\right) = 0.$$

$$B_n = \frac{1}{\pi}\left(\frac{2MFF_{max}\cos\left(n*\frac{\pi}{4}\right)}{n} - \frac{2MFF_{max}\cos\left(n*\frac{2\pi}{4}\right)}{n}\right.$$

$$+ \frac{2MFF_{max}\cos\left(n*\frac{3\pi}{4}\right)}{n} - \frac{2MFF_{max}\cos\left(n*\frac{4\pi}{4}\right)}{n}$$

$$+ \frac{2MFF_{max}\cos\left(n*\frac{5\pi}{4}\right)}{n} - \frac{2MFF_{max}\cos\left(n*\frac{6\pi}{4}\right)}{n}$$

$$\left. + \frac{2MFF_{max}\cos\left(n*\frac{7\pi}{4}\right)}{n} - \frac{2}{n}\right),$$

This gives:

$$F(\theta) = -\frac{4}{\pi}\sin(4\theta) - \frac{4}{3\pi}\sin(12\theta) - \frac{4}{5\pi}\sin(20\theta) - \frac{1}{6\pi}\sin(24\theta) - \cdots$$

Appendix D: Result Machine 2

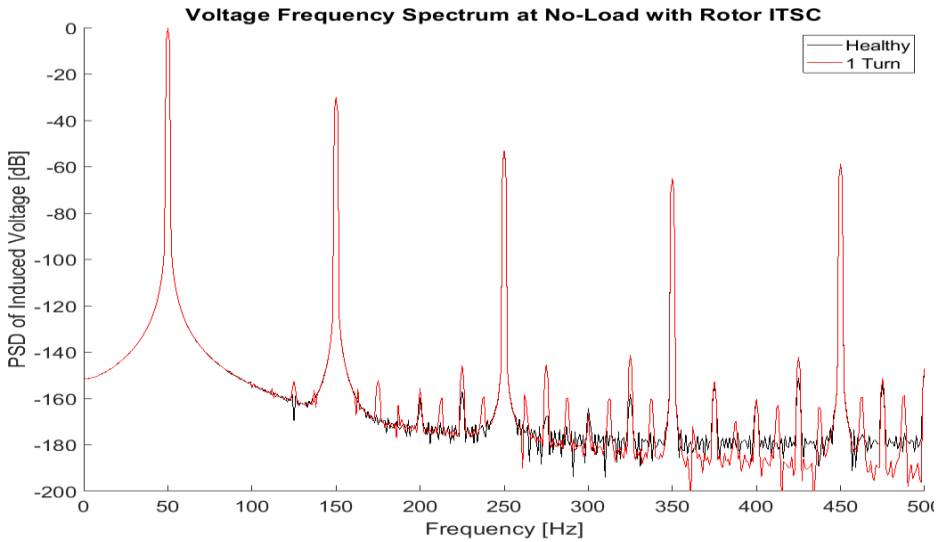

Figure D.1: Voltage PSD of Machine 2 with rotor ITSC at no-load simulation.

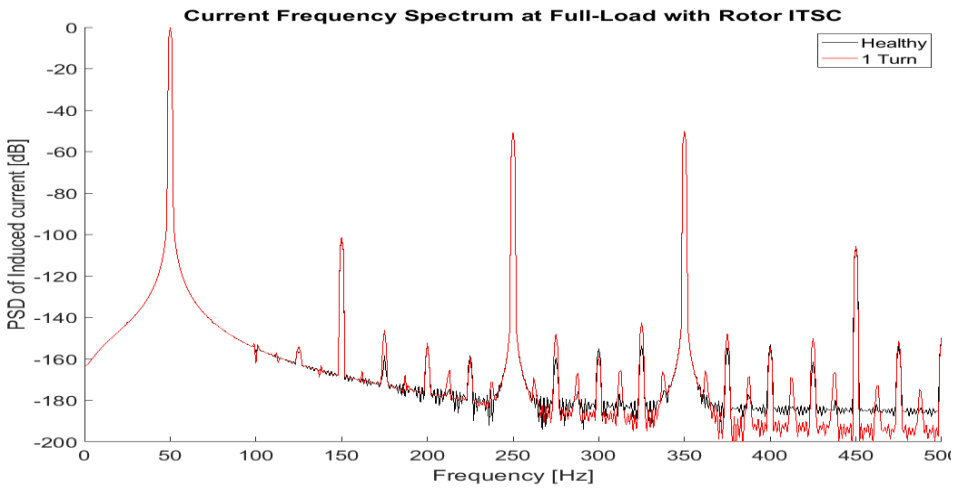

Figure D.2: Current PSD of Machine 2 with rotor ITSC at full-load simulation.

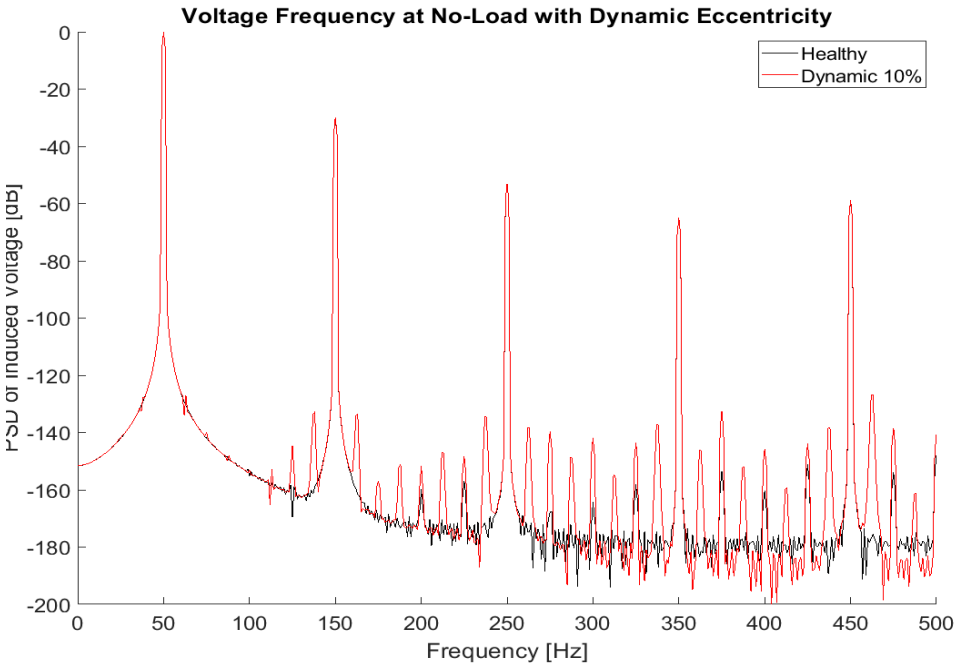

Figure D.3: Voltage PSD of Machine 2 for dynamic eccentricity at no-load simulation.

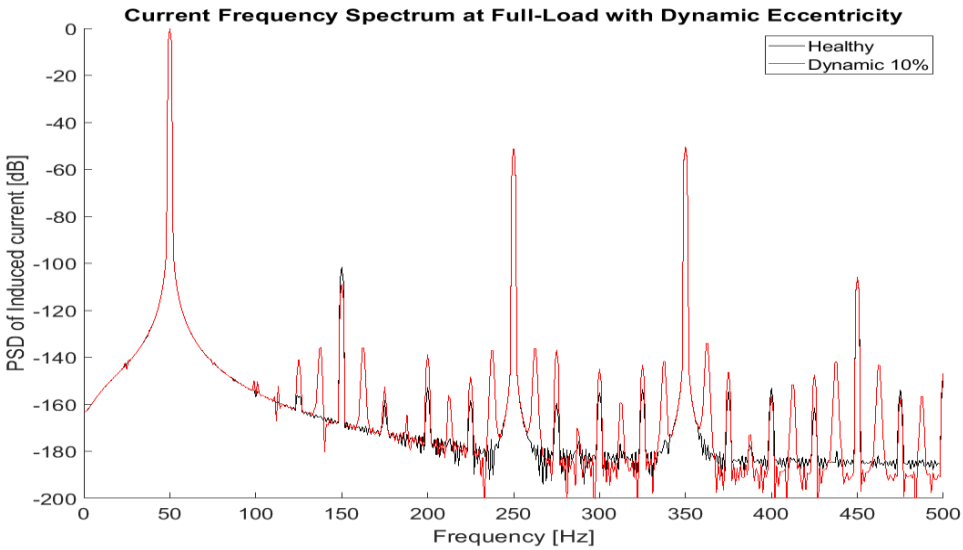

Figure D.4: Current PSD of Machine 2 with dynamic eccentricity at full-load simulation.

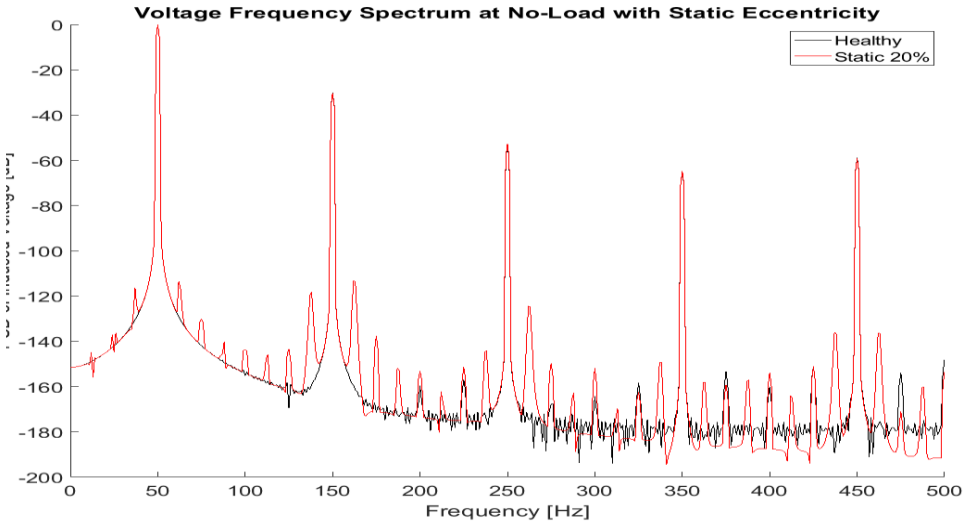

Figure D.5: Voltage PSD of Machine 2 with static eccentricity at no-load simulation.

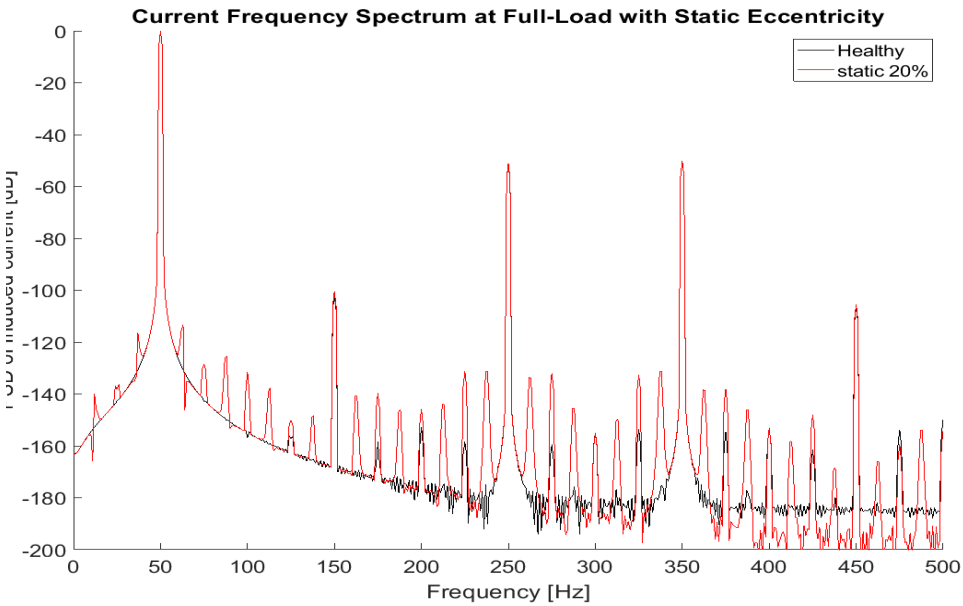

Figure D.6: Current PSD of Machine 2 with static eccentricity at full-load simulation.

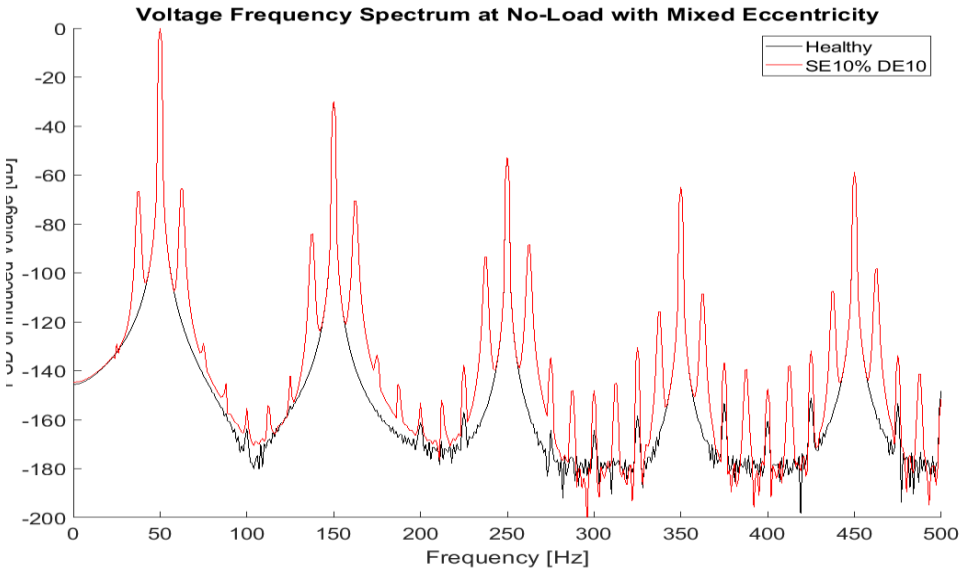

Figure D.7: Voltage PSD of Machine 2 with mixed eccentricity at no-load simulation.

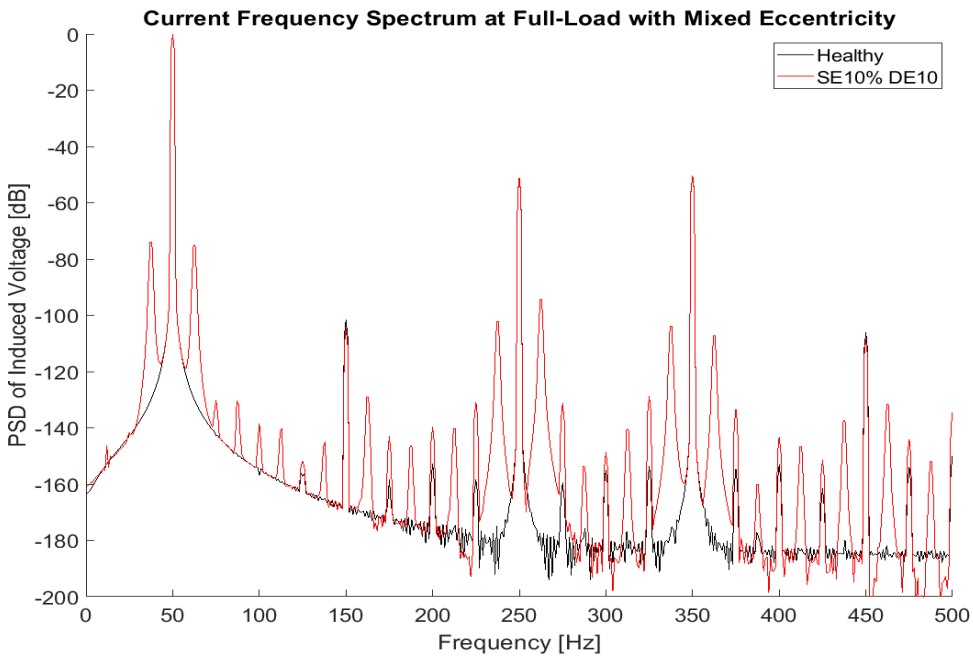

Figure D.8: Current PSD of Machine 2 with mixed eccentricity at full-load simulation.

Appendix E: Result of Machine 3

E.1 Dynamic Eccentricity results

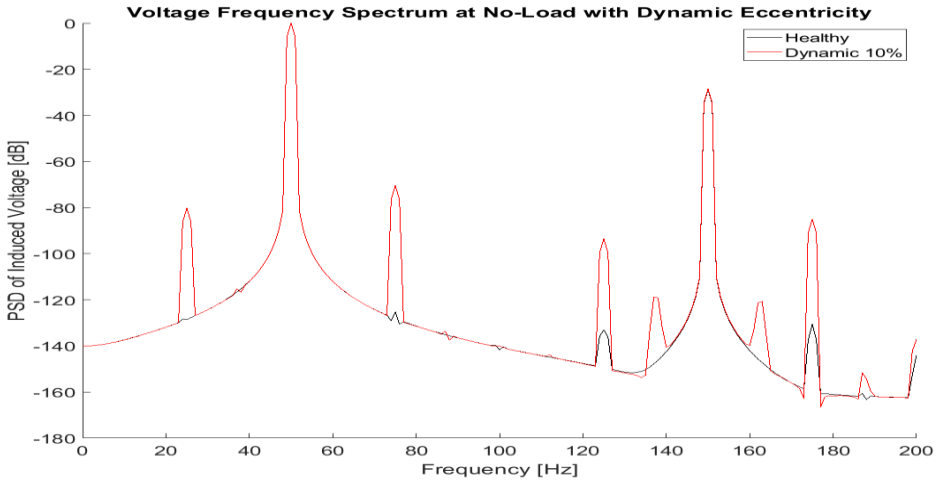

Figure E.1: Voltage PSD of Machine 3 with dynamic eccentricity at no-load simulation.

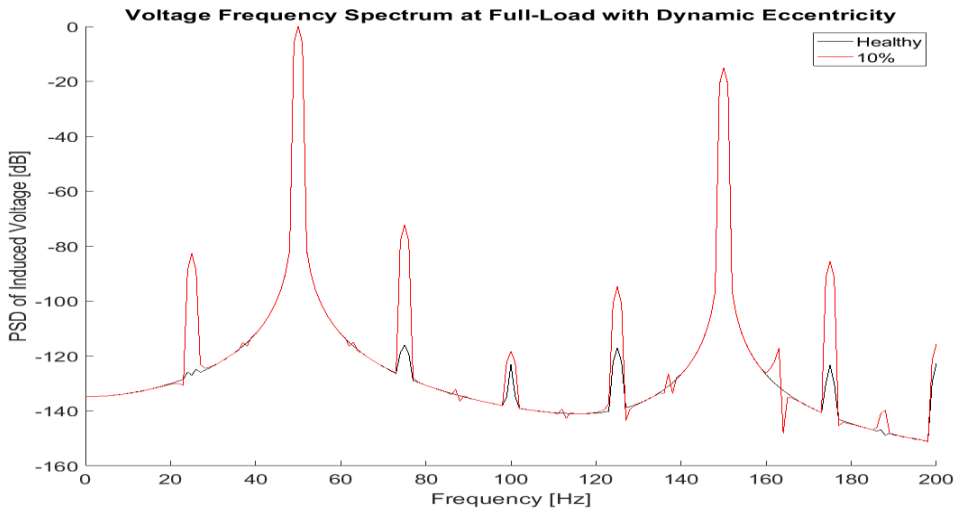

Figure E.2: voltage PSD Machine 3 with dynamic eccentricity at full-load simulation.

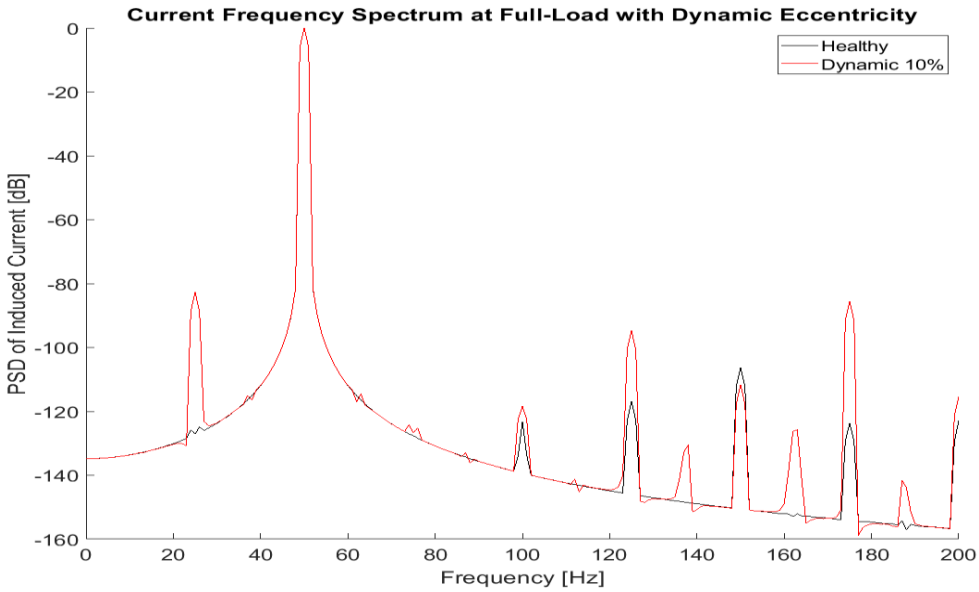

Figure E.3: Current PSD Machine 3 with dynamic eccentricity at full-load simulation.

E.2 Rotor ITSC Result

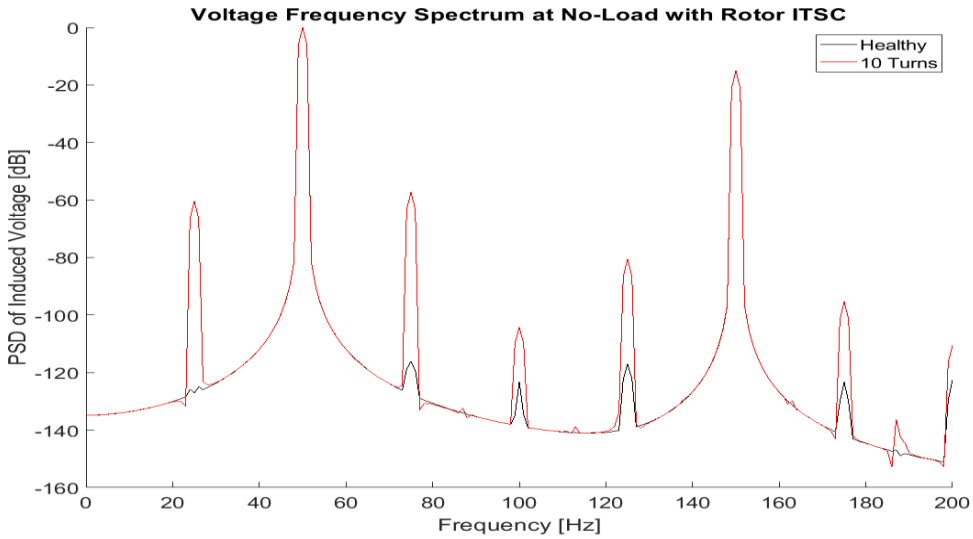

Figure E.4: Voltage PSD Machine 3 with rotor ITSC eccentricity at no-load simulation.

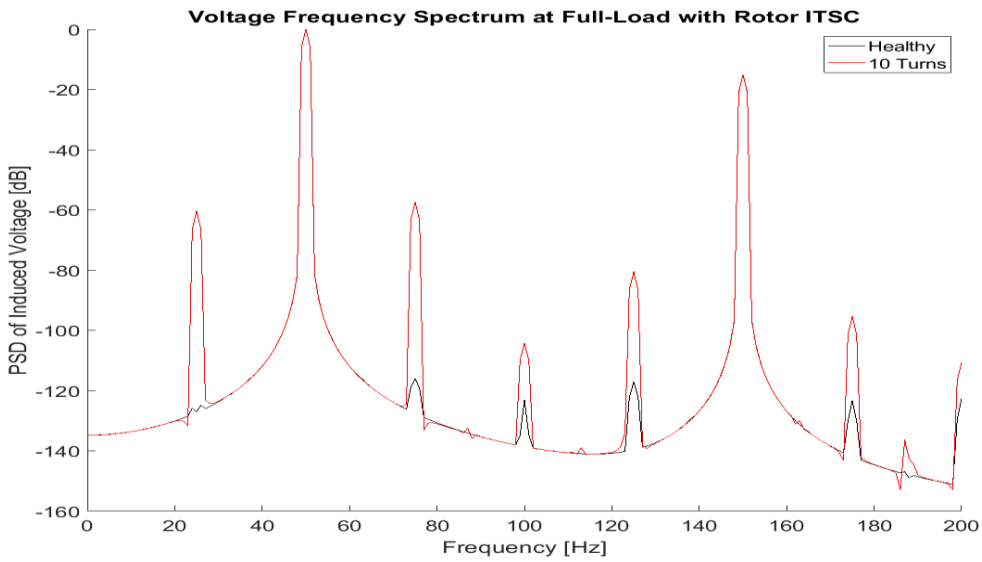

Figure E.5: Voltage PSD Machine 3 with rotor ITSC eccentricity at full-load simulation.

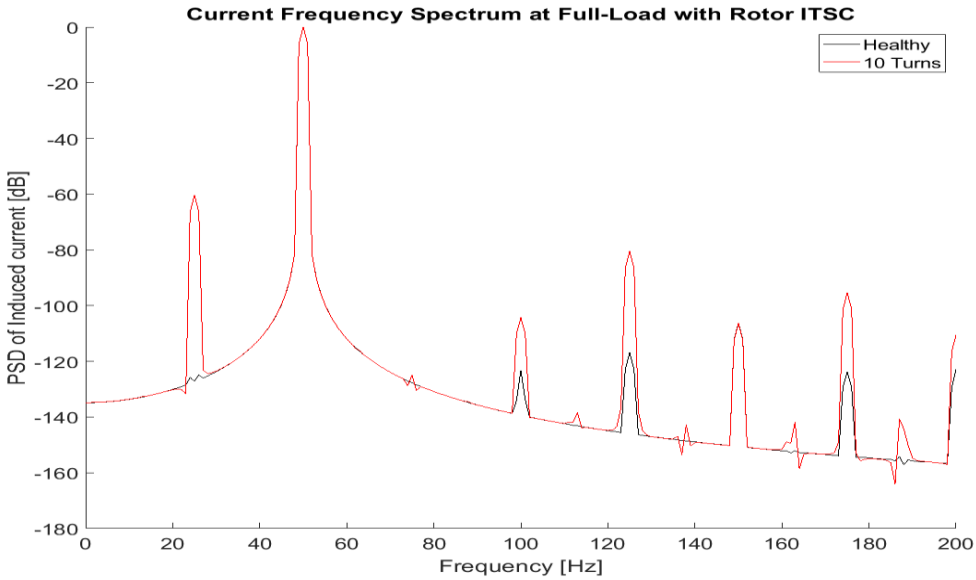

Figure E.6: Current PSD Machine 3 with rotor ITSC eccentricity at full-load simulation.

E.3 Static Eccentricity Results

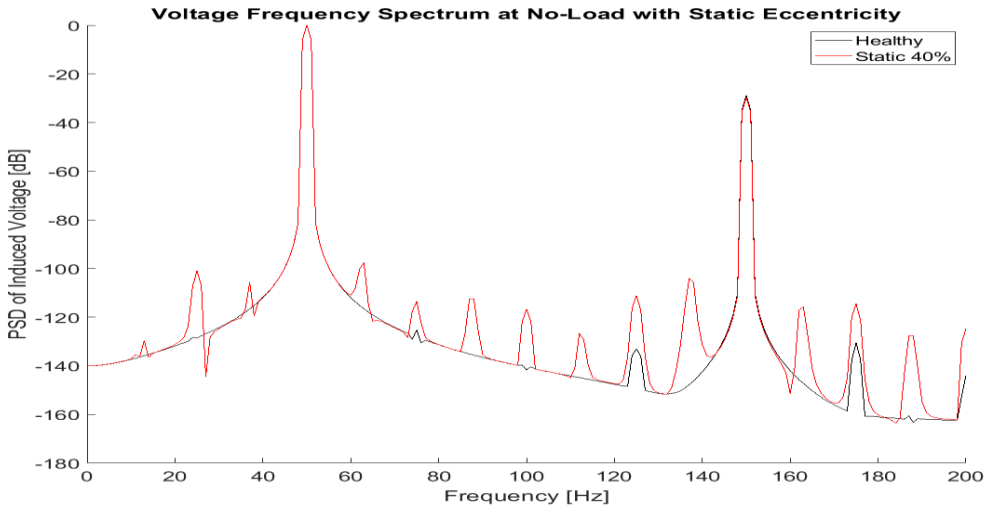

Figure E.7: Voltage PSD Machine 3 with static eccentricity at no-load simulation.

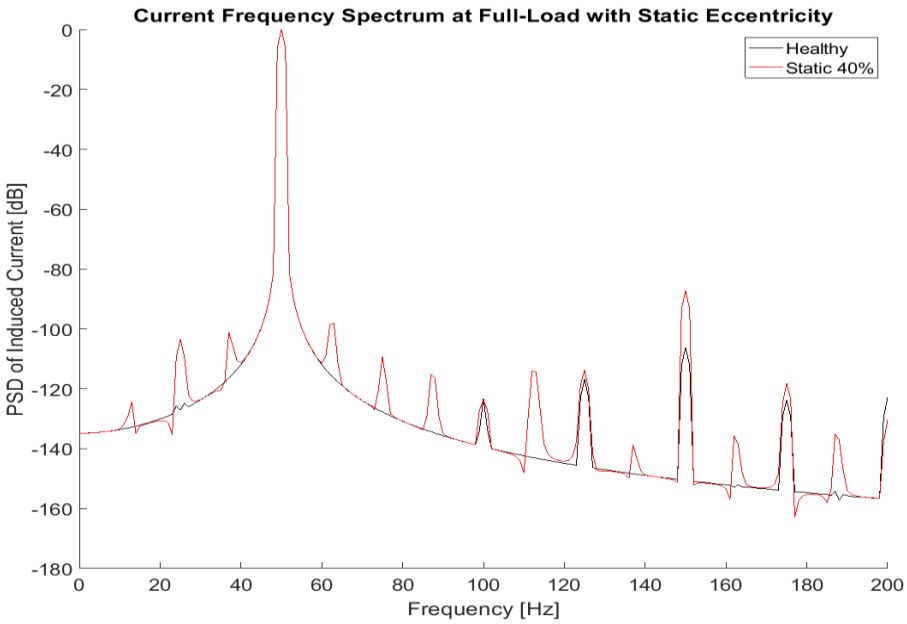

Figure E.8: Voltage PSD Machine 3 with static eccentricity at full-load simulation.

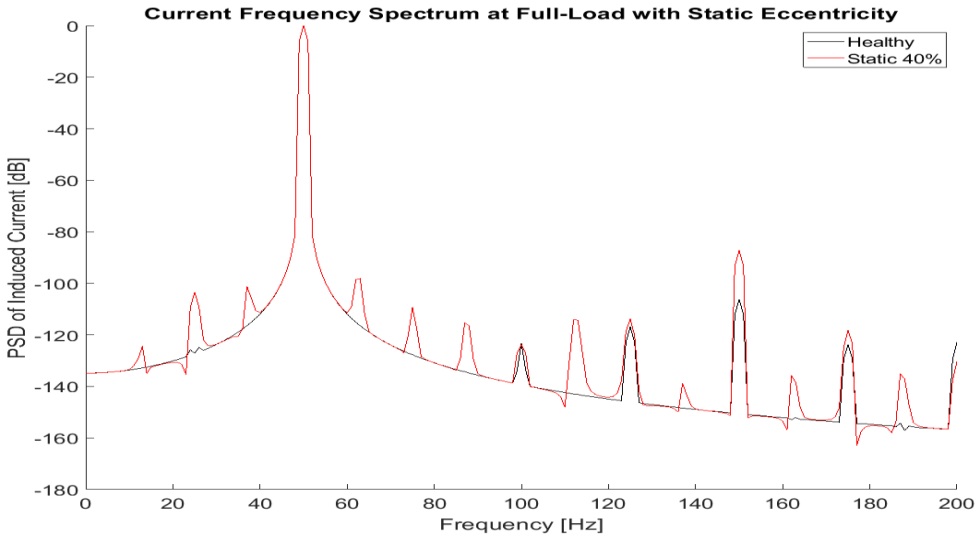

Figure E.9: Current PSD Machine 3 with static eccentricity at full-load simulation.

E.4 Mixed Eccentricity Results

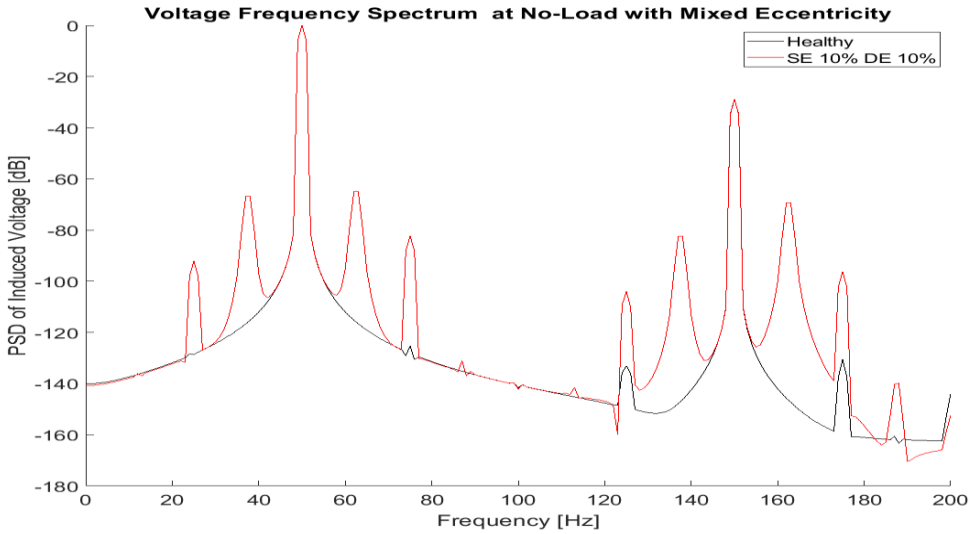

Figure E.10: Voltage PSD Machine 3 with mixed eccentricity at no-load simulation.

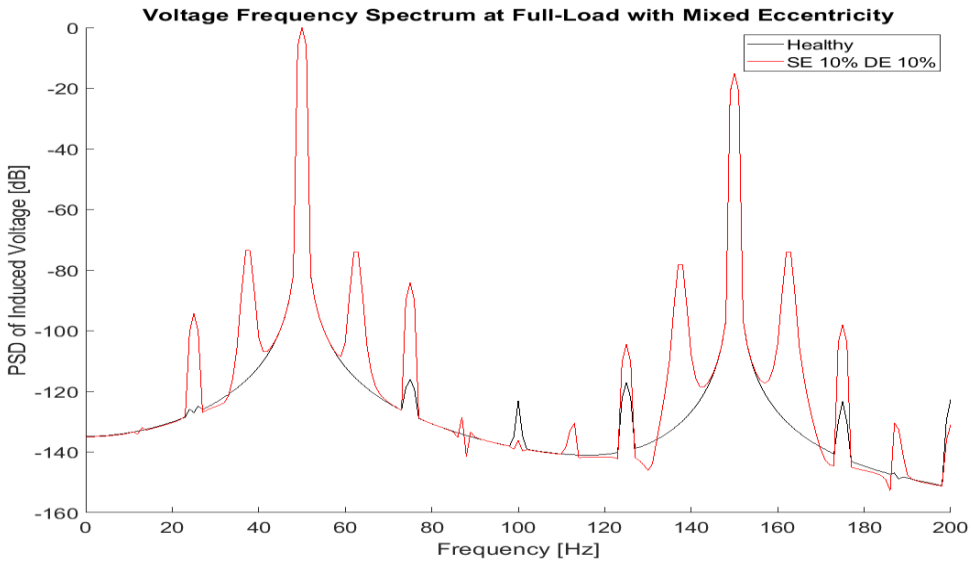

Figure E.11: Voltage PSD Machine 3 with mixed eccentricity at full-load simulation.

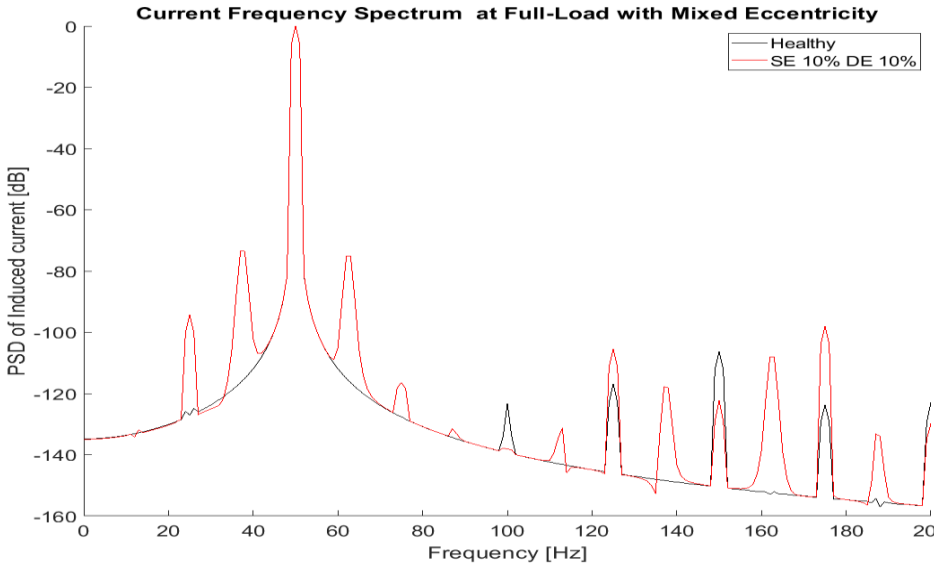

Figure E.12: Current PSD Machine 3 with mixed eccentricity at no-load simulation.

Appendix F: Simulation Results Machine 4

F.1 Dynamic Eccentricity Results

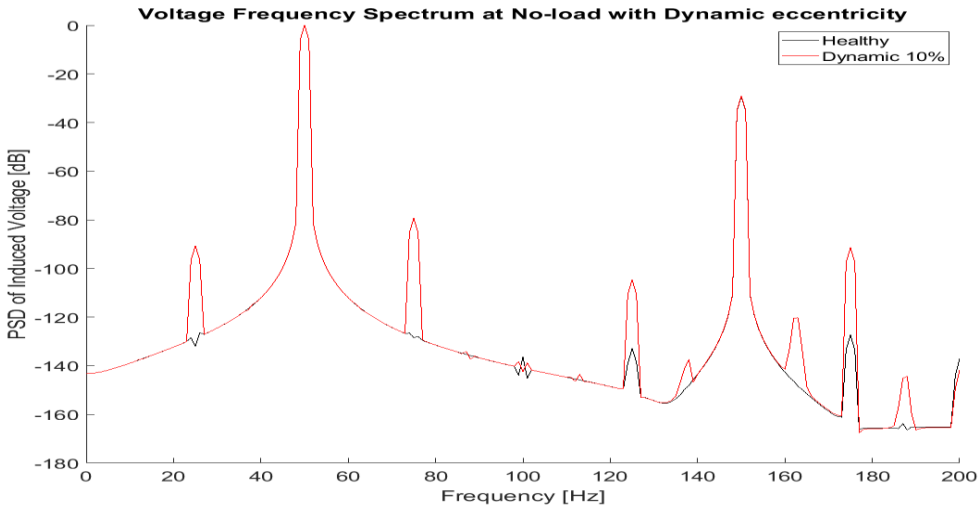

Figure F.1: Voltage PSD Machine 4 with dynamic eccentricity at no-load simulation.

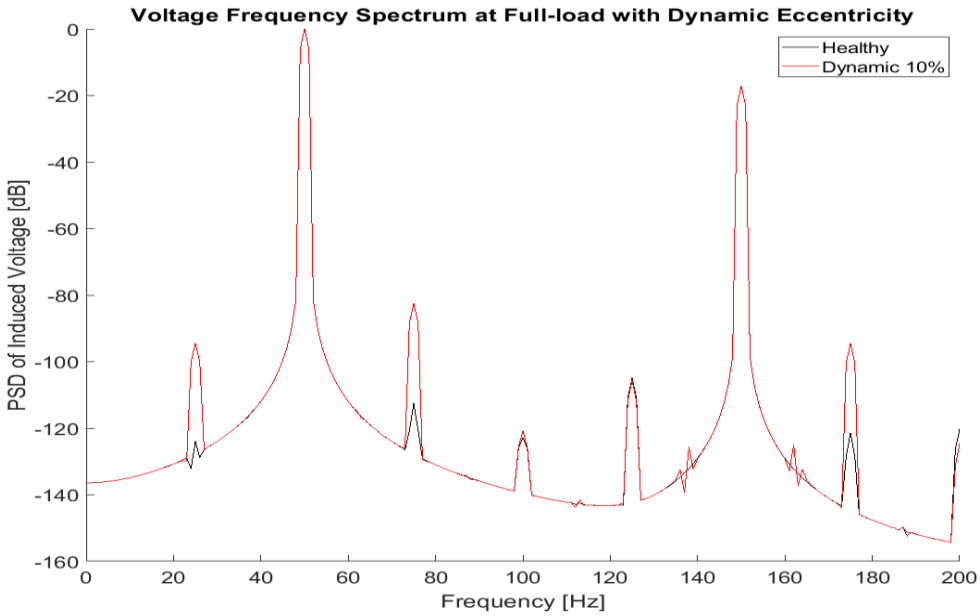

Figure F.2: Voltage PSD Machine 4 with dynamic eccentricity at full-load simulation.

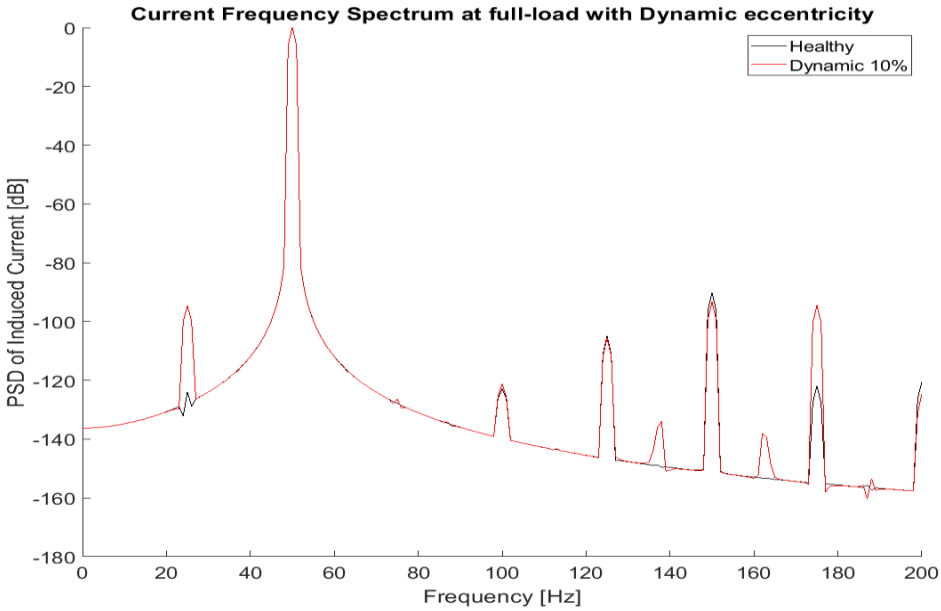

Figure F.3: Current PSD Machine 4 with mixed eccentricity at full-load simulation.

F.2 Static Eccentricity Results

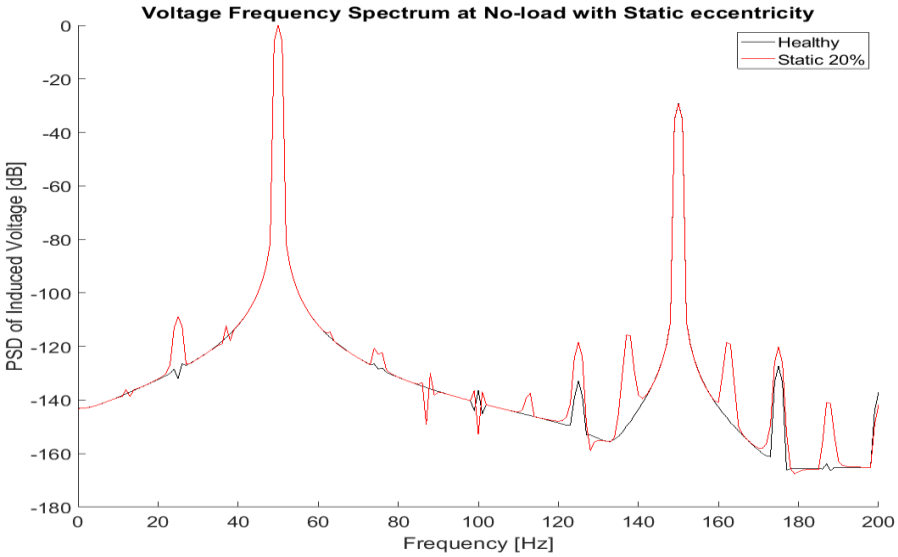

Figure F.4: Voltage PSD Machine 4 with static eccentricity at no-load simulation.

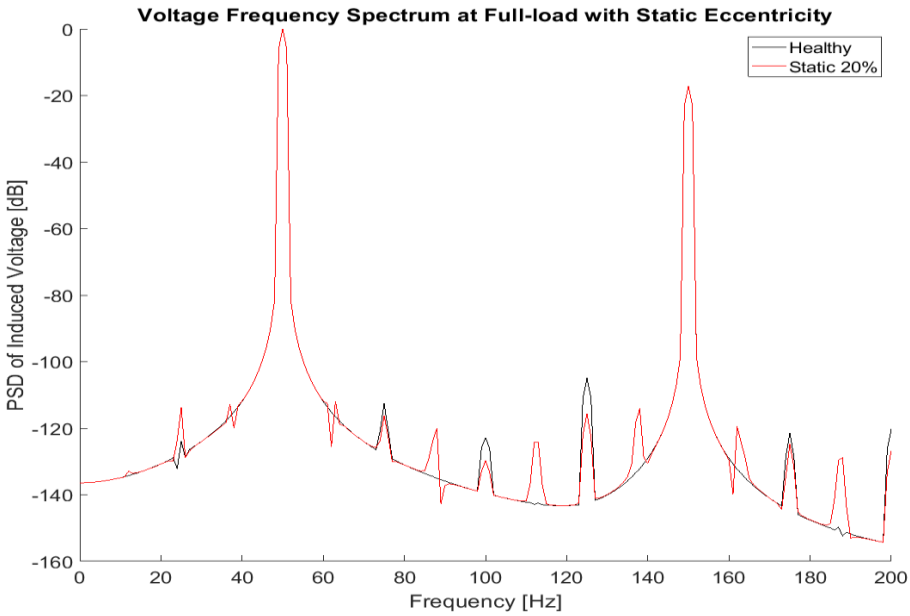

Figure F.5: Voltage PSD Machine 4 with mixed eccentricity at full-load simulation.

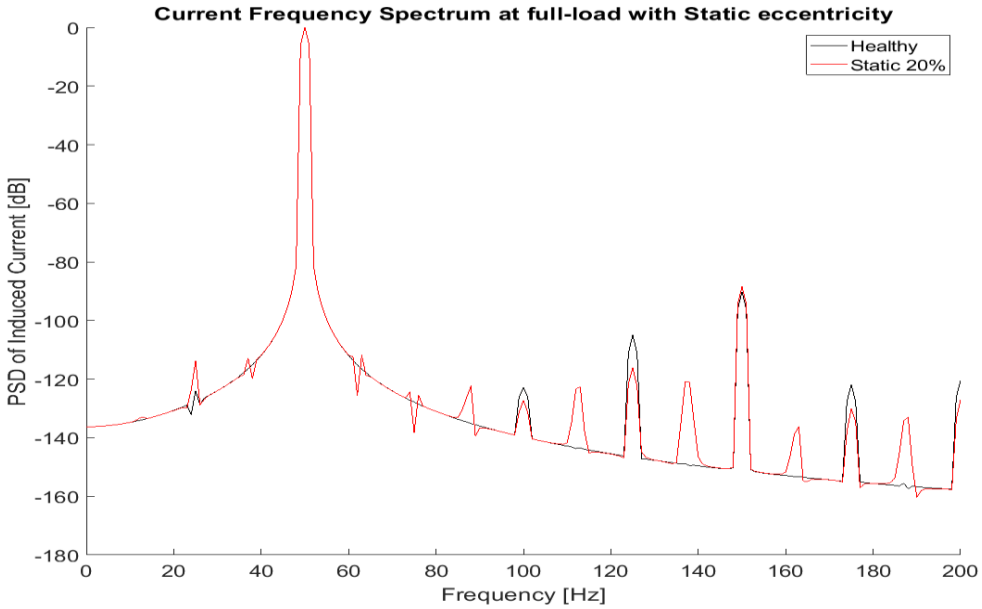

Figure F.6: Current PSD Machine 4 with static eccentricity at full-load simulation.

F.3 Rotor ITSC Results

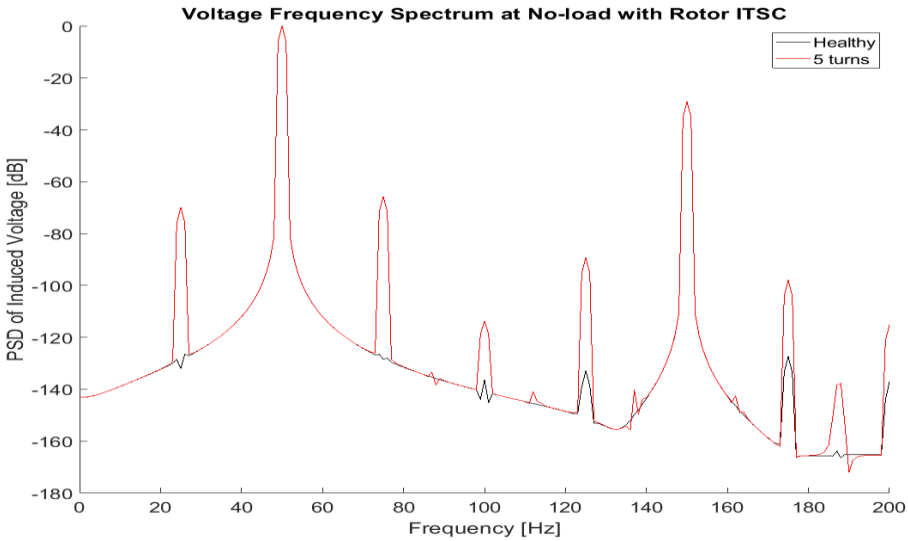

Figure F.7: Voltage PSD Machine 4 with rotor ITSC at no-load simulation.

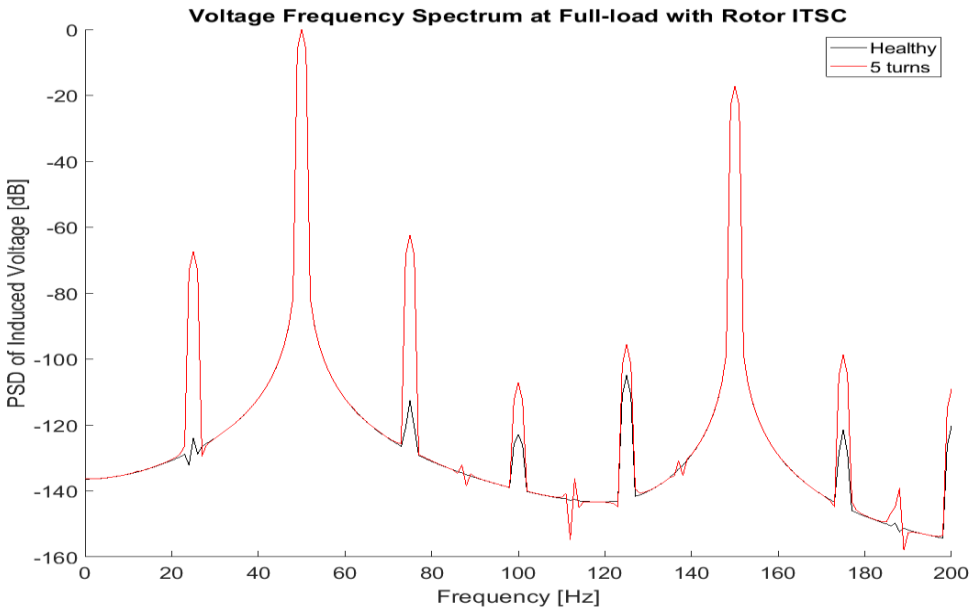

Figure F.8: Voltage PSD Machine 4 with rotor ITSC at full-load simulation.

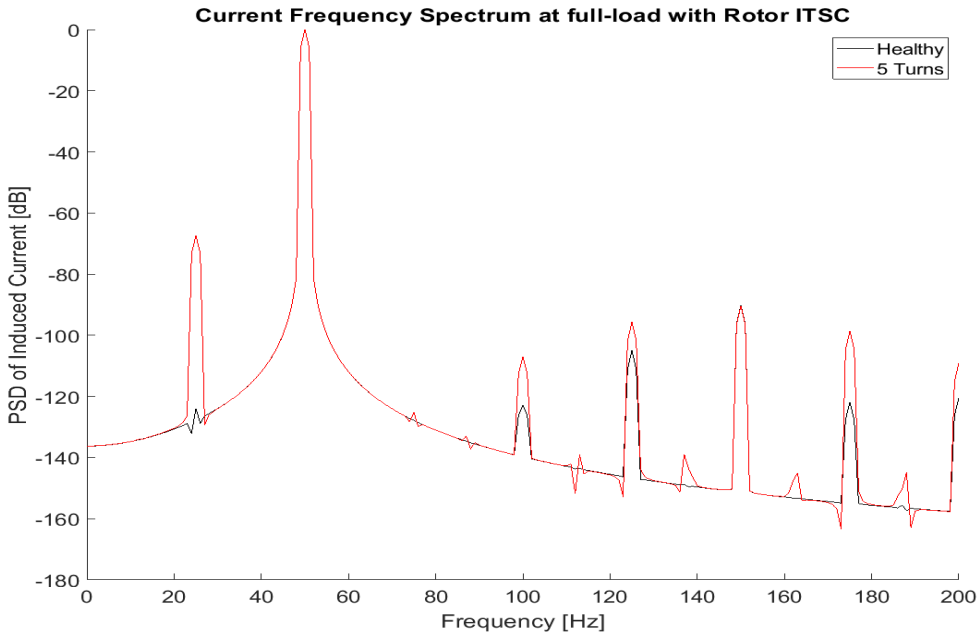

Figure F.9: Current PSD Machine 4 with rotor ITSC at full-load simulation.

F.4 Mixed Eccentricity Results

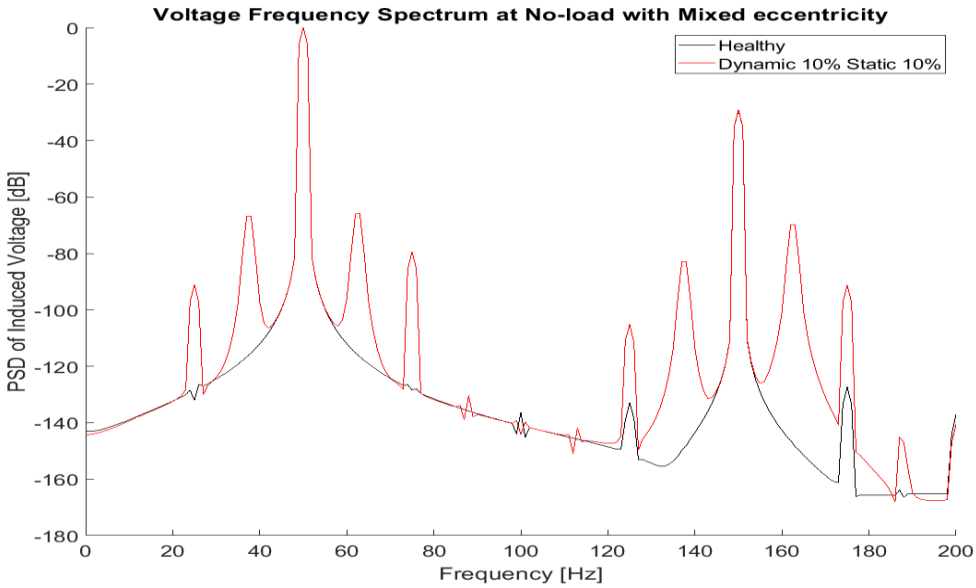

Figure F.10: Voltage PSD Machine 4 with mixed eccentricity at no-load simulation.

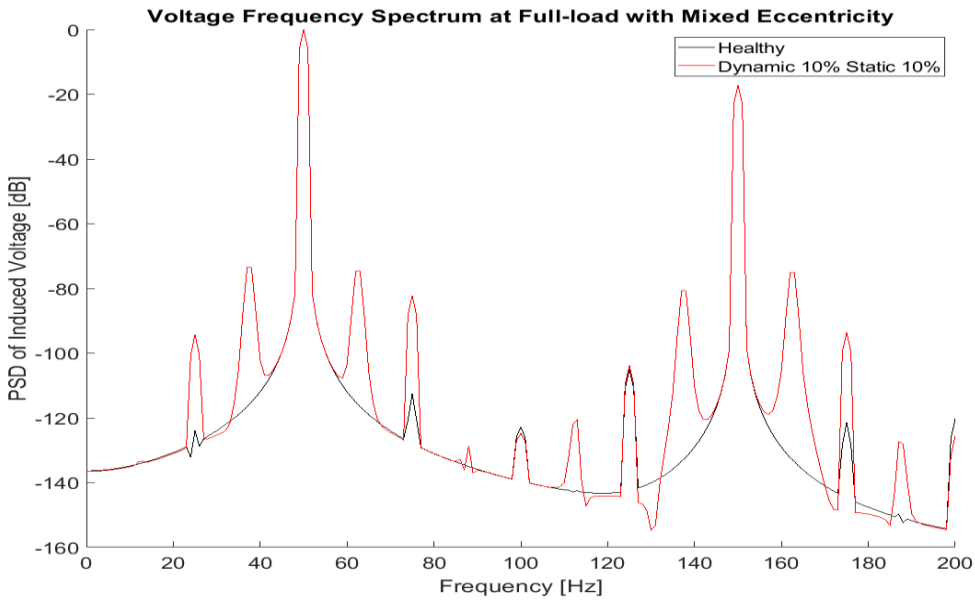

Figure F.11: Voltage PSD Machine 4 with mixed eccentricity at full-load simulation.

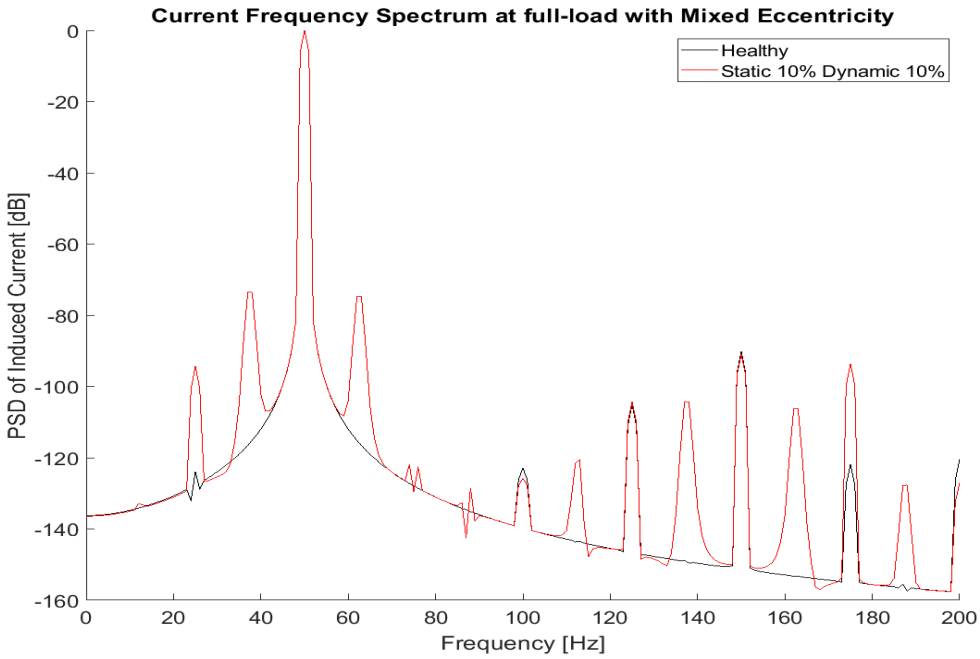

Figure F.12: Current PSD Machine 4 with mixed eccentricity at full-load simulation.